

Stellingen

Het principe om de sapstroom in een plantenstengel te kwantificeren door het NMR signaal daarvan als functie van stromingscoderende stappen in de magnetische veldgradienten te fitten aan een modelfunctie is onjuist.

Dit proefschrift, hoofdstuk 4.

Het gebruik van een PFG stimulated echo sequentie vergemakkelijkt aanzienlijk het onderscheiden van de verplaatsing van watermoleculen t.g.v. extreem langzame stroming en t.g.v. diffusie.

Dit proefschrift, hoofdstuk 3.

Geen van de gangbare theorieën over het verdwijnen van embolieën in xyleemvaten geeft een bevredigende verklaring voor het achterliggend mechanisme.

Dit proefschrift, hoofdstuk 6.

De aan een laag magneetveld inherente lage NMR signaal/ruis verhouding onmiddellijk na excitatie kan gecompenseerd worden door het opnemen van veel echo's.

Dit proefschrift, hoofdstuk 7.

Omdat voor ieder pixel meerdere NMR parameters toegankelijk zijn is het streven naar een zo hoog mogelijke ruimtelijke resolutie in een NMRi experiment niet alleen vaak onnodig, maar introduceert ook een extra signaalafname.

Dit proefschrift, hoofdstuk 7.

Capillaire elektrochromatografie is superieur aan drukgedreven capillaire chromatografie voor het scheiden van complexe mengsels, zeker indien de zeta-potentiaal van de capillairwand is afgestemd op die van het kolommateriaal.

Als de drugsbestrijding in Nederland onder de vlag van de binnenlandse veiligheidsdienst zou opereren, zou zij daadkrachtiger op kunnen treden.

Veel oudere werknemers verdienen meer dan dat zij op grond van prestatie en behoefte van de arbeidsmarkt behoren te krijgen.

Om de belangen van de consument te beschermen, zou de Nederlandse staat als aanbieder op moeten kunnen treden van primaire, utilitaire levensbehoeften, waaronder energie, water en telecommunicatie.

Stellingen behorend bij het proefschrift

Nuclear Magnetic Resonance imaging of water motion in plants

Tom Scheenen

Wageningen, 21 september 2001

**Nuclear Magnetic Resonance Imaging
of Water Motion in Plants**

Tom W. J. Scheenen

promotor:

**prof. dr. T.J. Schaafsma,
hoogleraar in de Moleculaire Fysica
Wageningen Universiteit**

co-promotor:

**dr. H. Van As, universitair hoofddocent
Laboratorium voor Biofysica
Wageningen Universiteit**

Promotiecommissie:

**prof. dr. ir. J. Goudriaan, Wageningen Universiteit
prof. dr. C. Kollöffel, Universiteit Utrecht
prof. dr. O. van Kooten, Wageningen Universiteit
prof. dr. K. Nicolay, Universiteit Eindhoven
dr. W. Köckenberger, Universiteit van Nottingham, Engeland**

nn 08701, 3032

Nuclear Magnetic Resonance Imaging of Water Motion in Plants

Tom W. J. Scheenen

Proefschrift

ter verkrijging van de graad van doctor
op gezag van de rector magnificus
van Wageningen Universiteit,
prof. dr. ir. L. Speelman
in het openbaar te verdedigen
op vrijdag 21 september 2001
des ochtends te elf uur in de aula.

Tom W. J. Scheenen

The work presented in this thesis was performed at the Wageningen University,
Department of Agrotechnology and Food Sciences, Laboratory of Biophysics,
Dreijenlaan 3, 6703 HA Wageningen, The Netherlands

Scheenen, T. W. J.

Nuclear Magnetic Resonance Imaging of Water Motion in Plants

Thesis, Wageningen University – With summary in Dutch

ISBN: 90-5808-475-2

Subject Headings:

cavitation / diffusion / embolism / flow / MRI / NMR microscopy / PFG / plants /
propagator / q-space / relaxation / resolution / stimulated echo / T_2 / transport /
turbo spin echo / vessels / xylem

Contents

Voorwoord

Chapter 1: Introduction	1
Chapter 2: Microscopic displacement imaging with pulsed field gradient turbo spin echo NMR	9
Chapter 3: Microscopic imaging of slow flow and diffusion: a pulsed field gradient stimulated echo sequence combined with turbo spin echo imaging	29
Addendum: The combination of a pulsed field gradient spin echo sequence with multiple spin echo imaging	43
Chapter 4: Quantification of water transport in plants with NMR imaging	47
Chapter 5: Functional imaging of plants: a Nuclear Magnetic Resonance study of a cucumber plant	65
Chapter 6: Embolism induction and repair in xylem vessels of <i>Cucumis Sativus</i> L.	89
Chapter 7: Measuring plant water status and transport with Nuclear Magnetic Resonance imaging: a strategy	105
Summary	127
Samenvatting	129
List of Publications	131
Curriculum vitae	133

Voorwoord

Nou dit is het dan. Tastbaar bewijs dat ik toch gewerkt heb de afgelopen jaren. Ik wil graag een aantal mensen bedanken voor hun bijdrage aan mijn tijd op Moleculaire Fysica (nu Biofysica). Ten eerste Henk, als directe begeleider ben jij degene die me het meeste heeft bijgebracht: bedankt voor de altijd informele gesprekken (gelukkig) en de vrijheid die je me liet tijdens het promotie-onderzoek. Veel dank ook aan mijn technisch, strategisch en sociaal (all-inclusive) mentor: Adrie de Jager. Frenkie V., bedankt voor al je compu-bijstand: Baywatch zal ik niet snel vergeten. Wat me brengt bij Anneriet, onze metingen hebben heel wat opgeleverd. Dagmar, bedankt voor je hulp en aanwezigheid in het begin. Tjeerd, bedankt dat je mijn promotor wilde zijn. Alle andere collega's van Fysica, bedankt dat jullie mijn gezanik (met te harde stem gebracht) zo lang aan hebben willen horen.

Ulrich, veel dank voor veel artikelen, het ga je goed in je Heimat. Misschien moeten we maar een lijntje leggen van Amsterdam via Wageningen en Nijmegen naar Magdeburg, kunnen we Wohaha, de Poetsvrouw en Carel Caputt nog eens interactief omleggen: heren, het (halve) leven zal nooit meer hetzelfde zijn. Uiteraard is er meer dan het Transitorium alleen. Bedankt mam en pap en alle dames en heren van vakanties, weekendjes weg, Pinkpop, carnaval, eten, drinken en alle andere écht belangrijke dingen. Tenslotte Christel, bedankt voor alles, toen, nu en straks.

Tom.

Zoea, vaerdig.

1

Introduction

General introduction

Water is the only substance on planet earth that occurs naturally in all three physical states: solid, liquid and gas. The liquid state of water is the most common and most important fluid in the world. Every organism needs water to live, and every organism contains at least some water. In plants for example water is used as the major cell content and serves as a solvent for biologically relevant solutes, it transports these solutes from roots to shoot or vice versa, it is the medium in which many biological reactions take place, it is a hydrogen donor in the carbon assimilation, et cetera. Water molecules are always in motion: continuous tumbles and collisions with each other cause the 'random walk' or self-diffusion of water. Although all individual molecules move, invisible for the human eye, the larger ensemble of molecules can be stationary or flowing from one region to another. The central theme of this Thesis is the movement of water within a certain time window, either by diffusion or by flow as measured by nuclear magnetic resonance imaging (NMRI or MRI). The ultimate strength of NMRI is the fact that it is non-invasive and therefore particularly useful for *in vivo* studies of the water status and/or water motion in biological objects.

In this Thesis the emphasis of the NMRI applications will be on plants. Recently, many papers have been published about the mechanisms of long-distance water transport in plants (1-5) after the introduction of the xylem pressure probe and cryo-scanning electron microscopy in plant physiology. The century-old Cohesion-Tension theory (6), which predicts large negative pressures in continuous water channels (long xylem vessels in the plant stem), has been questioned, but no satisfying alternative has been presented yet. In this debate another issue is not understood. Under extreme conditions (e.g. high transpiration of water from the

leaves and reduced water uptake by the roots, sub-zero temperatures of trunks) the continuous water column in a xylem vessel disrupts and the vessel fills with water vapor and air, blocking further water transport. Plants can refill these 'embolisms' (7-9) and new techniques and studies are required (9,10) to unravel the mechanisms controlling this refilling. In this Thesis it is shown that NMRi is a key tool in water transport and xylem refilling studies, creating the possibility to localize water flow non-invasively in intact plants, at the vascular tissue level or even at the individual vessel level.

Water in motion and NMR

In an NMR experiment two pulsed magnetic field gradients (PFGs) temporarily change the resonance frequency of the observed protons and thereby affect the amplitude and phase of the complex NMR signal (a short introduction in the principles of NMR can be found in Chapter 4 of this thesis, a thorough background can be found in references 11 and 12). Self-diffusion of protons between two PFGs results in an attenuation of the amplitude of the NMR signal, as Stejskal and Tanner reported in 1965 (13). If, in addition to self-diffusion (which is always present), the observed protons move uni-directionally in the direction of the PFGs, the phase of the NMR signal will shift as a result of the two PFGs (Fig. 1.1). If the amplitude g of the two PFGs is stepped, the NMR signal is modulated as a function of these steps. A Fourier Transformation of the modulated signal returns the distribution of displacements of the observed protons within Δ , also called a propagator (14). In Chapter 2 of this Thesis the signal modulation and propagator representation is described in more detail. A propagator can be obtained for every pixel of an NMR image (15) and can have many different shapes, depending on the amount of flowing protons and the size and nature of the displacements of the protons in the pixel concerned.

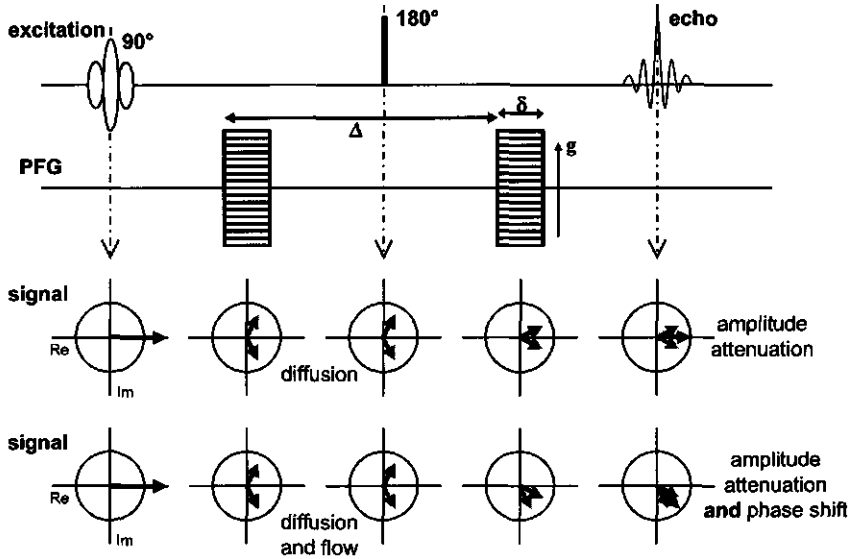


Figure 1.1: The modulation of the NMR signal by two pulsed field gradients with amplitude g , duration δ and spacing Δ . The two top lines represent the basic pulse sequence. The arrows in the circles in the bottom two lines schematically represent the complex signal of diffusing and flowing water during the different manipulations of the radiofrequency and gradient pulses. After signal excitation the signal resides along the real axis, where it gets dephased with the first PFG. With the 180° pulse all magnetization is inverted and with the second PFG the signal is rephased again. Protons that move along the PFG direction within Δ do not rephase exactly. If this movement is random (self-diffusion) the amplitude of the signal is attenuated. If, in addition to diffusion, the protons also move uni-directionally along the PFG direction (flow) the phase of the signal is also shifted.

NMR imaging of plants

NMR imaging of plants demands a special approach, as distinguished from other biological objects. Generally, the signal-to-noise ratio (SNR) of an NMR experiment depends on $B_0^{7/4}$ (with B_0 being the magnetic field strength) (16). This is the reason why many groups performing NMR microscopy move towards higher magnetic field strengths in a quest for a high spatial resolution of the image. Apart from the question whether this pursuit of the highest possible resolution is meaningful, plants impose a specific problem in high magnetic fields. Plants or plant tissues often have many intercellular spaces filled with air. Since air and water have different magnetic

susceptibilities, the density of magnetic field lines in air is different from the one in water, producing magnetic field inhomogeneities around every air-water interface; the higher the magnetic field strength, the stronger the field inhomogeneities.

The numerous local magnetic field inhomogeneities in many plant tissues can cause several image artifacts (17). The NMR signal after excitation is dephased rapidly because of the magnetic field inhomogeneities but can be refocused with an inversion pulse (180° pulse in Fig.1.1) in a spin echo. After the first 180° pulse and spin echo, a series or train of 180° pulses can refocus the signal over and over again. The amplitudes of the multiple spin echoes decay with a characteristic time constant: the spin-spin relaxation time T_2 . However, displacements of protons (due to self-diffusion) in the susceptibility-related field inhomogeneities can cause extra signal amplitude attenuation (as in the previous section: proton movements combined with magnetic field gradients attenuate the NMR signal). If the field inhomogeneities are large (at high B_0) the extra signal attenuation can also be dramatic and even the first spin echo image may already suffer from severe signal loss (18). Quantitative imaging of proton density and T_2 by fitting an exponential decay curve to the signal decay in the echo train now leads to erroneous T_2 and proton density images (18). Other imaging procedures in which the amplitude of the first echo image is modulated with e.g. PFGs also incorporate the signal losses due to the field inhomogeneities.

At lower magnetic field strength (0.47 and 0.7 T for all studies in this Thesis) the local magnetic field inhomogeneities are smaller. With large imaging gradients (compared to the field inhomogeneities), by using large spectral widths (~ 50 kHz), and short echo times the susceptibility problems can be overcome (18, 19) and the NMR signal can be recalled in as many as 1000 echoes (20). The disadvantage of a low magnetic field is of course the intrinsic low SNR. Much effort has to be put in obtaining a sufficiently high SNR by recording multiple spin echoes instead of a single echo, by signal averaging and by using a high filling factor of the radio-frequency coil.

Outline of this Thesis

Chapter 2 of this Thesis describes an NMR pulse sequence that combines fast NMR imaging with quantitative displacement studies using PFGs (the Pulsed Field Gradient Turbo Spin Echo sequence). After a detailed description of dynamic NMR microscopy (15), in which the NMR signal is modulated in both 'k-space' (for spatial localization) and 'q-space' (for displacement encoding), the combination with turbo spin echo (TSE) imaging is introduced. An elaborate description of the pulse sequence and of the processing of the forthcoming data is followed by several tests of the sequence with two artificial samples and a tomato plant.

In Chapter 3 of the Thesis a stimulated echo (STE) variant to the PFG TSE sequence in Chapter 2 is presented. The decay of the NMR signal in the labeling time between the PFGs in a spin echo sequence is controlled by T_2 . Proton displacements, originating from self-diffusion can only be distinguished from displacements originating from extremely slow flow (below ~ 0.3 mm/s) by using long labeling times. Long labeling times are also required to study effects of obstructions of the free diffusional pathway (restricted diffusion) of protons. If the observed protons have a short T_2 , relative to the required labeling time, the NMR-signal has vanished by the time the second PFG is applied. In these cases, it is advantageous to use a STE sequence instead of a spin echo pulse sequence, because the NMR-signal is then stored along the z-axis during most of the labeling time, where its decay is controlled by T_1 , and not by T_2 . Since T_1 is (often substantially) longer than T_2 the signal amplitude of a stimulated echo at a certain time can be significantly larger than the amplitude of a spin echo at that time, despite the inherent loss of half the signal in a STE sequence. The combination of a stimulated echo with PFG TSE in Chapter 3 is applied to extremely slow flowing water in a phantom, diffusion in a maize plant as a function of labeling time and flow localization in a tomato pedicel. In the addendum to Chapter 3 a pulse sequence is presented, in which the echo train after magnetization preparation with the PFGs is not used to fasten imaging time, but to record an echo decay for every pixel and every PFG step.

Chapter 4 deals with the analysis of the propagators, measured with the two pulse sequences. A propagator often represents both flowing and stationary water. If the (symmetrical) stationary part of the propagator is subtracted from the total propagator, the flowing part remains and can be quantified. The flow characteristics can be calculated by relating intensities of the flowing part of the propagator to the total intensity of pixel-propagators of water in a reference tube (100% water calibration). For a stem segment of a chrysanthemum flower the total volume flow, calculated from NMR experiments, is compared to the water uptake of that stem segment, simultaneously measured with a precision balance.

Chapter 5 focuses on functional imaging of plants by a combination of imaging T_2 , amplitude (or proton/water density) and flow characteristics in an extensive study of an intact cucumber plant. A high imaging resolution can be used to discriminate between different tissues on the basis of T_2 , water density or flow characteristics; the signal of the pixels in the different tissues can then be added (to increase the SNR) and analyzed for a second time. In this way bi-exponential decay curves can be observed in different tissues of a transverse image of the stem of the cucumber plant, and flow characteristics of different vascular bundles can be studied in time.

In Chapter 6 the possibility of studying transients in flow characteristics in the cucumber plant is applied to a specific phenomenon of the plant, related to water transport. If the roots of a cucumber plant are cooled, water uptake by the roots is severely inhibited: in a short time the plant loses more water than it takes up and wilts. After rewarming the roots to the original temperature, the plant recovers from its water loss within hours leaving no visual trace of the cooling event. Imaging the flow characteristics for every pixel in the stem of a cucumber plant revealed interesting transients in the xylem of the plant during and after the environmental changes, which raises new issues in the continuous debate about water transport in plants.

In the final Chapter a strategy is discussed of imaging plants at low magnetic field strength and the optimal use of the two pulse sequences and the analysis of the propagators. Difficulties with a large spectrum of displacements within the labeling

time (from diffusion to high flow velocities) are addressed, together with the question if a high spatial resolution is always desirable.

References

1. J. B. Passioura, *Bot. Acta*, **104**, 405-411 (1991).
2. U. Zimmermann, F. C. Meinzer, R. Benkert, J. J. Zhu, H. Schneider, G. Goldstein, E. Kuchenbrod and A. Haase, *Plant Cell Environ.* **17**, 1169-1181 (1994).
3. M. J. Canny, *Ann. Bot.* **75**, 343-357 (1995).
4. J. A. Milburn, *Ann. Bot.* **78**, 399-407 (1996).
5. M. T. Tyree, *J. Exp. Bot.* **48**, 1753-1765 (1997).
6. H. H. Dixon and J. Joly, *Philos. Trans. R. Soc. Lond. Ser. B-Biol. Sci.* **186**, 563-576 (1894).
7. M. J. Canny, *Am. J. Bot.* **84**, 1223-1230 (1997).
8. M. A. Zwieniecki and N. M. Holbrook, *Plant Physiol.* **123**, 1015-1020 (2000).
9. M. T. Tyree, S. Salleo, A. Nardini, M. A. o Gullo and R. Mosca, *Plant Physiol.* **120**, 11-21 (1999).
10. N. M. Holbrook and M. A. Zwieniecki, *Plant Physiol.* **120**, 7-10 (1999).
11. T. C. Farrar and E. D. Becker, *Pulse and Fourier transform NMR*, New York, London: Academic Press (1971).
12. P. T. Callaghan, *Principles of nuclear magnetic resonance microscopy*, Oxford: Clarendon Press (1991).
13. E. O. Stejskal and J. E. Tanner, *J. Chem. Phys.* **42**, 288-292 (1965).
14. J. Kärgler and W. Heink, *J. Magn. Reson.* **51**, 1-7 (1983).
15. P. T. Callaghan, C. D. Eccles and Y. Xia, *J. Phys. E.* **21**, 820-822 (1988).
16. D. I. Hoult and R. E. Richards, *J. Magn. Reson.* **24**, 71-85 (1976).
17. K. M. Lüdecke, P. Röschmann and R. Tischler, *Magn. Reson. Imag.* **3**, 329-343 (1985).
18. H. C. W. Donker, H. Van As, H. T. Edzes and A. W. H. Jans, *Magn. Reson. Imag.* **14**, 1205-1215 (1996).
19. C. J. Rofe, J. Van Noort, P. J. Back and P. T. Callaghan, *J. Magn. Reson.* **108**, 125-136 (1995).
20. H. T. Edzes, D. van Dusschoten and H. Van As, *Magn. Reson. Imag.* **16**, 185-196 (1998).

2

Microscopic displacement imaging with pulsed field gradient turbo spin echo NMR

T.W.J. Scheenen, D. van Dusschoten, P.A. de Jager and H. Van As

We present a pulse sequence that enables the accurate and spatially resolved measurements of the displacements of spins in a variety of (biological) systems. The pulse sequence combines Pulsed Field Gradient (PFG) NMR with Turbo Spin Echo (TSE) imaging. It is shown here that by ensuring that the phase of the echoes *within a normal spin echo train is constant, displacement propagators can be generated on a pixel by pixel basis. These propagators accurately describe the distribution of displacements, while imaging time is decreased by using separate phase encoding for every echo in a TSE train. Measurements at 0.47 T on two phantoms and the stem of an intact tomato plant demonstrate the capability of the sequence to measure complete and accurate propagators, encoded with 16 PFG-steps, for each pixel in a 128 x 128 image (resolution 117 x 117 x 3000 μm) within 17 minutes. Dynamic displacement studies on a physiologically relevant time-resolution for plants are now within reach.*

Also published in Journal of Magnetic Resonance 142: 207-215 (2000)

Parts of this work have been presented at the Fourth International Conference on Magnetic Resonance Microscopy and Macroscopy in Albuquerque, New Mexico, USA on Sept. 20-24, 1997 (1).

Introduction

Diffusion and transport processes of water in objects like tissues, soils, model systems, plants, food, separation columns, bioreactors, biofilms, etc. are of interest for researchers in many different fields. Some problems can arise when complex porous systems like vegetable or animal tissues are monitored: the water status of the studied system can change fast; water flow profiles and diffusional properties (e.g. restrictions) are generally unknown. Dynamic NMR-microscopy (2) provided the means to study the distribution of water displacements microscopically and non-invasively in a wide variety of systems. This method combines NMR imaging with quantitative displacement studies using Pulsed Field Gradients (PFGs).

Since the water status of a plant can change within half an hour, dynamic studies of that status should be at a physiologically relevant time-scale of less than twenty minutes. Because the flow profile and diffusive behavior of the plant tissue are not known a complete distribution of displacements within a certain time has to be constructed for every pixel of an image and the SNR of the properties of interest must be sufficiently high to produce results with acceptable accuracy. The standard dynamic NMR-experiment, in which an image with $n \times n$ picture elements is recorded, combined with m gradient steps to encode for displacement takes $n \times m$ acquisitions to complete. Consequently, the total acquisition time may exceed several hours (3, 4), and changes within the measurement time will be averaged out over the experiment. Therefore, a faster way of performing the dynamic NMR-experiment is needed in plants.

The time resolution of a PFG NMR imaging experiment can be increased by reducing the number of phase and flow encoding steps (5, 6). Reducing the number of phase encoding steps directly reduces the spatial resolution in one direction of the images, which is not desirable in plants where the small tissue dimensions require an in-plane resolution in the order of $100 \times 100 \mu\text{m}$. Rokitta *et al.* assumed a certain flow-profile for the observed spins and fitted the signal, attenuated by a reduced number of flow encoding steps, to a model function. Another approach to decrease measurement time is the use of an echo train. Echo Planar Imaging (EPI, (7, 8)) is not applicable in plants, because intercellular spaces in plant tissues

cause magnetic field gradients in the sample and shorten the T_2^* drastically (e.g. <40 ms). In a 180° pulse train with normal spin-echoes the signal decays under the influence of the longer T_2 . The multiple spin-echoes can be used to step rapidly through k-space by phase-encoding the echoes separately (Turbo Spin Echo, TSE or RARE, (9)). TSE is used here with the new feature that all echoes in the train can be acquired with constant and coherent amplitude and phase, which is a prerequisite for combining dynamic NMR-microscopy with TSE. Thus not only the signal amplitude attenuation can be measured as a function of the PFGs (10) but also the phase-development, containing flow information.

Theory

The displacement of an ensemble of spins in a magnetic field can directly be measured by the use of two gradient pulses g of duration δ and spacing Δ (see Fig. 2.1). A uniform displacement \mathbf{R} of the spins results in a phase shift ϕ of the NMR signal:

$$\phi = \gamma \delta \mathbf{g} \cdot \mathbf{R} \quad [2.1]$$

in which γ is the gyromagnetic ratio of the spins observed. If the displacement of the spins within the observation time Δ is not uniform but completely random, e.g. diffusion in a non-flowing liquid with a self-diffusion constant D , there will be no phase shift but only an attenuation of the NMR-signal amplitude $S(\mathbf{g})$ vs. g normalized to the signal amplitude $S(0)$ at $g = 0$ (11):

$$S(\mathbf{g})/S(0) = \exp(-\gamma^2 \mathbf{g}^2 \delta^2 D(\Delta - \delta/3)) \quad [2.2].$$

If the displacement-behavior of the ensemble of spins under observation is known *a priori*, e.g. for pure uniform diffusion or plug flow, an experiment with two g -values ($g = 0$ and $g = x$) would be enough to determine the flow velocity and the diffusion constant of the spins. Quantification problems emerge if the displacement-behavior

of individual spins in the ensemble is not known. Experiments with two g -values can only result in one weighted mean flow velocity or diffusion coefficient (12-17).

As soon as a biological system is studied, multiple spin ensembles that differ in diffusion constants and flow-velocities contribute to the NMR-signal in both spatially unresolved measurements and even in individual pixels of a high-resolution image. To correctly quantify the unknown displacement-behavior of the observed ensemble of spins one has to measure the NMR-signal $S(\mathbf{g})$ as a function of \mathbf{g} (18). In that case the NMR-signal is a superposition of phase terms $\exp(i\gamma\delta\mathbf{g} \bullet (\mathbf{r}'-\mathbf{r}))$ derived from Eq. [2.1] weighted with the spin density $\rho(\mathbf{r})$ at a position \mathbf{r} multiplied by the probability $P(\mathbf{r} | \mathbf{r}', \Delta)$ that a spin moves from position \mathbf{r} to position \mathbf{r}' in time Δ :

$$S(\mathbf{g}) = \int \rho(\mathbf{r}) \int P(\mathbf{r} | \mathbf{r}', \Delta) \exp(i\gamma\delta\mathbf{g} \bullet (\mathbf{r}'-\mathbf{r})) d\mathbf{r}' d\mathbf{r} \quad [2.3].$$

By defining a reciprocal space $\mathbf{q} = \gamma\delta\mathbf{g}/2\pi$ and a dynamic displacement $\mathbf{R} \equiv \mathbf{r}'-\mathbf{r}$, independent from the initial spin position and density, Eq. [2.3] can be rewritten as:

$$S(\mathbf{q}) = \int \bar{P}(\mathbf{R}, \Delta) \exp(i2\pi\mathbf{q} \bullet \mathbf{R}) d\mathbf{R} \quad [2.4a]$$

$$\bar{P}(\mathbf{R}, \Delta) = \int S(\mathbf{q}) \exp(-i2\pi\mathbf{q} \bullet \mathbf{R}) d\mathbf{q} \quad [2.4b].$$

This demonstrates the Fourier relationship between $S(\mathbf{q})$ and $\bar{P}(\mathbf{R}, \Delta)$. So by monitoring $S(\mathbf{q})$, the NMR-signal as a function of \mathbf{q} , a Fourier Transform of $S(\mathbf{q})$ results in the averaged probability distribution of displacements of all spins observed: the averaged propagator, $\bar{P}(\mathbf{R}, \Delta)$.

The mean square displacement σ^2 due to (unrestricted) diffusion is proportional to the corrected observation time $(\Delta-\delta/3)$ and results in a Gaussian propagator positioned at the mean displacement p of the observed water molecules:

$$\bar{P}(\mathbf{R}) = A \exp\left(-\left(\frac{\mathbf{R}-p}{\sigma}\right)^2 / 2\right) \quad [2.5].$$

For stationary water the mean displacement is zero resulting in a Gaussian distribution of $\bar{P}(\mathbf{R})$ with amplitude A and center position $p = 0$. The mean square displacement σ^2 can be used to calculate the diffusion coefficient of the water through:

$$\sigma^2 = 2D\left(\Delta - \frac{\delta}{3}\right) \quad [2.6].$$

The probability distribution function for water flowing laminarly through a tube is the unit step function:

$$\begin{aligned} \bar{P}(\mathbf{R}) &= C && \text{for } 0 < \mathbf{R} < \mathbf{R}_{\max} \\ \bar{P}(\mathbf{R}) &= 0 && \text{for } \mathbf{R} < 0 \text{ and } \mathbf{R} > \mathbf{R}_{\max} \end{aligned} \quad [2.7]$$

where C is a constant and \mathbf{R}_{\max} is the maximum displacement of the water in the tube within Δ . Since flowing water also exhibits diffusion the unit step function is broadened and the borders at $\mathbf{R} = 0$ and $\mathbf{R} = \mathbf{R}_{\max}$ appear as half Gaussians instead of sharp edges of the propagator.

When q-space imaging is combined with normal NMR imaging one can perform so-called dynamic microscopy experiments, a term which was first named by Callaghan (2). In conventional imaging the signal in time t evolves under the influence of a gradient G encoding for position (in two dimensions). Diffusion and flow in the direction of the imaging gradients might introduce extra signal attenuation, if the imaging gradients are of significant size compared to the PFGs. However, this extra signal attenuation, if any, will not vary as a function of the PFGs but will be equal for every step in q-space. Therefore the imaging gradients will not effect the shape of the propagator. So incorporating the well-known k-space description for imaging

$$S(\mathbf{k}) = \int \rho(\mathbf{r}) \exp(-i2\pi\mathbf{k} \cdot \mathbf{r}) d\mathbf{r} \quad [2.8]$$

with $\mathbf{k} = \gamma\delta G/2\pi$ in Eq. [2.4] the total signal as a function of k- and q-space is

$$S(\mathbf{k}, \mathbf{q}) = \int \rho(\mathbf{r}) \exp(i2\pi \mathbf{k} \cdot \mathbf{r}) \int \bar{P}(\mathbf{R}, \Delta) \exp(i2\pi \mathbf{q} \cdot \mathbf{R}) d\mathbf{R} d\mathbf{r} \quad [2.9].$$

The result of such a microscopic displacement measurement is a series of conventional images, obtained after a two dimensional Fourier Transform with respect to \mathbf{k} , which contains the propagator of the spins after Fourier Transform with respect to \mathbf{q} in the third dimension.

Materials and Methods

The pulse sequence

Figure 2.1 shows an outline of the Pulsed Field Gradient Turbo Spin Echo (PFG TSE) pulse sequence. This sequence is a combination of two techniques: the Pulsed Field Gradient Carr Purcell (PFG CP) sequence (19) and the Turbo Spin Echo technique, also known as RARE (9), originating from the idea to use multiple echoes to phase-encode the NMR-signal (7). The improvement of this sequence compared to previous reports on PFG TSE (10) involves the ability to maintain a constant amplitude and phase throughout the echo train. This is the property that enables the combination of encoding for flow with PFGs and decreasing the acquisition time with the TSE technique. Below a short description of the sequence follows.

In the first part of the sequence a selective 90° pulse induces magnetization perpendicular to the static magnetic field in a selected slice. This magnetization is encoded for displacement by two ramped PFGs in the slice direction. The amplitude of g is varied from $-g_{\max}$ via zero to $+g_{\max-1}$ in m steps. In calculating the effective duration δ of a PFG, one ramp is included. Δ Can be varied by changing the first echo time $t_{e,1}$ and additional 180° pulses with variable spacing τ (20) can be inserted between the two PFGs. The signal is not stored along the z -axis during $\Delta - \delta$ as in a Stimulated Echo (STE) sequence (21, 22), but remains in the xy -plane. In the xy -plane the additional 180° pulses are used to overcome susceptibility problems by refocusing the signal. The XY-8 phase scheme $(xyxyxyx)_n$ is used to

avoid losing the phase dispersion imposed by the first PFG in the time between the two PFGs due to r.f. pulse imperfections (19, 20).

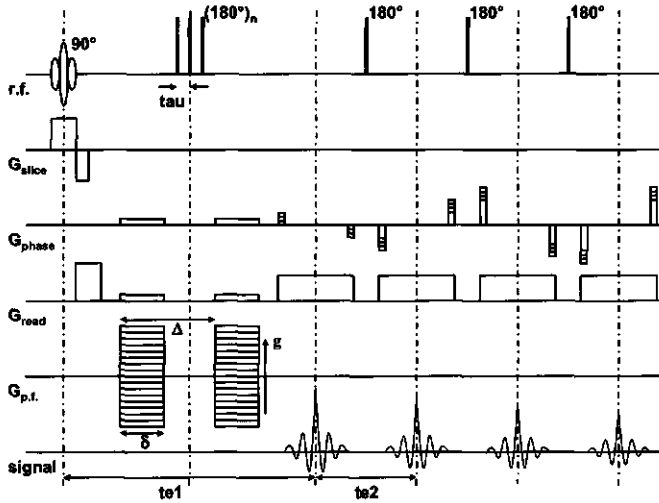


Figure 2.1: The Pulsed Field Gradient Turbo Spin Echo pulse sequence. All directions show a pair of crusher gradients around the first (train of) 180° pulse(s). In the direction of the displacement encoding PFGs (the slice direction) the crushers are negligible compared to the PFGs.

In the second part of the sequence the displacement encoded complex NMR-signal is phase-sensitively recorded in a train of spin-echoes. The cumulative error of imperfect 180° pulses is now overcome by using an MLEV-4 ($x - x - x x$)_n phase pattern in the pulse train, which performed best with the used instrumental set-up (23). The use of spin-echoes compared to gradient-echoes has the advantage that the decay in signal amplitude of the echoes in the train is governed by T_2 instead of T_2^* , which is the case in an EPI-experiment (12, 15). This advantage turns into an absolute necessity if samples with very short T_2^* s are studied. The susceptibility problems in plants can only be overcome by using a spin-echo train. The combination of short hard 180° pulses ($24 \mu\text{s}$) and strong, fast switching gradients ($100 \mu\text{s}$ ramps) enables short echo times (4.60 ms) at a spectral width of 50 kHz and 128 sample points. The receiver acquires data with a high duty cycle (2.56 ms acquisition in every 4.60 ms echo). The signal attenuation due to the short T_2^* is negligible compared to the controlled signal attenuation resulting from the high read out gradient to ensure that the observed resolution of the image is the same as the calculated resolution (24, 25).

The number of echoes in the r.f. pulse train used for phase encoding the NMR-signal (the turbo-factor tf) is variable and is determined largely by the T_2 of the sample. Figure 2.2 shows the k-space raster for an experiment in which 8 scans with 32 echoes form two images. The center of k-space, around $k_y = 0$, is sampled with the first two echoes of the 8 scans. All subsequent echoes are placed symmetrically around $k_y = 0$. This way, the T_2 relaxation in the echo train leads to a stepped decrease of the signal amplitude in k-space from $k_y = 0$ to the borders of k_y . The choice in the number of echoes is a compromise between measurement time and resolution. If too many echoes are used, the signal of those pixels with short T_2 s decays too much resulting in a heavy filtering in the k_y -direction: the intensity of the pixel containing water with the short T_2 s is distributed over neighboring pixels in the phase encoding direction. Different trajectories through the k_y -direction should minimize this artificial spreading (26). Furthermore, to reduce unwanted recombination of phase encoding gradients every echo is phase encoded differently from its neighboring echoes. This is possible by rewinding the phase gradient after each echo (27).

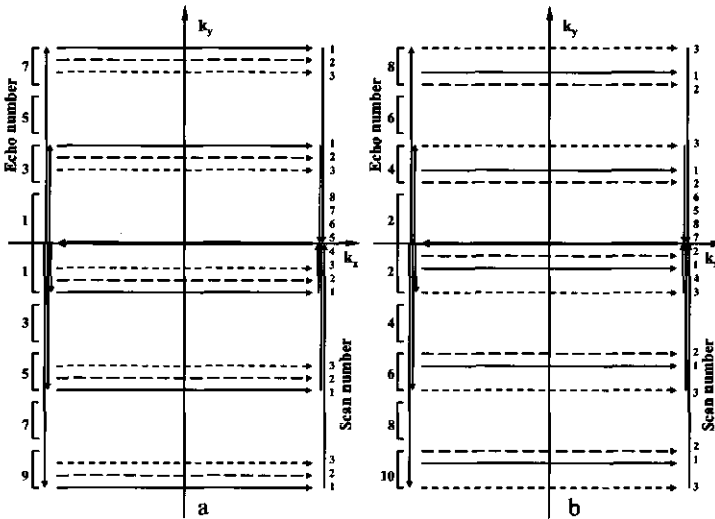


Figure 2.2: The k-space raster for a 128 x 128 image obtained in 8 scans. The first echoes of the eight scans form the center of k-space for the odd echoes image (a), the second echoes of the eight scans form the center of k-space for the even echoes image (b). The third and all other odd echoes are placed symmetrical around the center of the k-space raster for the odd echo image, just like the fourth and further even echoes are placed symmetrical around the center of the k-space raster for the even echo image.

It should be noted that the phase of the odd and even echoes is not exactly the same but remains constant for both types of echoes throughout the echo train. Therefore the odd and even echoes are separately phase-encoded to form two completely separate images (see k-space trajectory in Fig. 2.2). Using e.g. a tf of 32 means that for images of n^2 pixels $2n/tf$ scans are acquired in which 16 odd and 16 even echoes are used for phase encoding the signal, resulting in two n^2 complex images: one from the even and one from the odd echoes. After phase correction, the two complex images are summed to increase the SNR.

In the first and second part of the sequence hard 180° pulses are used, since they are short. Residual magnetization of the hard pulses in the xy plane is suppressed with gradients: crusher pairs are applied in three directions. In the direction of the displacement encoding PFGs the crushers are of negligible size compared to the PFGs. The dephasing read out gradient is applied before the first 180° pulse, so refocusing of initial magnetization of the soft 90° pulse will not occur at the same time as any residual magnetization from the hard pulses in the read out direction. A disadvantage of using hard 180° pulses instead of soft pulses in combination with slice gradients is that the time between scans cannot be used to measure a different slice, because the whole sample is excited with the pulses. A multislice experiment is still possible but requires different measurement conditions (longer echo times or larger spectral width) as a single slice experiment (28).

If averaging is necessary to increase the SNR of the images DC artifacts are subtracted by taking an even number of averages in which the phase of the soft 90° pulse is shifted by π for every scan. If averaging is not performed a DC-correction is made by subtracting the mean level where no signals are present from the echoes.

Measurement objects and spectrometer

Three objects were used to test and illustrate the possibilities of the pulse sequence: two phantoms and a tomato plant. The first phantom consisted of six small test tubes filled with water, doped with different concentrations of $MnCl_2$ to vary the T_2 . This was done in order to study the effect of the different T_2 s on the quality of the TSE images and the effect on the single pixel propagators. The

second phantom, used to evaluate the accuracy of measuring flow with the PFG TSE imaging sequence, was a test tube (i.d. 3.0 cm) filled with doped water (tap water with CuSO_4). Inside the test tube with stationary water was a second, empty test tube and a third, flexible, looped tube with water passing through the r.f. coil two times: flowing up and down. The flow rate through the flexible tube was controlled with a Waters 4000 HPLC pump (Waters Corporation, Milford, Massachusetts, USA). The final object was a 60-cm tall, ten weeks old, tomato plant. The plant, including pot, was put in the instrumental set-up (light intensity approx. 150 Lux, relative humidity 65% and air temperature 26°C) two days before measurements and was flowering during the measurement.

The spectrometer was an SMIS console (SMIS Ltd., Guildford, Surrey, UK), operating at 20.35 MHz, equipped with an electromagnet (Bruker, Karlsruhe, Germany), which generates the 0.47 T field over a 14 cm air gap and is stabilized by the use of an external ^{19}F lock unit (SMIS). The phantoms and the tomato plant were measured in a custom-engineered gradient and r.f. probe (Doty Scientific Inc., Columbia, South Carolina, USA) with a 45 mm (i.d.) cylindrical central bore, accessible from both ends. The 48 mm solenoid r.f. coil is surrounded by a set of actively shielded gradients (maximum strengths are 0.60, 0.51 and 0.60 T/m for the x, y and z-direction, respectively). For the measurements on the tomato plant the probe's r.f. coil was detuned and an extra solenoid r.f. coil with an i.d. of 15 mm, directly wrapped around the plant stem, was inserted in the 45 mm bore gap of the gradient probe, increasing the SNR by a factor of approx. $48/15 \approx 3$ (29).

Signal processing

A dataset of m images with n^2 pixels obtained with the PFG TSE pulse sequence contains three dimensions of complex data. The first dimension contains n sample points in which one echo is read out. The second dimension is composed of a number of views ($2n/TF$) and echoes (TF), which are necessary to form the total of n phase encoding steps for two images. The third dimension holds the m PFG steps. The primary data handling involves reshuffling the different views and echoes into n phase encoding steps for two images in the correct order with respect to k_y . The complex k -space data is Fourier Transformed and here the main reason for obtaining two complete complex images emerges: the image constructed from the

odd echoes is shifted slightly in the phase encoding direction (less than one pixel) with respect to the image of the even echoes. A first order phase correction in the phase encoding direction before the Fourier Transform minimizes the difference in position of the sample in the two images.

Subsequently, zero and first order phase corrections of the even and odd echo images at $g = 0$ are performed in both image directions and used to correct the displacement encoded images. Furthermore, a linear phase shift of the total images with respect to g is caused by a PFG-dependent B_0 field shift and is corrected by zeroing the phase of stationary water either in a reference tube or in the studied object. Finally, the PFG-direction or q -space data is zero-filled once and Fourier Transformed to form a complex propagator for every pixel in the even and odd images. The propagators of the odd images are mirrored and shifted by one point to enable the addition of the odd and even images to one final image set (so-called propagator images). The real part of this set contains the propagators whereas the imaginary part only contains noise. The width of the displacement axis of the propagator is determined by $1/\gamma g_{step} \delta$. In the 3D FT no filtering is applied. All data handling is performed in IDL (RSI, Boulder, Colorado, USA).

Results

The phantoms

The T_2 values of the six test tubes in the first phantom varied over a range of three decades. To measure these T_2 s we used a multi-echo experiment with a train of 48 echoes (echo time $n \cdot 4.6$ ms) to obtain a series of images with decreasing intensity. For every pixel in the images the real part of the complex signal attenuation (after phase correction) in the echo train was fitted to a mono-exponential decay to calculate values for T_2 and the initial signal amplitude (23). Table 2.1 contains the calculated values of mean T_2 and initial signal amplitude and standard deviations for every tube: T_2 values range from 5.4 msec to 1.5 sec. The mean signal amplitude for every tube was calculated from only those pixels (around 45 for every tube) that were completely filled with water: we did not use pixels near edges to

exclude partial volume effects. Since partial volume effects do not significantly influence signal attenuation we did use partially filled pixels to calculate T_2 values; for the mean T_2 values around 80 pixels were used for calculations. In the calculated mean amplitudes the amplitudes of tubes II up to VI are comparable.

Table 2.1: Mean values and standard deviations (SD) of the following calculated parameters for the six different tubes in the first phantom: the T_2 , the signal amplitude at the moment of excitation (amp), the self-diffusion constant in the propagator (D_1) and the self-diffusion constant in the Stejskal-Tanner plot (D_2).

tube	[MnCl ₂] mmol/l	T_2 ms	SD ms	Amp a.u.	SD a.u.	D_1 $10^9 \text{m}^2/\text{s}$	SD $10^9 \text{m}^2/\text{s}$	D_2 $10^9 \text{m}^2/\text{s}$	SD $10^9 \text{m}^2/\text{s}$
I	0.0	1.5×10^3	4.5×10^3	10.2	0.6	2.20	0.16	2.20	0.19
II	0.2	118	3	25.8	1.1	2.19	0.13	2.24	0.13
III	0.4	59.8	2.1	26.1	1.1	2.18	0.18	2.27	0.17
IV	0.8	29.2	1.3	24.6	1.4	2.23	0.13	2.37	0.22
V	2.5	8.3	1.7	22.7	1.8	2.18	0.16	2.30	0.30
VI	5.0	5.4	0.5	23.8	3.4	2.08	0.29	1.97	0.40

Only tube I shows a lower amplitude, because of partial saturation: the low signal intensity and the long T_2 (and therefore long T_1) compared to t_r result in an inaccurate estimation of T_2 and an underestimated calculated amplitude (see Table 2.1).

Figure 2.3a shows an image of the same six tubes filled with doped water, acquired with the PFG-TSE sequence at $g = 0$. Although the first echo in the experiment is at 13.0 ms after excitation, one can still observe tube VI with a T_2 of 5.4 ms. The effect of smearing of these short T_2 s in the vertical, phase encoding direction of the images is clear in tube V and VI and some vertical ghosting is present around tube IV and V (maximum intensity around 7% of maximum intensity in the tube). Subsequently, we obtained propagator images for the six tubes phantom and subjected all propagators to a non-linear least-squares fit to a Gaussian function (Eq. [2.5]) using the Levenberg-Marquardt method (30). To calculate the diffusion

constant D from σ we used Eq. [2.6]. These results are presented in Fig. 2.3b. The data from the PFG-TSE experiment was also analyzed in the same manner as proposed by Stejskal and Tanner (Eq. [2.2], (11)): a weighted least-squares linear fit of $\ln(S(g)/S(0))$ to $\gamma^2 g^2 \delta^2 (\Delta - \delta/3)$ for every pixel resulted in a D map. The mean D and its standard deviation (SD) for each tube in the images is summarized in Table 2.1. We take $2.20 \times 10^{-9} \text{ m}^2/\text{s}$ to be the self-diffusion constant D for free water.

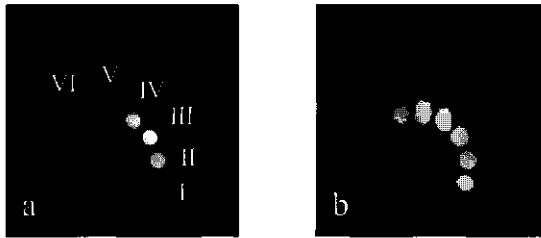


Figure 2.3: Images of six tubes with doped water. (a) The real part of the complex signal at $g = 0$ of a PFG-TSE experiment. (b) D for every pixel, calculated through Eq. [2.5], with σ derived from the fit to the propagator. Parameters: Image size 128×128 pixels, field of view (FOV) 55 mm, t_0 13.0 ms, t_e 4.6 ms, Δ 6.26 ms, δ 3.5 ms, t_r 480 ms, slice thickness 3 mm, 16 PFG steps, PFG_{max} 0.457 T/m, t_f 16, measurement time 4 min 23 s, T 24°C.

Propagator images of the second phantom (Fig. 2.4a) were fitted to Eq. [2.5]. The propagators of three pixels (solid lines), one pixel with stationary water, one pixel in the middle of the tube with water flowing up and one pixel in the middle of the tube with water flowing down, with their fits (dashed lines) to the Gaussian function are displayed in Fig. 2.4b. Since displacement caused by coherent flow is proportional to Δ , the position p of the fit to the Gaussian function corresponds to the mean displacement of the water in the observed pixel within Δ . Figure 2.4c displays p for every individual pixel of the slice through the phantom. The maximum displacement of the water flowing up and down through the slice was measured at 60.8 and 58.9 μm within Δ , respectively. These values correspond to linear flow velocities of 4.76 and 4.62 mm/s. The forced water volume flow of the pump was set to $16.7 \text{ mm}^3/\text{s}$, which, assuming a laminar, parabolic flow profile exists within the tube (i.d. 3.0 mm), results in a maximum linear velocity of 4.72 mm/s.

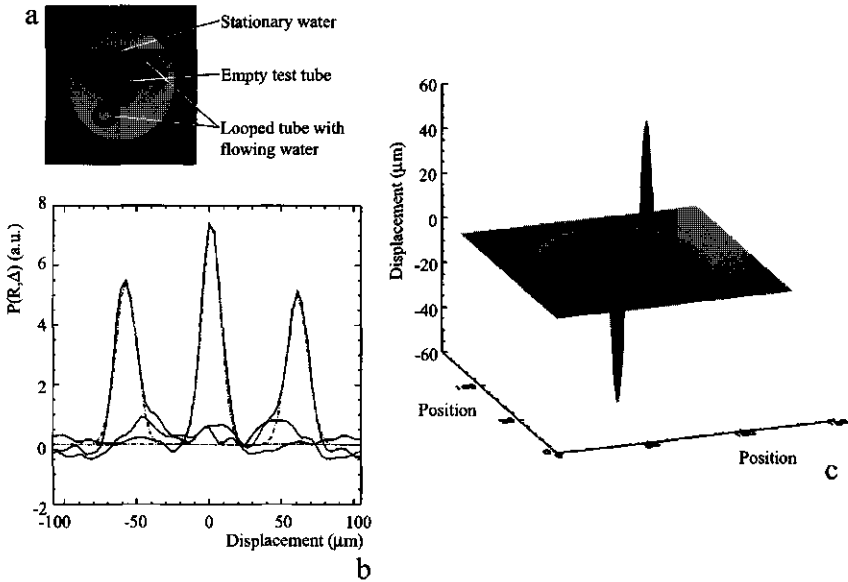


Figure 2.4: Summary of data of the phantom with stationary and flowing water. (a) An image at $g = 0$, perpendicular to the axes of the tubes. (b) The propagators of three individual pixels (solid lines) and their fits to the Gaussian function (dashed line). One pixel contains stationary water, one pixel with maximum flow up and one with maximum flow down through the slice. (c) Mesh plot of the spatial distribution of displacements. The countercurrent flow of water results in two anti-symmetrical parabolic profiles in the tube with flowing water. Parameters: FOV 40 mm, t_e1 20.2 ms, t_e2 4.8 ms, Δ 12.76 ms, δ 4.5 ms, t_r 1700 ms, slice thickness 3 mm, 32 PFG steps, PFG_{max} 0.385 T/m, t_f 32, measurement time 16 min 30 s, T 24°C, volume flow 1.00 ml/min.

Additionally Eq. [2.1] predicts a linear relation between the phase of the NMR-signal and the displacement of the spins in time Δ . When the phase of the signal of the center of the tubes was fitted to Eq.[2.1] we found a maximum linear velocity of 4.81 mm/s (flowing up) and 4.52 mm/s (flowing down). The correct value should be 4.72 mm/s, as reported earlier.

The Tomato Plant

The most demanding object in terms of time resolution and spatial resolution, but also the most interesting object in terms of dynamics presented here is the stem of a tomato plant. Figures 2.5a and 2.5b show single parameter images of the amplitude and T_2 of the stem of the tomato plant, acquired in the same manner as described for the first phantom. The TSE image at $g = 0$ is shown in Fig. 2.5c. One

can observe that the stem mainly consists of spongy parenchyma with large cells, which results in high values for T_2 . In the center of the stem a cavity is visible where no signal is detected. The outer rings of the stem, from the ring with lower intensity near the middle and three broadened regions visible in the amplitude image, up to the surface of the stem contain transport vessels with supporting tissues and fibers. T_2 values in the outer rings show more diversity because of the different cell structures and sizes (31), which occur there. The dot on the lower right side of the images is a reference tube with doped water. The reference tube axis is not exactly perpendicular to the image plane so its image is somewhat elliptical.

The pixel size of this image-set containing the single pixel propagators is $117 \times 117 \times 3000 \mu\text{m}$. From microscopic studies we know that the internal diameters of the xylem vessels in the stem range from approximately 10 to $160 \mu\text{m}$ (32). Distances between individual xylem vessels are in the same order of magnitude.

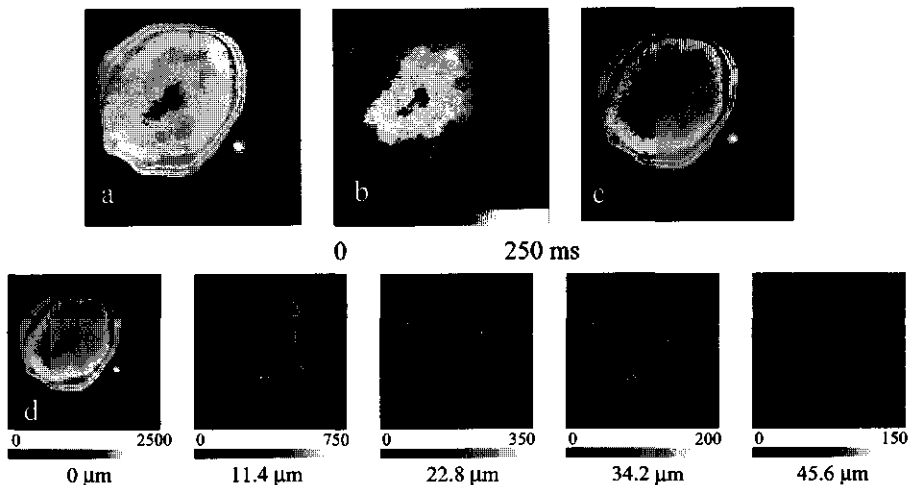


Figure 2.5: Images of a transverse slice through the stem of the tomato plant. (a) A calculated amplitude image. (b) A calculated T_2 image. (c) A TSE image at $g = 0$ of the real signal amplitude after phase-correction. (d) Images of the real signal amplitude at calculated displacements of 0, 11.4, 22.8, 34.2 and $45.6 \mu\text{m}$. The shown signal intensities are in arbitrary units. Parameters a+b: FOV 14 mm, t_e1 8.6 ms, t_e2 5.2 ms, t_r 1500 ms, slice thickness 3 mm, acquisition time 32 min, T 26°C . Extra parameters c+d: FOV 15 mm, t_e1 17.2 ms, Δ 9.56 ms, δ 4.5 ms, t_r 800 ms, 16 PFG steps, PFG_{max} 0.457 T/m , t_f 32, measurement time 17 min 8 s.

Since most xylem vessel radii are smaller than the pixel size there will probably be no pixels in the images that contain only flowing water. Using the information contained in the propagator images, images can be constructed representing the propagator intensity for a certain displacement. A series of such images (Fig. 2.5d) gives an overview of the water displacement in the slice. In this way one can detect three areas with pixels with low amplitudes at 0 μm displacement but high intensity at larger displacement. The pixels in these areas resemble volume-elements in which water is transported upwards in the plant and they coincide with the regions with active xylem vessels of the tomato plant (32).

The propagator of one pixel in the active xylem area is displayed in Fig. 2.6, together with the propagator of a pixel in the reference tube. The propagator of the pixel in the xylem area shows displacements within Δ up to 30 μm , which corresponds to a flow velocity of 3.1 mm/s. The shape of the 'flowing' part of this propagator is not simply a Gaussian broadened step function, which would be the case for laminar flow in a single xylem vessel only (Eq. [2.7]). Apparently the volume element corresponding to the pixel with the propagator shown in Fig. 2.6 contains more than one vessel with flowing water. It might hold a part of a second vessel with flowing water that causes more signal than expected in the lower displacements (10 to 20 μm) of the propagator.

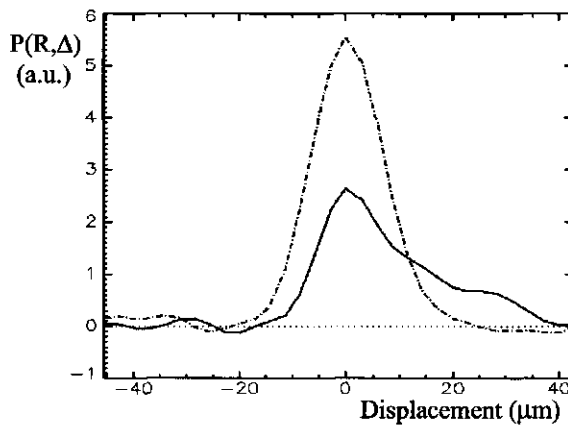


Figure 2.6: The propagator of a pixel in the reference tube (dashed line) and a pixel in one of the three areas of the tomato plant that show flow (solid line).

Discussion and Conclusions

The amplitude images (Figs. 2.3a, 2.4a and 2.5c) of the different objects show that the TSE part of the sequence produces real images without unexpected artifacts. This means that the amplitude and phase of the NMR-signal throughout the echo train is constant which is a prerequisite for calculating real images and for monitoring flow-induced phase shifts within the echo train.

The calculation of D of the stationary water in the six tubes of the first phantom by the fit of the propagator to a Gaussian function resulted in values around the value of D for free water at 24°C (Table 2.1). The error in D , which is 8% or smaller for tubes 1 to 5, remains well within a standard deviation (SD) of 10%. Since D is proportional to g^2 (Eq. [2.2]) and the gradient noise can be up to 3%, deviations in D up to 6% are the result of gradient noise.

The calculation of D by the Stejskal Tanner (ST) analysis should result in approximately the same values for D as obtained with the propagator analysis, because the same data is used for both calculations. In the measurements reported here the ST analysis gives less accurate results. In the propagator analysis three parameters are fitted to the data, which is one parameter more than in the ST analysis. This third parameter p , the position of the Gaussian-shaped propagator, is not always zero as can be seen in Fig. 2.4c. The ST analysis doesn't have a parameter to correct for this error which of course is also present in the data before the FT and this error results in a higher SD in D , despite the fact that introducing extra fit parameters normally results in higher SD's.

From the results in Fig. 2.3a one can see that the very short T_2 s cause a smearing of the signal intensities in the vertical, phase encoding direction. The shape of the propagator of that volume-element, however, remains the same as the propagator originating from the pixels with a longer T_2 , though its total amplitude is smeared over the neighboring pixels. Tube VI of the first phantom is an example of a sample with volume-elements with very short T_2 s (5.4 ms). The calculation of D by propagator analysis is still rather accurate, albeit with a higher SD. In homogeneous

samples, this poses no problem. Problems can emerge if two neighboring volume-elements both have a short T_2 and a different displacement-behavior: in adjoining pixels of a TSE-image the shape of the propagator is mainly defined by the displacement-behavior of the corresponding volume-element, but in this special case both pixels will experience substantial interference from each other. One might consider lowering the spatial resolution to merge pixels with water with large and small T_2 s together. This could also be a strategy in quantifying the propagators of all pixels in a slice to calculate the total volume flow through the slice (33).

The second phantom shows that besides diffusion also flow information is well preserved in the echo train. An unstable amplitude and phase in the echo train would obscure any displacement correlated phase shift, enforced by the PFGs. The measured maximum flow velocities (4.62 and 4.76 mm/s) are accurate within 2%, to the actual maximum flow velocities in the tube, as driven by the pump (4.72 mm/s).

The areas with water transport in the xylem of a tomato plant emerge after constructing images at different positions on the displacement axis (Fig. 2.5d). These three areas can also be recognized in the T_2 image. In the T_2 image (Fig. 2.5b) the areas show a high T_2 -variance, which may be caused by large differences in T_2 of the water in a xylem vessel and water of supporting or accompanying cells. One pixel can contain more vessels with varying diameters than another, resulting in different T_2 s.

The shape of a propagator from a volume-element in the xylem area is not a summation of a symmetrical Gaussian shaped peak at zero displacement and one step function, broadened by diffusion. At the obtained resolution one pixel represents one or more xylem vessels and/or a part of one or more xylem vessels with accompanying tissue. This can result in a range of propagator shapes that are not known in advance and thus obstructs the possibility to fit the propagator to a model function for quantification. The possibility to obtain propagators with high spatial resolution, acceptable accuracy and a realistic measurement time demands the need for a model-free quantification of the propagator formalism (33).

The pixel size and the amount of time spent on acquisition of the images of the tomato plant were small enough to justifiably entitle the PFG TSE technique as a fast microscopic displacement imaging technique. If averaging is not necessary, and one would use 16 g steps, t_r 1 s, t_f 32 and image size 128×128 , the acquisition of a complete set of propagator images would take 2 min. and 8 sec. At 0.47 T an accurate map of water displacements in a tomato plant stem with a resolution of $117 \times 117 \times 3000 \mu\text{m}$ could be obtained in 17 min. and 8 sec.

Acknowledgements

This research is financially supported by the EU Large Scale Facility WNMRC and the Technology Foundation (STW).

References

1. T. W. J. Scheenen, D. van Dusschoten, P. A. de Jager and H. Van As, in 'Spatially Resolved Magnetic Resonance, Methods, Materials, Medicine, Biology, Rheology, Geology, Ecology, Hardware', (P. Blümli, B. Blümich, R. Botto and E. Fukushima, eds.), Vol. 1, 481-486, Wiley-VCH, Weinheim, New York (1998).
2. P. T. Callaghan, C. D. Eccles and Y. Xia, *J. Phys. E.* **21**, 820-822 (1988).
3. P. T. Callaghan, W. Köckenberger and J. M. Pope, *J. Magn. Reson. Series B* **104**, 183-188 (1994).
4. W. Köckenberger, J. M. Pope, Y. Xia, K. R. Jeffrey, E. Komor and P. T. Callaghan, *Planta* **201**, 53-63 (1997).
5. E. Kuchenbrod, M. Landeck, F. Thürmer, A. Haase and U. Zimmermann, *Bot. Acta* **109**, 184-186 (1996).
6. M. Rokitta, A. Peuke, U. Zimmerman and A. Haase, *ISMRM Book of Abstracts, Sydney*, P1928 (1998).
7. P. Mansfield, *J. Phys. C: Solid State Phys.* **10**, L55 (1977).
8. P. Mansfield and L. Pykett, *J. Magn. Reson.* **29**, 355-373 (1978).
9. J. Hennig, A. Nauwerth and H. Friedburg, *Magn. Reson. Med.* **3**, 823-833 (1986).
10. C. F. Beaulieu, X. Zhou, G. P. Cofer and G. A. Johnson, *Magn. Reson. Med.* **30**, 201-206 (1993).
11. E. O. Stejskal and J. E. Tanner, *J. Chem. Phys.* **42**, 288-292 (1965).
12. D. N. Firmin, R. H. Klipstein, G. L. Hounsfield, M. P. Paley, D. B. Longmore, S. R. Underwood and R. S. Rees, *Magn. Reson. Med.* **12**, 316-327 (1989).
13. D. N. Firmin, G. L. Naylor, P. J. Kilner and D. B. Longmore, *Magn. Reson. Med.* **14**, 230-241 (1990).

14. J. E. M. Snaar and H. Van As, *J. Magn. Reson.* **87**, 132-140 (1990).
15. D. N. Guilfoyle, P. Gibbs, R. J. Ordidge and P. Mansfield, *Magn. Reson. Med.* **18**, 1-8 (1991).
16. Y. Xia and P. T. Callaghan, *Magn. Reson. Med.* **23**, 138-153 (1992).
17. H. Van As and D. Van Dusschoten, *Geoderma* **80**, 389-403 (1997).
18. J. Kärger and W. Heink, *J. Magn. Reson.* **51**, 1-7 (1983).
19. D. van Dusschoten, C. T. Moonen, P. A. de Jager and H. Van As, *Magn. Reson. Med.* **36**, 907-913 (1996).
20. D. van Dusschoten, P. A. de Jager and H. Van As, *J. Magn. Reson. A* **116**, 237-240 (1995).
21. M. D. King, J. Houseman, S. A. Roussel, N. Van Bruggen, S. R. Williams and D. G. Gadian, *Magn. Reson. Med.* **32**, 707-713 (1994).
22. F. Schick, *Magn. Reson. Med.* **38**, 638-644 (1997).
23. H. T. Edzes, D. van Dusschoten and H. Van As, *Magn. Reson. Imag.* **16**, 185-196 (1998).
24. C. J. Rofo, J. Van Noort, P. J. Back and P. T. Callaghan, *J. Magn. Reson.* **108**, 125-136 (1995).
25. P. T. Callaghan, *J. Magn. Reson.* **87**, 304-318 (1990).
26. M. T. Vlaardingerbroek and J. A. den Boer, 'Magnetic Resonance Imaging', pp. 115-166, Springer-Verlag, Berlin (1996).
27. M. L. Glyngell, *Magn. Reson. Imag.* **6**, 415-419 (1988).
28. T. Loenneker, F. Hennel and J. Hennig, *Magn. Reson. Med.* **35**, 870-874 (1996).
29. C.-N. Chen and D. I. Hoult, 'Biomedical Magnetic Resonance Technology', Medical science series, pp. 340, IOP Publishing Ltd, Bristol and New York (1989).
30. W. T. Vetterling, S. A. Teukolsky, W. H. Press and B. P. Flannery, 'Numerical Recipes Example Book (C)', pp. 247, Cambridge University Press, Cambridge (1992).
31. P. A. de Jager, F. J. Vergeldt and H. Van As, 'Book of Abstracts 14th EENC', pp. 211, Bled, Slovenia (1998).
32. C. van der Schoot, 'Determinants of xylem-to-phloem transfer in tomato', thesis Utrecht University, Utrecht (1989).
33. T. W. J. Scheenen, D. van Dusschoten, P. A. de Jager and H. Van As, *ISMRM Book of Abstracts, Philadelphia, P2005* (1999).

3

Microscopic imaging of slow flow and diffusion: a pulsed field gradient stimulated echo sequence combined with turbo spin echo imaging

T.W.J. Scheenen, F.J. Vergeldt, C.W. Windt, P.A. de Jager and H. Van As

In this paper we present a pulse sequence that combines a displacement-encoded stimulated echo with rapid sampling of k-space by means of turbo spin echo imaging. The stimulated echo enables the use of long observation times between the two pulsed field gradients that sample q-space completely. Propagators, constructed with long observation times, could discriminate slowly flowing protons from diffusing protons, as shown in a phantom in which a plug flow with linear velocity of 50 $\mu\text{m/s}$ could clearly be distinguished from stationary water. As a biological application the apparent diffusion constant in longitudinal direction of a transverse image of a maize plant stem had been measured as a function of observation time. Increasing contrast in the apparent diffusion constant image with increasing observation times were caused by differences in plant tissue: although the plant stem did not take up any water, the vascular bundles, concentrated in the outer ring of the stem, could still be discerned because of their longer unrestricted diffusional pathways for water in the longitudinal direction compared to cells in the parenchymal tissue. In the xylem region of a tomato pedicel flowing water could be distinguished from a large amount of stationary water. Linear flow velocities up to 0.67 mm/s were measured with an observation time of 180 ms.

Introduction

Already in 1965 Stejskal and Tanner demonstrated that pulsed magnetic field gradients (PFGs) could be used in nuclear magnetic resonance (NMR) to probe the displacement of protons in a sample (1). Their well-known equation describes the attenuation of the normalized NMR-signal $S(\mathbf{g})$ of diffusing protons as a function of amplitude (\mathbf{g}), spacing (Δ) and duration (δ) of the two PFGs, and as a function of the diffusion constant D of the protons:

$$S(\mathbf{g})/S(0) = \exp(-\gamma^2 \mathbf{g}^2 \delta^2 D(\Delta - \delta/3)) \quad [3.1]$$

where γ is the gyromagnetic ratio of protons. Apart from the NMR-signal amplitude attenuation as a result of diffusion, the phase of the NMR-signal shifts when the protons move in the direction of the PFGs during Δ . Kärger and Heink measured the NMR signal as a function of the intensity m of the PFGs in one direction ($m = \gamma\delta g$, also known as q -space with $q = \gamma\delta g/2\pi$ (2)), and Fourier Transformed the complex NMR-signal as a function of m into the averaged propagator $P(R, \Delta)$ (3). An averaged propagator is a spectrum representing the distribution of spin displacements (R) in the direction of the PFGs within Δ .

Probing displacements with PFGs can be combined with imaging to construct propagators for every pixel in an image (2,4-6). Pixel-propagators can represent different proton pools. In transverse images of plant stems for instance, pixels in the xylem tissue that transports water from roots to shoot and leaves can contain flowing water in a xylem vessel surrounded by stationary water outside the vessel (6,7). The pixel-propagator will show stationary water as a symmetrical part of the displacement distribution centered at zero displacement and flowing water as a part of the displacement distribution with a net displacement (cf. Fig. 3.1c). Recently a method has been presented to quantify the flowing part of the propagator of every pixel in an NMR-image without assuming any model for the flow profile of the flowing water (7), in contrast to fitting a model function to the NMR-signal modulation by a number of q -steps, assuming the occurrence of one complete laminar flow profile in one pixel (8-10).

With both quantification methods problems arise when one wants to study slow flow: one needs long observation times (Δ) to distinguish between displacements originating from slow flow and displacements originating from free diffusion. This will be evident from the following discussion. The root mean square (rms) displacement σ due to diffusion, observed by NMR, is proportional to the square root of the corrected observation time $\Delta - \delta/3$:

$$\sigma = \sqrt{2D(\Delta - \delta/3)} \quad [3.2],$$

whereas the mean displacement \bar{r} of flowing protons is proportional to Δ itself:

$$\bar{r} = \bar{v}\Delta \quad [3.3],$$

in which \bar{v} is the mean flow velocity of the flowing protons. Suppose one wants to distinguish water, flowing with a laminar flow profile at a mean velocity of $200 \mu\text{m/s}$, from stationary water at 20°C (D of free water at 20°C is $2.20 \times 10^{-9} \text{ m}^2/\text{s}$, no exchange between flowing and stationary water, volume fraction flowing water 0.25, $\delta \ll \Delta$). With Δ of 15 ms \bar{r} would be $3.0 \mu\text{m}$, whereas σ would be $8.1 \mu\text{m}$, which makes a distinction between flow and diffusion hardly possible (Fig. 3.1a) on the basis of displacements. Going up to 100 ms observation time \bar{r} and σ would be 20 and $21 \mu\text{m}$ resp. (Fig. 3.1b) and at a value of Δ of 1 second \bar{r} and σ become 200

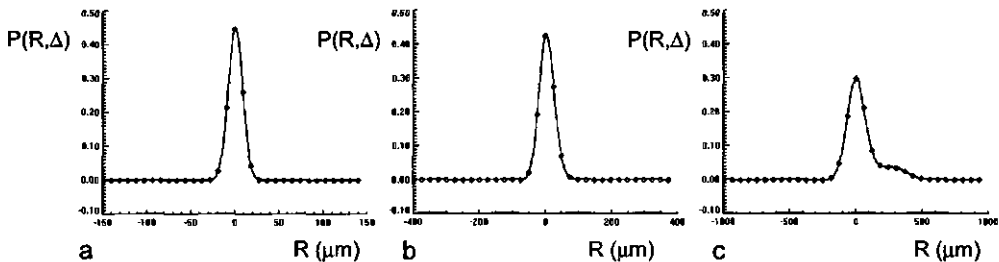


Figure 3.1: Three simulated propagators of 75% stationary water and 25% flowing water. The diffusion constant of the stationary and flowing water is $2.0 \times 10^{-9} \text{ m}^2/\text{s}$, the mean linear flow velocity of the flowing water is $200 \mu\text{m/s}$. No exchange between stationary and flowing water and no radial diffusion over the laminar flow profile has been assumed. Δ -values for (a), (b) and (c) are 15, 100 and 1000 ms resp. The solid lines are the calculated propagators, the marks indicate the sampling of the propagator with a hypothetical experiment with 32 PFG-steps.

and 66 μm . In this last case the flowing part of the propagator becomes clearly visible (Fig. 3.1c). Transversal diffusion of the water is accounted for in these theoretical examples but radial diffusion, perpendicular to the flow direction, is neglected. Incorporating radial diffusion would mean that water molecules move across the laminar, parabolic flow profile, changing the shape of the propagator and decreasing the already small maximum displacement of the flowing water, although \bar{r} would remain unaffected (11).

If long observation times are used in PFG experiments, the time from signal excitation to detection of the first echo will also be long. In this case the need for a stimulated echo (STE) sequence, instead of a spin echo (SE) sequence emerges. Already in 1985 the STE had been used in an imaging sequence (12) and was soon combined with PFGs to measure diffusion (13) and flow (14). Since the T_1 is always (often substantially) longer than the T_2 , it is advantageous or even necessary during long observation times to store the magnetization along the z-axis, where magnetization can evolve according to T_1 : despite the inherent loss of a factor of 2 in signal to noise ratio (SNR) in a STE amplitude, this amplitude can still be larger than a SE amplitude. Recording a complete set of pixelpropagators with only one echo per scan is very time-consuming (4,5). In order to decrease the total acquisition time, we combined the STE with a turbo spin echo (TSE) train. The displacement-encoded STE is modulated in the TSE train to obtain a TSE image for every displacement-encoding step. Since an STE pulse sequence also generates spin echoes (SE of first and second 90° pulses, SE of second and third 90° pulses (15), SE of first and third 90° pulses, and SE of first SE and third 90° pulse) a 180° pulse train behind a STE can also refocus these spin echoes producing unwanted spurious echoes in the echo train resulting in image ghosting. With appropriate phase schemes and spoiler gradients all spurious echoes are suppressed and acceptable TSE images can be obtained. As challenging applications of the STE TSE sequence we measured slow flow in a pedicel of a tomato and we constructed images of the apparent diffusion constant of a transverse slice of a maize plant stem as a function of observation time Δ .

The pulse sequence

Figure 3.2 shows an outline of the Pulsed Field Gradient STimulated Echo Turbo Spin Echo (PFG STE TSE) pulse sequence. Alike its SE variant (6) this sequence uses PFGs to encode for displacement and the Turbo Spin Echo technique, also known as fast SE or RARE (16), to shorten imaging time. The difference is the use of a STE to store magnetization along the z-axis during Δ . As in the SE version we were able to maintain a coherent amplitude and phase throughout the echo train, so amplitude and phase-information, encoded with the PFGs, could be recorded throughout the TSE train.

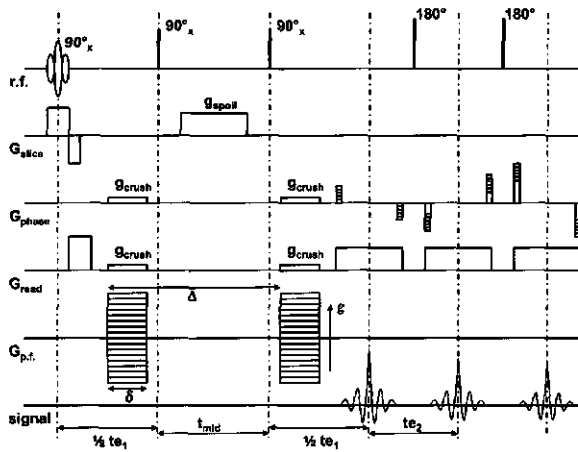


Figure 3.2: An outline of the STimulated Echo Pulsed Field Gradient Turbo Spin Echo pulse sequence. A large spoiling gradient during t_{mid} crushes magnetization in the xy -plane after the first two 90° pulses, whereas the crushers (g_{crush}) and the second PFG within the second $\frac{1}{2} te_1$ period crush the free induction decay of the third 90° pulse.

After the first slice-selective 90°_x pulse the magnetization in the xy -plane is displacement-encoded with the first PFG. All spins in the coil experience the second, hard, 90°_x pulse that stores half the magnetization of those spins, which experienced the first r.f. pulse, along the z -axis for a time t_{mid} . All residual magnetization in the xy -plane (FID of hard pulse) is crushed with the spoiling gradient g_{spoil} . After the third, hard, 90°_x pulse that will induce the STE, displacement encoding is completed with the second PFG. The FID of the third 90°_x pulse is crushed with the crusher pairs in the phase encode and readout direction

and with the second PFG. All gradient pulses in the sequence are ramped, in calculating the effective duration δ of the stepped PFGs (amplitudes from $-g_{\max}$ to zero to $+g_{\max-1}$), one ramp of 100 μs is included. Possible extra signal attenuation due to diffusion between read-out gradients or crushers and differences in T_1 and T_2 in the sample will not vary as a function of PFGs, so the shape of the constructed propagators will only be determined by displacements of the spins involved. The TSE train after the STE phase-encodes every echo between the hard 180° pulses individually, unwrapping the phase encode gradient after every echo. Since the magnetization in the xy -plane is encoded for displacement with the PFGs, the phase of the signal can have any value between minus and plus π , depending on $\gamma\delta g$ and the displacement of the observed spins within the labeling time. Alsop (17) described the problems of refocusing prepared magnetization in a multiple spin echo train and pointed out that it is crucial to either use pulses in the pulse train with flip angles as close to 180 degrees as possible or to modify the TSE part of the sequence in gradient and r.f. pulse amplitudes to prevent rapid signal amplitude decay and oscillations. Edzes et al (18) reported accuracy of observed T_2 values in images of plant tissues (magnetization preparation with phase encode gradient) within 3% of its proper values as long as the 180° pulses were accurate within $\pm 5^\circ$. By interactively adjusting the r.f. pulse amplitude, observing the pulse profile in the solenoid r.f. coil we were able to set and keep the refocusing pulses in the center of the coil at their correct value. The TSE part of the sequence, including the MLEV-4 phase scheme of the 180° r.f. pulses and the k -space trajectories of the echoes is described elsewhere, including the signal processing of the data into pixel-propagators for every pixel in an image (6).

Phantom study

To check whether this technique to construct pixel-propagators with long observation times is able to distinguish very slow flow from self-diffusion we measured the propagators of a phantom with stationary and slowly flowing water. Inside a glass tube with doped (0.1 mM MnCl_2) water was another tube through which a capillary, filled with doped water, was pulled upwards with a syringe pump

(model YA-12, Yale Apparatus, Wantagh NY, USA). This created a perfect plug flow with a controlled and well-defined flow velocity ($50.0 \pm 0.2 \mu\text{m/s}$) surrounded by stationary water. The phantom was fixed in a dedicated solenoid r.f. coil ($\sim 19 \text{ mm}$ inner diameter) inside a custom-engineered gradient probe (Doty Scientific Inc., Columbia, South Carolina, USA), controlled with an SMIS console (Surrey Medical Imaging Systems Ltd., Guildford, Surrey, UK). The 0.7 T magnetic field was generated with an electromagnet (Bruker, Karlsruhe, Germany), stabilized by the use of an external ^{19}F lock unit (SMIS).

Figure 3.3a shows an image of the water density of the phantom. This image is constructed by fitting a mono-exponential decay curve to the NMR-signal of every pixel in an echo train to calculate the NMR signal intensity at the moment of excitation (18). From a PFG STE TSE experiment we also constructed the propagator in the direction of the plug flow for every pixel of the image of the phantom. Because displacements of protons in the phantom in the direction of the PFGs are unrestricted, all pixel-propagators (including pixels inside the moving capillary) were subject to a non-linear least-squares fit to a Gaussian function with amplitude A :

$$P(R, \Delta) = A \exp\left(-\frac{(R - \bar{r})^2}{\sigma^2} / 2\right) \quad [3.4]$$

using the Levenberg-Marquardt method (19). Figure 3.3b and c reflect the results of the Gaussian fit: an image of the position of the maximum of the fitted Gaussian (Fig. 3.3b), representing the mean displacement \bar{r} of the water of the corresponding pixel and the diffusion constant D (Fig. 3.3c), calculated from σ by Eq. 3.2. Using Eq. 3.3, \bar{r} can be used to calculate \bar{v} . In Fig. 3.3a two groups of pixels are indicated: 16 pixels in the center of the capillary and 49 pixels in the large tube. The mean values for \bar{v} and D are $51 \pm 8 \mu\text{m/s}$ and $2.6 \pm 0.1 \times 10^{-9} \text{ m}^2/\text{s}$ for the pixels indicated inside the capillary. For the indicated pixels in the large tube \bar{v} and D are $0 \pm 7 \mu\text{m/s}$ and $2.6 \pm 0.1 \times 10^{-9} \text{ m}^2/\text{s}$ respectively (given errors are standard deviations). The linear flow velocity of the water in the capillary ($51 \pm 8 \mu\text{m/s}$) coincides with the velocity with which the capillary was pulled upwards with

the syringe pump ($50.0 \pm 0.2 \mu\text{m/s}$), although the standard deviation of the velocity is large (16%) due to a low signal-to-noise ratio of the experiment. The diffusion constant of the water inside the capillary is equal to that of the water in the tube: the D-values correspond to a sample temperature of 31°C .

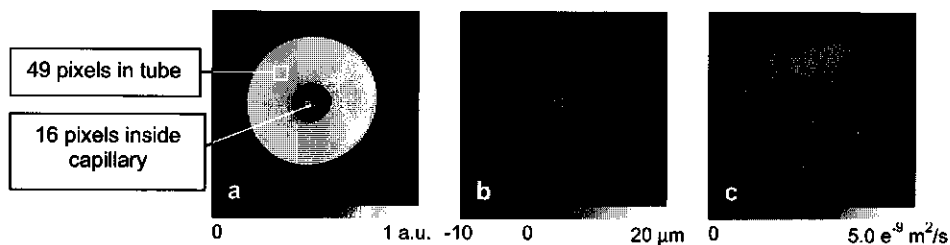


Figure 3.3: Images of a phantom with stationary water and water in a capillary which is pulled through an empty tube at a velocity of $50.0 \mu\text{m/s}$. (a) Calculated image of the initial signal amplitude. (b) The position of the maximum of the Gaussian fit to the propagator of every pixel: the mean displacement \bar{r} of the water. (c) The diffusion constant D , calculated from the characteristic width σ of the Gaussian fit (Eq. 3.2). The grayscale bar in every image represents the indicated quantitative values for the different variables. Since the calculated initial NMR-signal amplitude is in arbitrary units, no values are indicated in image (a). In image (a) is pointed out which pixels are used to calculate the mean values and standard deviations of pixels in the capillary and pixels in the large tube containing stationary water. Mean T_2 inside capillary 143 ± 5 ms, mean T_2 in large tube 143 ± 2 ms. Experimental parameters: 128×128 matrix, field of view 20 mm, slice thickness 3.0 mm, repetition time 2 s. Extra parameters (a): echo time in train 4.8 ms, 64 echoes, measurement time 17 minutes. Extra parameters (b) and (c): 32 PFG steps, Δ 150.1 ms, δ 1.5 ms, PFG_{max} 0.217 T/m, echo time in train 4.4 ms, 32 echoes in TSE train, measurement time 19 minutes.

Maize plant stem

To test the pulse sequence with a biological sample a water-cultured maize plant stem was cut off its roots and put in the instrumental setup. Because of air inlet during cutting the maize plant did not take up any water. The strength of the technique is the possibility to use long displacement encoding times. So to study the longitudinal diffusion constant for every pixel in an image of the stem propagators in the direction along the plant stem were constructed with the following series of Δ -values: 15.1, 30.1, 50.1, 100.1, 175.1, 250.1, and 400.1 ms. Since the diffusional pathways of the water in the cells are restricted by the

boundaries or membranes from the different cell compartments the measured D depends on Δ and is now defined as the Apparent Diffusion Constant (ADC). In Fig. 3.4d to j images of the calculated ADCs as a function of Δ are presented, next to images of the calculated water density (Fig. 3.4a) and the T_2 (Fig. 3.4b) of the maize plant stem. Figure 3.4c is an optical micrograph of a different maize plant stem as an anatomical reference (after (20), page 418). The stem, below the apex, consists of homogeneous tissue of large parenchymal cells and scattered vascular bundles, visible in the water density image as high intensity dots, and in the T_2 image as dots with T_2 -values, smaller than those of parenchymal tissue. The majority of the vascular bundles are concentrated in the outer ring of the stem, clearly visible as a ring with smaller T_2 -values, in comparison with parenchymal tissue. In the NMR images two leaves embrace the stem. A reference capillary with doped water is clearly visible in the calculated water content image, but with a mean T_2 of 21 ± 2 ms (22 pixels in capillary) it is almost invisible in the T_2 image. In

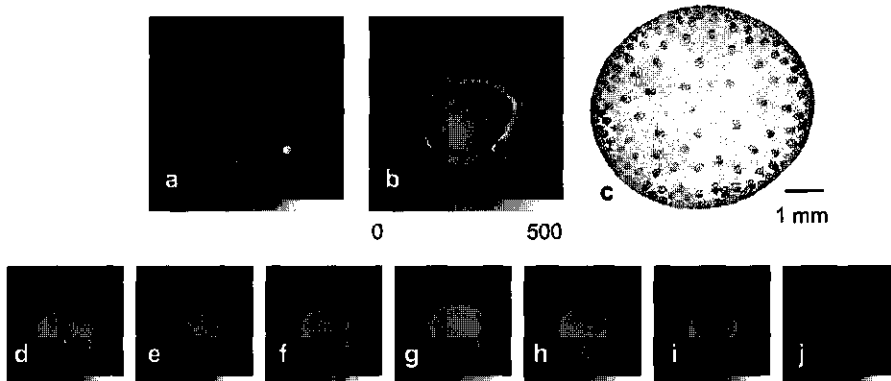


Figure 3.4: Cross-sectional images of the maize plant stem, measured below the apex in the regions where the stem tissue consists of homogenous parenchymal tissue and scattered vascular bundles. (a) Calculated water content image. (b) Calculated T_2 image. (c) Microscopic picture of a transverse coupe of a maize plant stem without stem embracing leaves (after (20), page 418). (d) to (j) Images of the calculated (Eq. 3.2) Apparent Diffusion Constant (in longitudinal direction, along the plant stem) as a function of the following Δ -values: 15.1, 30.1, 50.1, 100.1, 175.1, 250.1, and 400.1 ms. The grayscale bar in image (b) reflects the indicated T_2 -values quantitatively, the bars in images (d) to (j) indicate ADC-values from 0 to $4.0 \times 10^{-9} \text{ m}^2/\text{s}$. Parameters (a)+(b) as in Fig. 3.3a and b. Parameters (d) to (j) as in Fig. 3.3c and d, but for every Δ -value δ , PFG_{max} and measurement time (averaging) have been adjusted to sample q -space correctly with a sufficient signal-to-noise ratio. Measurement time ranges from 34 to 102 minutes for Δ is 15.1 to 400.1 ms respectively.

the series of ADC images the reference capillary can be discerned up to a Δ -value of 100.1 ms, which is about 5 times the T_2 -value. The mean value for the ADC in the reference capillary does not change as a function of Δ although the standard deviation of the ADC increases because of the decreasing signal-to-noise ratio as the time from the first r.f.-pulse to the STE increases (see Table 3.1): because diffusion is unrestricted the ADC will resemble the intrinsic D of the water in the capillary.

Table 3.1: Mean value and standard deviation of the Apparent Diffusion Constant of 22 pixels in the reference capillary next to the maize plant stem as a function of the observation time Δ .

	$\Delta = 15.1 \text{ ms}$	$\Delta = 30.1 \text{ ms}$	$\Delta = 50.1 \text{ ms}$	$\Delta = 100.1 \text{ ms}$
D ($10^{-9} \text{ m}^2/\text{s}$)	2.8 ± 0.2	2.8 ± 0.7	3.0 ± 0.4	3.0 ± 0.5

In the plant stem hardly any contrast in ADCs can be seen at small Δ -values (image d and e), but as Δ increases, some contrast between the center of the stem and the peripheral ring, which is also visible in the T_2 image, becomes clear. Actually, ADC-values of all pixels in the stem decrease, which is even more evident in the histogram in Fig. 3.5, in which the amount of pixels that have a certain ADC are plotted versus the ADC itself for three Δ -values. The ADC-distribution becomes broader with a decreasing mean value: when Δ is small, water molecules will not meet restrictions in their vicinity so the ADC resembles the intrinsic D of the corresponding molecules. When Δ is larger, the chance that a water molecule will be restricted in its diffusional pathway gets larger and the ADC decreases. Tissue with small cells or cell compartments will impose more restrictions to the diffusing water molecules than larger cells or cell compartments, which is an origin of contrast in the ADC. Differences in cell size and cell size compartments in the maize stem are a reason why the ADC-histogram broadens with increasing Δ . The ADC of the pixels in the peripheral ring with mainly vascular bundles and pixels containing scattered vascular bundles in the parenchymal tissue does not decrease as much as the ADC of pixels in the parenchymal tissue itself: vascular bundles have longer unrestricted diffusional pathways in the longitudinal direction than cells in the parenchymal tissue have. T_2 -values of the peripheral ring and the scattered

vascular bundles are smaller than T_2 -values in parenchymal tissue (cf. T_2 image in Fig. 3.4b) but, as mentioned earlier, differences in T_2 of different tissues in the stem are not reflected in the ADCs of the corresponding tissues. Relaxation times have been linked to diffusion constants in a (time-consuming) PFG experiment in which the echo train is not used for fast imaging, but for calculating T_2 -values (21). Combining an echo train for calculating T_2 -values with measuring the propagator for every pixel would also take a lot of acquisition time, but it could link different T_2 -values to different displacements (either due to flow or diffusion) of the water for every pixel.

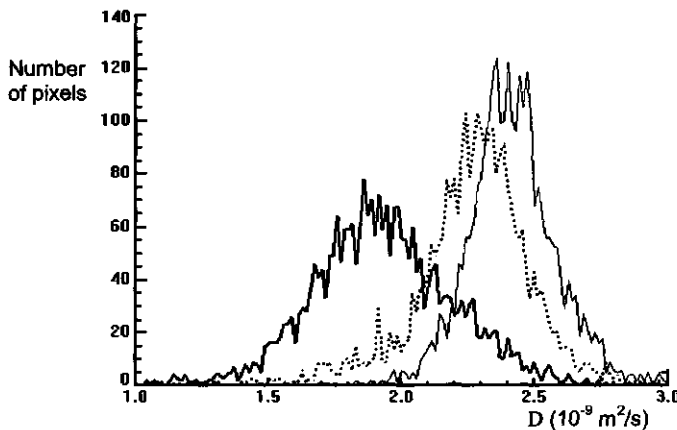


Figure 3.5: The distribution of the ADCs of the images presented in Fig. 3.4 for three different Δ -values: three histograms of the amount of pixels of the image of the maize plant stem belonging to an ADC-value indicated on the x-axis.

Pedicle of a tomato

The final application presented here is the measurement of a small pedicle of a tomato. We cut off a pedicle (21 mm length, 4 mm diameter) from a tomato, attached a silicone tube to the pedicle on the plant stem side and installed it in a test tube with water in the instrumental setup. A small pressure was applied to the pedicle with a water column in the silicone tube of 1.8 m (1.8 m water pressure corresponds to 17.6 kPa) to induce flow through the xylem vessels. The inset in Fig. 3.6 shows two images of the pedicle: the top image is the total integral of the

images from displacements $-121 \mu\text{m}$ to $41 \mu\text{m}$ from the pixel-propagators, whereas the bottom image is the signal intensity at a displacement of $-121 \mu\text{m}$ only (the scale of bottom image is 15 times smaller than the scale of the top image). The contrast in the top image is caused by T_1 : apart from T_1 -weight in the time from the second to the third 90° pulse, tissue with long T_1 -values will be partially saturated with the used repetition time of 1 s. In the top image different tissues in the pedicel can be distinguished: the outer ring with a low intensity is the cortex, the first bright ring is the phloem, the second ring with low intensity is the xylem and in the center the pith is located. The bottom image only has intensity in a few bundles in the xylem: the normalized averaged pixel-propagator from the corresponding pixels is the propagator in Fig. 3.6. Apart from the large amount of stationary water, the shoulder with negative displacements is clear: flowing water in the xylem of this pedicel has linear flow velocities up to $121 \mu\text{m}$ in 180 ms (approx. 0.67 mm/s).

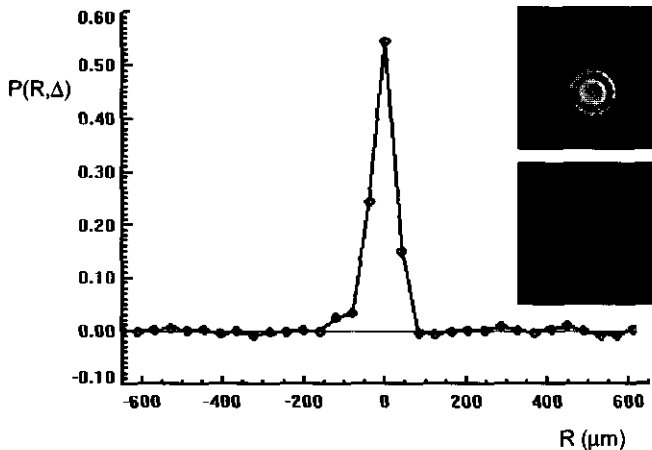


Figure 3.6: The normalized averaged propagator from pixels in the xylem region of a pedicel of a tomato. The shoulder with negative displacements corresponds to water that flows with maximum linear flow velocities of 0.67 mm/s (the sign of the displacements merely indicates the direction of flow). The top image in the inset is the integral image of all displacements between -121 en $+41 \mu\text{m}$: a reference capillary is attached to the silicon tube (the large ring with no intensity around the pedicel) and placed in a test tube with water. The bottom image is the image at a displacement of $-121 \mu\text{m}$, showing bundles with flowing water in the xylem. Experimental parameters: 128×128 matrix, field of view 15.0 mm , slice thickness 4.0 mm , repetition time 1.0 s , 32 echoes in TSE train, echo time in train 4.4 ms , 32 PFG steps, Δ 180 ms , δ 2.0 ms , PFG_{max} 0.144 T/m , 32 echoes, measurement time 17 minutes.

Conclusions

The successful implementation of a stimulated echo in a PFG TSE imaging pulse sequence creates the possibility to construct propagators with observation times of several hundreds of milliseconds between the two displacement-encoding PFGs. These observation times are much longer than those that can generally be reached by PFG SE because T_1 in biological tissues is usually much longer than T_2 , so sufficient signal is left for the stimulated echo and turbo spin echo train. Unwanted spurious echoes from the first three 90° pulses are successfully suppressed before the TSE part of the sequence by spoiler gradients. The use of accurate 180° pulses and an appropriate phase scheme of the 180° pulse train preserve a coherent phase in the echo train so amplitude and phase attenuation of the PFGs is retained throughout the TSE part of the sequence. In this way a fast imaging method is combined with a quantitative measurement of the displacement distribution of water in a pixel within long observation times.

In the phantom study the long Δ -values enable a clear distinction between stationary water and water flowing with a plug flow profile at a velocity as low as $50 \mu\text{m/s}$. In a cut-off maize plant the use of a series of observation times ranging from 15 to 400 ms revealed an increasing contrast in the ADCs of different tissues: mean values of the ADC-distributions decreased and ADC-distribution widths increased with increasing Δ . The averaged propagator of pixels with flowing water in the xylem region of a small tomato pedicel revealed an asymmetric shape: apart from a large amount of stationary water also flowing water with linear flow velocities up to 0.67 mm/s could be discerned with an observation time of 180 ms. Tracking the development of ADCs of different tissues as a function of Δ (e.g. in different PFG directions for diffusion tensor measurements), together with the possibility to observe very slow flow can make the PFG STE TSE pulse sequence a useful tool in displacement studies in different scientific disciplines.

Acknowledgement

This research is supported by the Dutch Technology Foundation STW, applied science division of NWO (project WBI 3493).

References

1. E. O. Stejskal and J. E. Tanner, *J. Chem. Phys.* **42**, 288-292 (1965).
2. P. T. Callaghan, C. D. Eccles and Y. Xia, *J. Phys. E.* **21**, 820-822 (1988).
3. J. Kärger and W. Heink, *J. Magn. Reson.* **51**, 1-7 (1983).
4. P. T. Callaghan, W. Köckenberger and J. M. Pope, *J. Magn. Reson. Series B* **104**, 183-188 (1994).
5. W. Köckenberger, J. M. Pope, Y. Xia, K. R. Jeffrey, E. Komor and P. T. Callaghan, *Planta* **201**, 53-63 (1997).
6. T.W.J. Scheenen, D. van Dusschoten, P.A. de Jager and H. Van As, *J. Magn. Reson.* **142**, 207-215 (2000).
7. T. W. J. Scheenen, D. van Dusschoten, P. A. de Jager and H. Van As, *J. Exp. Bot.* **51**, 1751-1759 (2000).
8. E. Kuchenbrod, M. Landeck, F. Thürmer, A. Haase and U. Zimmermann, *Bot. Acta* **109**, 184-186 (1996).
9. M. Rokitta, U. Zimmermann and A. Haase, *J. Magn. Reson.* **137**, 29-32 (1999a).
10. M. Rokitta, A. D. Peuke, U. Zimmermann and A. Haase, *Protoplasma* **209**, 126-131 (1999b).
11. U. Tallarek, E. Rapp, T. Scheenen, E. Bayer and H. Van As, *Anal. Chem.* **72**, 2292-2301 (2000).
12. J. Frahm, K. D. Merboldt, W. Hänicke and A. Haase, *J. Magn. Reson.* **64**, 81-93 (1985).
13. K. D. Merboldt, W. Hänicke and J. Frahm, *J. Magn. Reson.* **64**, 479-486 (1985).
14. K. D. Merboldt, W. Hänicke and J. Frahm, *J. Magn. Reson.* **67**, 336-341 (1986).
15. P. T. Callaghan, "Principles of Nuclear Magnetic Resonance Microscopy," 76, Clarendon Press, Oxford, UK (1991).
16. J. Hennig, A. Nauwerth and H. Friedburg, *Magn. Reson. Med.* **3**, 823-833 (1986).
17. D. C. Alsop, *Magn. Reson. Med.* **38**, 527-533 (1997).
18. H. T. Edzes, D. van Dusschoten and H. Van As, *Magn. Reson. Imag.* **16**, 185-196 (1998).
19. W. T. Vetterling, S. A. Teukolsky, W. H. Press and B. P. Flannery, "Numerical Recipes Example Book (C)," 247, Cambridge University Press, Cambridge, UK (1992).
20. P. H. Raven, R. F. Evert and S. E. Eichhorn, "Biology of Plants, fourth edition," Worth Publishers, New York, USA (1986).
21. D. van Dusschoten, C. T. Moonen, P. A. de Jager and H. Van As, *Magn. Reson. Med.* **36**, 907-913 (1996).

Addendum to Chapter 3

The combination of a pulsed field gradient spin echo sequence with multiple spin echo imaging

For micro-imaging of displacements of water in a packed capillary chromatography column we implemented a pulse sequence which combines motion-encoding pulsed field gradients with a multiple spin-echo imaging module (21). It is the unique feature of this approach that not only an amplitude attenuation but also phase-information is maintained over the whole echo-train at each value of q . Figure 3.7 illustrates the information of the multi-echo PFG-NMR experiment after Fourier transformation (FT) of $S(\mathbf{k}, q)$ with respect to \mathbf{k} (see also Eq. 2.9). Horizontally shown in Fig. 3.7a is the modulation of the real part of the NMR images (after FT with respect to \mathbf{k}) as a function of q , whereas the signals decay in the echo-train is displayed vertically. After FT with respect to q (zero-filling of the data is possible here) we obtain pixelpropagators $P_{av}(\mathbf{R}, \Delta)$ for every echo in Fig. 3.7b. The signals decay in the echo-train is usually characterized by T_2 , but with a used nominal in-plane resolution of $40 \times 40 \mu\text{m}$ the imaging gradients become large enough that this decay is also affected by the dispersive motion of the fluid molecules (18). In principle, such a multi-echo PFG-NMR imaging experiment can relate an initial signal amplitude and a characteristic decay time to any pixel and any displacement \mathbf{R} . We used an additional multi-echo imaging experiment (i.e., $q = 0$) with increased signal-to-noise ratio (40 averages and 20 echoes) to examine the characteristic decay time for each pixel in the column. No systematic differences in decay times could be retrieved and we used the mean value (32 ms) to filter signals in the echo-train for each pixel in order to add filtered signals when needed and increase the signal-to-noise ratio of the final pixel-propagators.

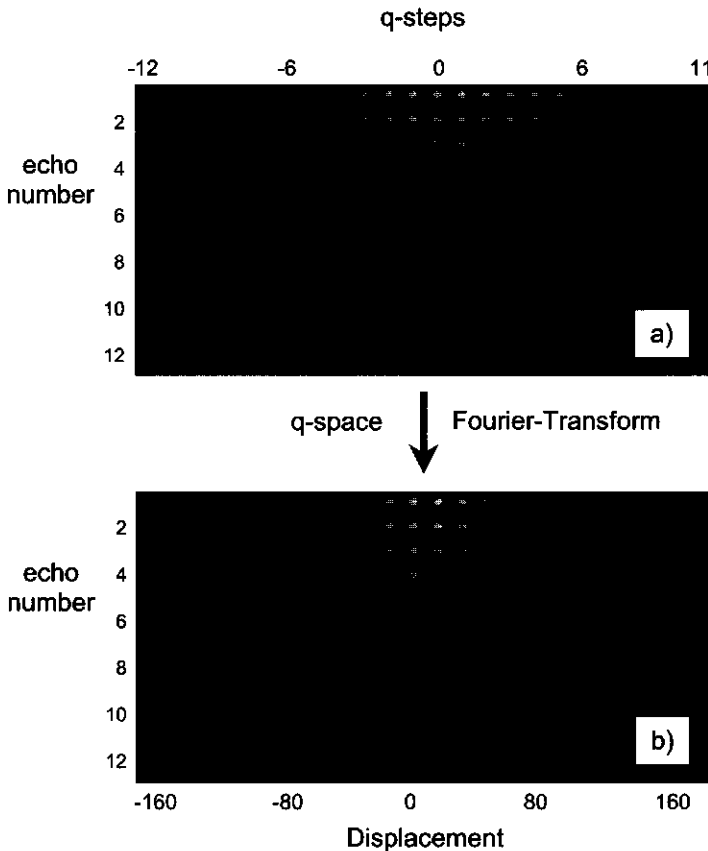


Figure 3.7: Multi-echo PFG-NMR imaging experiment after Fourier transformation of the data with respect to k . a) 24 by 12 images of the packed capillary (24 q -steps and 12 echoes) demonstrating the modulation of the complex signals real part depending on q (horizontally) and echo number (vertically). b) 24 images after zero-filling in q -space from 24 to 72 steps and Fourier transformation with respect to q . The horizontal axis represents displacement space.

Experimental parameters: $20 \times 20 \times 12 \times 24$ matrix, 0.8 mm field of view, slice thickness: 6.0 mm, 0.8 s repetition time, g_{\max} : 0.31 T/m, $\delta = 2.3$ ms, $\Delta = 17.5$ ms and echo time in train: 5.2 ms.

With this experiment we tried to spatially resolve flow heterogeneities in the capillary column with an in-plane resolution of $40 \mu\text{m}$. The slice thickness was set to 6 mm because we expect the effects to be systematic along the column axis and consequently do not require a high spatial resolution in this third dimension. Thus, a reasonable signal-to-noise ratio and a sufficiently high resolution over the column cross-section (compared to the particle diameter, $d_p = 50 \mu\text{m}$) could be achieved.

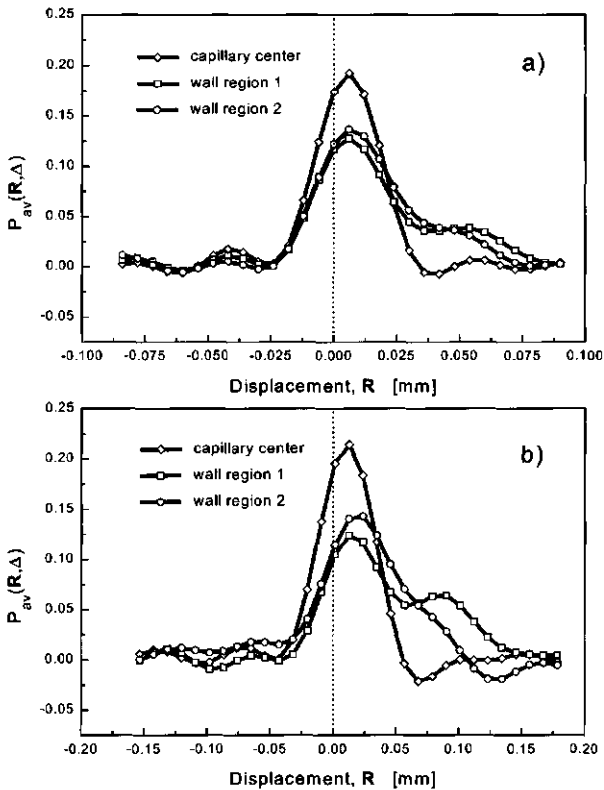


Figure 3.8: Added propagators comparing the fluid dynamics in wall and center positions of the capillary, a) $\Delta = 17.5$ ms and b) $\Delta = 35$ ms. Displacement distributions have been normalized by their surface area. Mobile phase: 10^{-3} M sodium tetraborate buffer (pH 9.13).

The propagators from four added pixels representative for wall and center positions in the capillary are shown in Fig. 3.8. Data were collected from opposite edges of the capillary cross-section (wall region 1 and 2), and were zero-filled before FT with respect to q and normalized. The distributions show pronounced shoulders or even separate local maxima for fluid molecules in pixels closer to the column wall than pixels in the center of the capillary and the effects scale with observation time, but a lateral exchange of molecules between velocity extremes is also promoted.

4

Quantification of water transport in plants with NMR imaging.

T.W.J. Scheenen, D. van Dusschoten, P.A. de Jager and H. Van As

A new nuclear magnetic resonance imaging (NMRI) method is described to calculate the characteristics of water transport in plant stems. Here, dynamic NMRI is used as a non-invasive technique to record the distribution of displacements of protons for each pixel in the NMR image. Using the NMR-signal of the stationary water in a reference tube for calibration, the following characteristics can be calculated per pixel without advance knowledge of the flow-profile in that pixel: the amount of stationary water, the amount of flowing water, the cross-sectional area of flow, the average linear flow velocity of the flowing water and the volume flow. The accuracy of the method is demonstrated with a stem segment of a Chrysanthemum flower by comparing the volume-flow, measured with NMR, with the actual volumetric uptake, measured with a balance. NMR measurements corresponded to the balance uptake measurements with a rms error of 0.11 mg/s in a range of 0 to 1.8 mg/s. Local changes in flow characteristics of individual voxels of a sample (e.g. intact plant) can be studied as a function of time and of any conceivable changes the sample experiences on a time-scale, longer than the measurement time of a complete set of pixel-propagators (17 min.).

Introduction

One of the key-tools in the continuing debate about mechanisms of long-distance water transport in plants (1-5) is the ability to measure the water transport directly, non-invasively and spatially resolved. To validate recent theories (6, 7) in fundamental issues about the occurrence and refilling of embolized xylem vessels one needs a technique to measure the volume flow, the linear flow velocity and the cross-sectional area of flow in the xylem vessels of an intact plant.

The heat pulse velocity technique (8) and derived techniques, that use heat as a tracer, can be useful in measuring water uptake by trees or plants non-destructively, although heater probes and temperature sensors have to be inserted into the stem. Moreover, no information about the exact positions of flow within the measured stem can be obtained and heterogeneities in the stem tissues cause problems in calibrating the technique (9). Other techniques to assess sap flow in stems include the injection of radioactive tracers into the xylem and the use of porometers to measure leaf transpiration of a representative part of a plant to estimate the total transpiration, resembling total water uptake.

In the last ten years or so, Nuclear Magnetic Resonance (NMR) has proven to be a useful non-invasive technique to measure flow in plants *in vivo* (10-14). One of the NMR imaging techniques - dynamic NMR microscopy (15) - provides direct information on the distribution of all spin displacements within a pixel of an NMR image using predefined labeling times. To accomplish this, dynamic NMR microscopy combines standard imaging with Pulsed Field Gradient (PFG) NMR. Since flow in xylem vessels can change rapidly, methods to visualize flow and measure changes in flow should be faster than the time it takes for these changes to occur. Dynamic NMR experiments normally are time-consuming (15, 16), but recently, new methods have been developed to decrease the measurement time drastically (14, 17, 18).

The measurement time can be decreased by not recording the complete distribution of displacements of spins (the so-called propagator) for every pixel (17, 19). This approach can be used if the displacement distribution of the spins is known in

advance. If so, the need to record the complete propagator disappears, less flow encoding steps are required and the NMR-signal as a function of the flow encoding steps can be fitted to a model function. However, in plant tissue, and probably in any non-artificial sample, the distribution of displacements of spins in a pixel is unknown and can vary with time.

The reason why in (plant) tissue the use of a model function is essentially wrong is threefold. Firstly, it is not possible to choose the pixel size (e.g. $100 \times 100 \times 2500 \mu\text{m}$) and position of an image in such a way that one pixel always contains no more than one complete vessel. Vessels differ in size and are often grouped, so pixels will generally contain more than one vessel (at low spatial resolution) or only part of one vessel (at high spatial resolution or with large vessels). Secondly, it is assumed that on the timescale of flow encoding (Δ) spins do not move perpendicular to the flow direction. Diffusion of spins from one position on the flow profile to the other within the flow encoding time changes the shape of the displacement distribution drastically (20). The third reason is that vessels in biological tissues are often not perfectly circular and have a rough surface, which can influence the displacement distribution.

In conclusion, the best way to quantify flow is to avoid any model for flow within a pixel. This can be done by recording the propagator, which is the distribution of displacements within a certain flow encoding time, and by extracting flow-characterizing parameters from these propagators that are essentially independent of any flow-profile. The flow-sensitive PFG Turbo Spin Echo (TSE) technique (21) produces these propagators for every pixel in an image in a physiologically relevant measurement time. Here a method is presented to extract several important variables from the pixel-propagators without reverting to any model or assumption for the flow profile. These variables include the volume flow, the linear flow velocity and the cross-sectional area of the flowing fluid of the pixel. Using a reference tube to calibrate the NMR-signal we can calculate absolute values for the volume flow and the cross-sectional area of the flowing fluid, rather than normalizing the volume flow to the maximum volume flow observed (22). In principle, the method can be used for any set of pixel-propagators of any sample. In this work stem segments of *Chrysanthemum* (*Dendranthema x grandiflorum* Tzvelev cv. Cassa) were used

because the volume flow through the stem segment could easily be controlled, and did not depend on environmental conditions as relative humidity, light intensity and temperature.

Theory

Principles of NMR imaging

^1H -nuclei possess a quantum mechanical property called spin, which, when placed in a magnetic field, precesses around the magnetic field vector at a frequency (the Larmor frequency) that depends on the magnetic field strength (3). The small, thermally equilibrated difference between spins precessing along the magnetic field vector (spin up) and spins precessing opposite to the magnetic field vector (spin down) causes a net magnetization vector of the spins along the magnetic field axis. This net magnetization vector can be manipulated by disturbing the equilibrium of the nuclear spin system with radio frequency (rf) pulses, produced with an rf coil around the protons in the magnetic field. Any magnetization in the plane perpendicular to the magnetic field after an rf pulse induces an rf signal in the coil around the sample. The magnetization vector will return to its initial size and direction with two typical time constants: the spin-spin relaxation time (T_2) characterizes the loss of magnetization in the plane perpendicular to the magnetic field (which is the loss of the NMR-signal), whereas the return of magnetization along the magnetic field is characterized by the spin-lattice relaxation time (T_1). Since the NMR-signal represents the magnetization in the plane perpendicular to the magnetic field axis, it is also a vector with an amplitude and phase, precessing at the Larmor frequency. Linear magnetic field gradients, superimposed on the static magnetic field, generate a position-dependent Larmor frequency: different frequencies of the NMR-signal can be processed (by a Fourier transform) into an NMR image, which is a map of the proton (usually water) density or an NMR-specific parameter for every position in a sample.

Probing movement of protons

The NMR-signal for every position in a sample can be made sensitive for the displacement of the protons in a certain direction by use of two pulsed magnetic

field gradients (PFGs) with spacing Δ . Here we explain the influence of two kinds of displacements - diffusion and laminar flow - of spins on the NMR-signal and the shape of the distribution of displacements (propagator) deduced from the signal as a function of PFG amplitude. The theory concerning the propagator formalism (15) and the fast acquisition of complete pixel-propagators (21) has already been extensively described elsewhere.

If an ensemble of molecules exhibits self-diffusion due to the Brownian motion, the PFGs will attenuate the amplitude of the NMR-signal of the protons of the molecules, while the phase of the NMR-signal will remain unaffected. A Fourier transform of the signal into $P(R, \Delta)$, the probability distribution of displacements R in the direction of the PFGs within the labeling time Δ , results in a Gaussian shape (Fig. 4.1) as described by:

$$P(R, \Delta) = A \exp\left(-\frac{(R-p)^2}{\sigma^2}\right) \quad [4.1]$$

with A as amplitude and p as mean displacement ($p = 0$ for stationary water) of the water protons. The characteristic width of the Gaussian σ can be used to calculate the self-diffusion coefficient D of the molecules:

$$D = \frac{\sigma^2}{2(\Delta - \delta/3)} \quad [4.2]$$

where δ is the duration of each of the two PFGs.

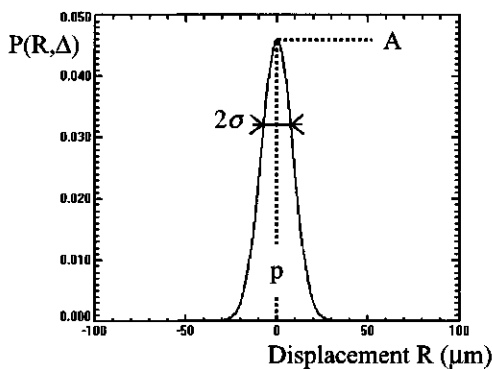


Figure 4.1: Normalized theoretical displacement distribution of stationary water. The propagator of stationary, self-diffusing water is a Gaussian peak with position $p = 0$, characterizing width σ and amplitude A . The displacement axis is sampled with 200 data points.

As an example of displacements of molecules due to flow, let us observe slowly flowing water inside a cylinder. The water in the cylinder can be divided into thin circular layers that glide past one another. The water adjacent to the wall of the cylinder is essentially stationary. As one moves away from the wall to the center of the cylinder the flow velocity increases to a maximum in the center. If viscous drag forces dominate the inertial forces of the fluid the flow profile through the cylinder has a parabolic shape and is called a laminar flow profile. In the hypothetical case that the fluid does not exhibit a Brownian motion only the phase of the NMR-signal of these circular layers is shifted without modulation of the signal amplitude as a function of PFG amplitude. Fig. 4.2a depicts a laminar flow profile through a cylinder and its propagator in the direction of flow, in absence of self-diffusion. The propagator consists of a distribution of displacements R from zero to maximum displacement R_{max} within Δ and is a boxcar function:

$$\begin{aligned}
 P(R, \Delta) &= C \quad \text{for } 0 \leq R \leq R_{max} \\
 P(R, \Delta) &= 0 \quad \text{for } R < 0 \text{ and } R > R_{max}
 \end{aligned}
 \tag{4.3}$$

where C is a constant and the integral $\int_{-\infty}^{\infty} P(R, \Delta) = 1$. Different layers in the cylinder coincide with different parts of the propagator, as is shown by the arrows in Fig. 4.2a. If the circular layers in the cylinder are thought to be infinitesimally thin, the corresponding part in the propagator will be a spike at the correct displacement.

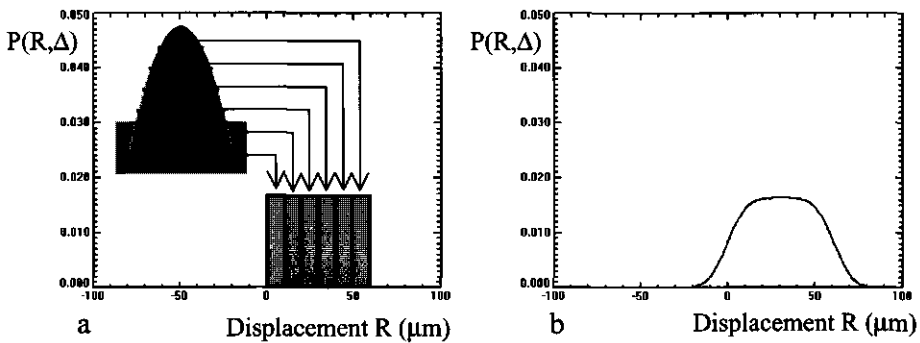


Figure 4.2: Normalized displacement distributions of flowing water sampled with 200 points. a. The hypothetical propagator of a laminar flow profile in absence of self-diffusion. b. As a with self-diffusion present.

Usually, the fluid in the cylinder also exhibits self-diffusion, which combines the phase-shift of the NMR-signal due to flow, with the amplitude attenuation of the signal due to diffusion. The shape of the corresponding propagator changes: every thin circular layer in the cylinder now has a Gaussian shape instead of a spike (cf. Fig. 4.1). All these layers together form a propagator as shown in Fig. 4.2b: the boxcar function is broadened by a Gaussian. If an observed ensemble of spins contains more than one cylinder with flowing water, the propagator will be the sum of several boxcar functions, broadened by diffusion. If only a part of one cylinder with flowing water is observed, the propagator will be only a part of this broadened boxcar function.

Materials and Methods

NMR Image analysis

The PFG-TSE (turbo spin echo) pulse sequence (Fig. 4.3) has been described elsewhere (21). The amplitude and phase modulation of the NMR signal as a function of the displacement encoding steps can be Fourier Transformed to obtain the propagator. Generally, the pixel-propagator within a slice through a plant stem has a Gaussian shape, since it contains only stationary, diffusing water (cf. Fig. 4.1). However, some of the pixels in the stem are in regions where active xylem or phloem vessels are present, so the corresponding propagators will show displacements originating from flowing sap.

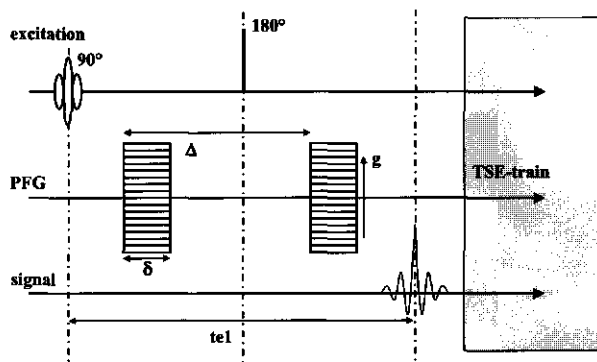


Figure 4.3: Pulsed field gradient turbo spin echo pulse sequence. The two large pulsed field gradients in the flow direction with duration δ and spacing Δ are stepped to acquire flow information.

Propagators representing both stationary and flowing water can be analyzed in the following way. The half, which doesn't display flow, is fitted to a half-Gaussian. Subsequently the complete Gaussian (including the other half) is subtracted from the propagator. The remaining part of the propagator $P_F(R, \Delta)$ represents the flowing water. This propagator is calibrated into $P_C(R, \Delta)$ by dividing it with the integral I_{ref} of a propagator of a pixel in a reference tube that is filled with doped water:

$$P_C(R, \Delta) = \frac{P_F(R, \Delta)}{I_{ref}} \quad [4.4].$$

Relating the calibrated propagator $P_C(R, \Delta)$ to the experimentally known surface A_{ref} of one pixel the cross sectional area of flow A of the flowing water can be calculated for every pixel:

$$A = \sum_{R=0}^{R=R_{max}} P_C(R, \Delta) \cdot A_{ref} \quad [4.5].$$

The first moment of the calibrated propagator represents the volume flow Q of the corresponding pixel and can be calculated by adding the propagator intensities multiplied by the displacement values and relating it to A_{ref} and Δ :

$$Q = \sum_{R=0}^{R=R_{max}} (P_C(R, \Delta) \cdot R) \cdot \frac{A_{ref}}{\Delta} \quad [4.6].$$

The average linear flow velocity \bar{v} is the volume flow divided by the cross-sectional area of flow (strictly the calibration is not necessary for \bar{v}):

$$\bar{v} = \frac{Q}{A} = \frac{\sum_{R=0}^{R=R_{max}} (P_C(R, \Delta) \cdot R)}{\sum_{R=0}^{R=R_{max}} P_C(R, \Delta) \cdot \Delta} \quad [4.7].$$

A few assumptions are made here: within one pixel water does not flow in two directions and the loss of NMR-signal within the time between excitation and detection of the first echo (te_1 , Fig. 4.3) is comparable for the reference tube and the water in the xylem.

The spectrometer

The NMR spectrometer consists of an SMIS console (SMIS Ltd., Guildford, Surrey, UK), operating at 30.7 MHz, an electromagnet with a 10 cm air gap (Bruker, Karlsruhe, Germany) generating the magnetic field of 0.72 T and an external ^{19}F lock unit (SMIS) stabilizing the magnetic field. The magnet is equipped with a

custom-engineered gradient probe (Doty Scientific Inc., Columbia, South Carolina, USA) with a 45 mm (i.d.) cylindrical central bore, accessible from both ends. The stem segments of cut flowers were measured in a custom made vase (Fig. 4.4) that can be inserted in the gradient probe. A solenoid radio frequency (r.f.) coil (12 mm inner diameter), wrapped around the shallow part of the vase, transmits the NMR-pulses and receives the signal.

Plant material

Chrysanthemum (*Dendranthema x grandiflorum* Tzvelev cv. Cassa) plants were grown in a greenhouse at Wageningen University, in plastic pots (14 cm diameter) with a commercial potting soil. The average temperature in the greenhouse was 18° C. The plant had a photoperiod of 16 hours until the plant had formed 15-17 leaves longer than 0.5 cm (3-4 weeks), followed by an eight hours photoperiod until harvest. The photoperiods were lengthened by high-pressure sodium lamps or shortened by black screens when necessary. Flowering stems at commercial maturity and stem segments were cut off underwater with razor blades to ensure that no air entered the xylem vessels of the stem.

Setup to control water uptake of stem segments

Van Ieperen et al. (24) described a method to control the water uptake of stem segments. This method is used here, since it enables a very precise control of the water flow level through a stem segment, it measures water uptake directly (not by way of transpiration) and it is straightforward to implement. The method will briefly be summarized here. The water level in the vase is controlled with a communicating vessel on a precision balance: the uptake of water by a cut flower or stem segment is measured with the balance (LC3201D, Sartorius AG, Göttingen, Germany) by sampling the weight decrease every 20 seconds. The uptake of water of a stem segment is controlled with underpressure: the top of the stem segment is connected with water-filled silica tubing to a vessel of which the underpressure is controlled with a pump (Fig. 4.4). The pump (505DI Watson-Marlow Limited, Falmouth, UK), the vacuum sensor (DVR5, Vacuubrand, Gmbh & Co, Wertheim, Germany) and the balance were connected to a computer to automate underpressure control and uptake measurements.

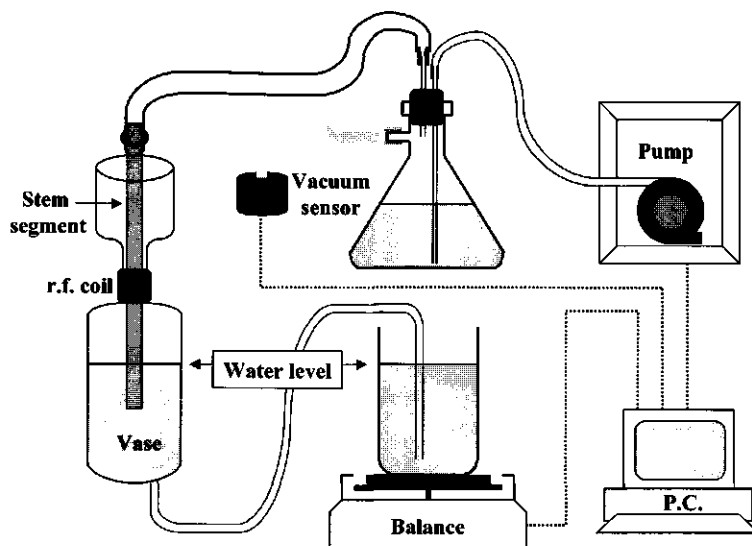


Figure 4.4: Draft of the set-up to control the water uptake of stem segments (after Van Ieperen *et al.*, 2000).

Results

The stem segment of a Chrysanthemum flower in the set-up was 25 cm long, measured at 40 cm from the roots, 10 cm above the cut surface. The NMR measurements show a distribution of displacements of all protons for every pixel in an image (Fig. 4.5). Fig. 4.5a displays a transverse image of the stem segment at $g=0$: this is a standard TSE image that displays the proton density for every pixel (21). The striking feature of the image is that it displays only a single, relatively thin, ring. As a reference, Fig. 4.5b is a photograph of a transversal section through a Chrysanthemum stem: the spongy tissue with large dead parenchymatic cells in the middle of the stem hardly contains any water, so it does not give a detectable NMR-signal. The outer ring of the stem contains all functional tissue, including xylem, cambium, phloem, supporting tissues and epidermis. Pixels in the xylem region of the stem segment can display stationary and flowing water. The propagator of a particular pixel ($100 \times 100 \times 2500 \mu\text{m}$) in that region (Fig. 4.5c) reveals a peak, centered at a displacement of $0 \mu\text{m}$, representing stationary water, with a large asymmetrical shoulder with positive displacements, representing flowing water. The

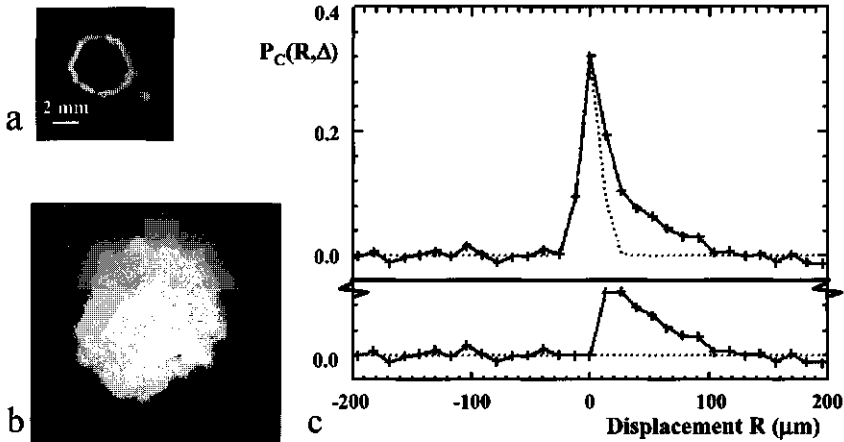


Figure 4.5: a. A TSE image of a Chrysanthemum stem segment, perpendicular to the stem axis. b. A photograph of a transverse section through a Chrysanthemum stem. c. The calibrated propagator of a pixel in the xylem region of the stem (solid line) with the Gaussian fit to the left half of the propagator (dotted line). The bottom panel shows the difference between the original calibrated propagator and the fit on the same scale. The crosses in the solid lines indicate the individual data points. Parameters: resolution $100 \times 100 \times 2500 \mu\text{m}$, t_{e1} 25.0 ms, 32 PFG steps, Δ 19.4 ms, δ 2.5 ms, PFG_{max} 0.36 T/m, repetition time 1 s, number of averages 4, total measurement time 17 min.

propagator was calibrated with the averaged intensity of nine pixels in the reference tube (Eq. 4.4). The dotted line in Fig. 4.5c is the result of a fit to the left half of the calibrated propagator using a Gaussian function. After subtraction of this Gaussian from the propagator the asymmetrical flowing part of the propagator remains. This part is plotted in Fig. 4.5c below the complete propagator. The integral of the flowing part of the calibrated propagator represents the fraction of the corresponding pixel through which water flows, relative to a pixel in the reference tube. This fraction can be recalculated into the cross sectional area of flow within the pixel in mm^2 (Eq. 4.5), knowing the surface A_{ref} of a pixel inside the reference tube, and assuming that the anatomy of a stem segment does not change along the axis of the stem within the slice thickness ($2500 \mu\text{m}$). Apart from the cross sectional area of flow the volume flow and linear flow velocity can be calculated for every pixel with equations 4.6 and 4.7. Knowing these flow characteristics for each pixel one can construct images with the characteristics: total amount of water, total amount of stationary water, cross sectional area of flow, linear flow velocity and volume flow (Fig. 4.6a to e respectively). Fig. 4.6f indicates the regions of flow (cf. Fig. 4.6e) superimposed on the image of the water content of the stem segment (cf. Fig. 4.6a).

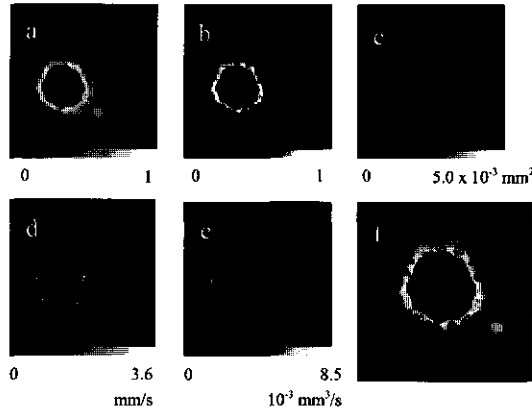


Figure 4.6: Images of the calculated flow characteristics of the stem segment. a to e, respectively water content, amount of stationary water, cross sectional area of flow, linear flow velocity and volume flow. The grayscale bar relates intensities to quantitative values. Water content and the amount of stationary water are expressed as fractions, relative to the mean water content of a pixel in the reference tube (= 1 unit) and can easily be recalculated into a volume or a surface. f. The areas that show flow superimposed on an enlarged image of the water content (cf. a.).

The total volume flow through the stem segment was monitored with the precision balance and could easily be changed by varying the underpressure of the vessel that was connected to the top of the stem segment. Stepwise decreasing the pressure differences over the stem segment in a range of 47 to 0 kPa resulted in uptake values from 1.8 to 0 mg/s: a physiologically sensible range for Chrysanthemum (Fig. 4.7). Small negative uptake values were the result of a small overpressure of remaining water in the silica tubing on top of the stem segment, pushing water backwards through the xylem. After about two hours the uptake, which was constant in the first three pressure steps, decreased with (maximum) seven percent during one pressure step: the hydraulic resistance of the stem segment increased slowly with time. This effect is even more evident when pressure steps 1 and 5 or 2 and 6 are compared: at the same pressure difference the uptake in the measurements later in time has decreased. However, the increase in hydraulic resistance of the stem segment is of little importance for a comparison of two ways to measure water transport in a single stem and the measurement time (17 min.) for the dynamic NMR imaging experiment is short enough to have a constant uptake during one measurement.

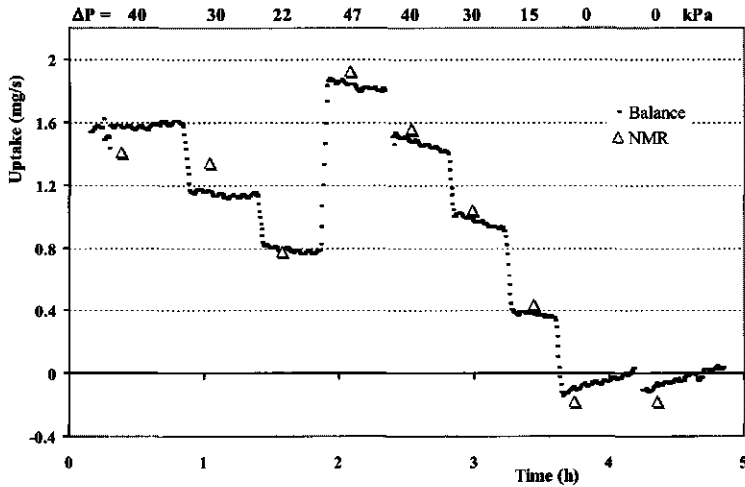


Figure 4.7: A comparison of the actual water uptake of a stem segment, measured with a precision balance, and the total uptake measured with NMR, by adding the volume flow of every pixel that shows flow. The marks indicating the uptake, measured with the balance, are running averages of 10 points (200 s). The row of values for ΔP indicates the pressure difference over the stem segment for every pressure step in kPa.

The NMR measurements are represented by triangular markers in Fig. 4.7 and were calculated by adding all pixels of the NMR image of the volume flow that had intensities larger than a manually set threshold value ($\sim 2/3$ of peak noise level) with at least one neighboring pixel that also exceeded the threshold value. Except for the first two pressure steps, the NMR flow values correspond within an error of 0.10 mg/s with the actual flow that was measured with the balance. In the first two steps, the difference is 0.16 and 0.20 mg/s respectively. The overall rms error of all points is 0.11 mg/s. For negative uptake values, the positive halves of the propagators were used for the Gaussian fit and the negative halves were used to calculate the volume flow.

Discussion and Conclusions

A pixel-propagator from the xylem region of a *Chrysanthemum* stem is not simply the sum of a Gaussian peak at zero displacement and a broadened boxcar function. This becomes especially clear when the Gaussian fit is subtracted from the

propagator. Due to the large pixel size (100 x 100 x 2500 μm) a propagator from a pixel in the xylem region will always represent multiple xylem vessels and accompanying cells, since xylem vessels in *Dendranthema x grandiflorum* Tzvelev cv. Cassa have diameters in a range from 10 to 40 μm (25). Therefore, the shape of a single pixel propagator is not known a priori and the use of a model function for the modulated NMR signal to calculate flow data is clearly not correct. However, one can accurately calculate the volume flow, as Tsai et al described (26), by way of the first moment of the propagator by differentiating the modulated NMR-signal at $g=0$ (first moment theorem of Fourier transforms (27)). If not just the volume flow, but also the linear flow velocity and the cross-sectional area of flow are of interest the only accurate solution, i.e. not assuming any flow-profile, as far as we know is the method described above (see Materials and Methods). The fit of the stationary water to the half-Gaussian function is in principle only validated if the stationary water can diffuse without restrictions. This means that on the time-scale (Δ) of labeling the bulk of the molecules should not reach any walls or membranes. In practice, the bulk of the water-molecules resides in vacuoles and moves 9 μm (rms value σ from Eq. 4.2) with the instrumental settings we used ($\Delta\delta/3 = 18.6$ ms) and $D = 2.0 \times 10^{-9}$ m^2/s (free water at 20°C). Even if displacements of 9 μm were already restricted by the membrane of the vacuoles of the cells, surrounding the vessels, the effect on the shape of the stationary water part of the propagator would be small: the Gaussian fit would still remove the stationary water part quite effectively.

One other issue to be mentioned here is the fact that flowing water has intensity at zero displacement in the propagator (cf. Fig. 4.2). This intensity originates from water near the walls of the vessel or tube in which it is flowing. In the presented method no intensity is left at zero displacement after subtraction of the Gaussian fit from the propagator (Fig. 4.5c). This is not a problem in calculating the volume flow of such a propagator, since any intensity at zero displacement is multiplied with the zero value of the displacement axis (Eq. 4.6). However, loss of intensity at zero displacement increases the linear flow velocity and decreases the cross sectional area of flow (Eq. 4.7 and Eq. 4.5): water at the walls of vessels, which does not appear as flowing water, is indeed part of flowing water. Regions at the vessel walls are in fact part of the cross sectional area of flow of that vessel. As a solution to this problem the instrumental settings of an experiment can be chosen in such a way

that within Δ water can diffuse from the vessel walls into the regions where flow is present. Recently, the shape of a propagator of a laminar flow profile as a function of Δ has been published (20) showing a decreasing intensity at zero displacement with increasing Δ . The rms displacement due to diffusion within Δ combined with the velocity gradient of the flowing water near the vessel wall (depending on the vessel diameter and the volume flow through the vessel) determine the actual intensity of the propagator at zero displacement.

The comparison between the results obtained with the balance and with NMR, as presented in Fig. 4.7, show the accuracy of the quantification method. We found an agreement between both uptake measurements with a rms error of 0.11 mg/s, not by using an unclear constant to correlate NMR results to the actual ('balance') volume flow or by normalizing the volume flow to the maximum volume flow observed (22), but by calibrating NMR signal intensities to the averaged signal intensity of a reference tube. If, for certain studies, the labeling time Δ between the two PFGs is increased (increasing also t_{e1}), problems may arise from using a reference tube with water for calibration. The decay of the NMR signal, characterized by the relaxation time T_2 , varies in different tissues of the sample. Suppose the T_2 of the water in the reference tube ('doped' with paramagnetic ions to decrease T_2) differs substantially from the T_2 of the water in the xylem vessels and the time from signal excitation to first detection (t_{e1} in Fig. 4.3) is of considerable size compared to the T_2 values of the water in the tube and/or in the xylem vessels. The signal intensity of the water in the tube and in the xylem at the moment of detection will now be weighted with their different T_2 values and in the calibration this extra T_2 weight has to be considered. In our results the T_2 values of the water in the reference tube and in the xylem vessels were comparable (around 100 ms) and large compared to the first echo time (maximum 27 ms), so we did not experience these difficulties. If need be, it is possible to record pixel-propagators in combination with a T_2 experiment to link a T_2 value to every point of a pixel-propagator, though imaging time will be longer.

For in vivo applications of the described method in intact plants one assumption stated earlier has to be evaluated carefully: there should be no bi-directional flow within one pixel. In other words, the resolution of the NMR image has to be high

enough to discriminate between xylem and phloem tissue. In a pixel-propagator one can immediately see if both xylem and phloem flow are present: the propagator will show intensities at positive and negative displacements beyond the rms displacement of diffusing stationary water. Flow quantification is only hampered if the linear flow velocities in the two directions in the same pixel are of comparable size. In that case, one might consider using the rms displacement from stationary water of neighboring pixels to get rid of the stationary water in the pixel with bi-directional flow, after which positive and negative displacements can be evaluated separately. For full-grown intact plants active xylem and phloem areas are usually more than 100 μm apart, which means the resolution used here would be high enough to avoid bi-directional flow within one pixel. Increasing the spatial resolution of the images would increase measurement time drastically, a problem that might be solved by measuring at a larger magnetic field strength although examples of decreasing image quality with increasing magnetic field strength have been reported (28) for biological tissues (especially plant tissues).

In summary, it can be stated that relevant and accurate information about water transport can be acquired non-invasively with the presented method. The information is relevant in the debate about long distance transport in plants, and accurate since it does not need a model for flow to calculate flow characteristics. The method is demonstrated with *Chrysanthemum* stem segments, but can easily be used on intact plants (21) or any other system that fits within the NMR-imager. Since the overall uptake of NMR and balance measurements match, the local information of every pixel can be studied individually: the setup for the *Chrysanthemum* stem segments is being used as a model to investigate the restoration of original flow profiles and of hydraulic conductance for *Chrysanthemum* flowers after cutting.

Acknowledgement

We thank Ir. Jaap Nijse, Horticultural Production Chains Group, Wageningen University, for providing the photograph of the *Chrysanthemum* stem.

This research is supported by the Dutch Technology Foundation STW, applied science division of NWO (project WBI 3493).

References

1. J. B. Passioura, *Bot. Acta*, **104**, 405-411 (1991).
2. U. Zimmermann, F. C. Meinzer, R. Benkert, J. J. Zhu, H. Schneider, G. Goldstein, E. Kuchenbrod and A. Haase, *Plant Cell and Environment*, **17**, 1169-1181 (1994).
3. M. J. Canny, *Ann. Bot.* **75**, 343-357 (1995).
4. J. A. Milburn, *Ann. Bot.* **78**, 399-407 (1996).
5. M. T. Tyree, *J. Exp. Bot.* **48**, 1753-1765 (1997).
6. N. M. Holbrook and M. A. Zwieniecki, *Plant Physiol.* **120**, 7-10 (1999).
7. M. T. Tyree, S. Salleo, A. Nardini, M. A. Lo Gullo and R. Mosca, *Plant Physiol.* **120**, 11-21 (1999).
8. R. H. Swanson, *Flow, its measurement and control in science and industry*, **1**, 647-652 (1975).
9. Y. Cohen and M. Fuchs, *Agronomie*, **9**, 321-326 (1989).
10. J. E. A. Reinders, H. Van As, T. J. Schaafsma and D.W. Sheriff, *J. Exp. Bot.* **39**, 1211-1220 (1988).
11. T. J. Schaafsma, H. Van As, W. D. Palstra, J. E. Snaar and P. A. de Jager, *Magn. Reson. Imaging*, **10**, 827-36 (1992).
12. H. Van As, J. E. A. Reinders, P. A. de Jager, P. A. C. M. van de Sanden and T. J. Schaafsma, *J. Exp. Bot.* **45**, 61-67 (1994).
13. P. T. Callaghan, W. Köckenberger and J. M. Pope, *J. Magn. Reson., Ser. B*, **104**, 183-188 (1994).
14. E. Kuchenbrod, M. Landeck, F. Thürmer, A. Haase and U. Zimmermann, *Bot. Acta*, **109**, 184-186 (1996).
15. P. T. Callaghan, C. D. Eccles and Y. Xia, *J. Phys. E: Sci. Instrum.* **21**, 820-822 (1988).
16. W. Köckenberger, J. M. Pope, Y. Xia, K. R. Jeffrey, E. Komor and P. T. Callaghan, *Planta*, **201**, 53-63 (1997).
17. M. Rokitta, U. Zimmermann and A. Haase, *J. Magn. Reson.* **137**, 29-32 (1999).
18. D. Xing, S. J. Gibbs, J. A. Derbyshire, E. J. Fordham, T. A. Carpenter and L. D. Hall, *J. Magn. Res., Ser. B*, **106**, 1-9 (1995).
19. E. Kuchenbrod, E. Kahler, F. Thürmer, R. Deichmann, U. Zimmermann and A. Haase, *Magn. Reson. Imaging*, **16**, 331-338 (1998).
20. U. Tallarek, E. Rapp, T. Scheenen, E. Bayer and H. Van As, *Anal. Chem.* **72**, 2292-2301 (2000).
21. T. W. J. Scheenen, D. van Dusschoten, P. A. de Jager and H. Van As, *J. Magn. Reson.* **142**, 207-215 (2000).
22. M. Rokitta, A. D. Peuke, U. Zimmermann and A. Haase, *Protoplasma* **209**, 126-131 (1999).
23. T. C. Farrar and E. D. Becker, *Pulse and Fourier transform NMR*. New York: Academic Press (1971).

24. W. van Ieperen, U. van Meeteren and H. van Gelder, *J. Exp. Bot.* **51**, 769-776 (2000).
25. J. Nijssse, G. W. A. M. van der Heijden, W. van Ieperen, C. J. Keijzer, U. van Meeteren, *J. Exp. Bot.* **52**, 319-327 (1999).
26. C.-M. Tsai, E. W. Olcott and D. G. Nishimura, *Magn. Reson. Med.*, **42**, 682-690 (1999).
27. R.N. Bracewell, *The Fourier transform and its applications*. McGraw-Hill electrical and electronic engineering series. 381, New York: McGraw-Hill (1965).
28. H. C. W. Donker, H. Van As, H. T. Edzes and A. W. H. Jans, *Magn. Reson. Imaging*, **14**, 1205-1215 (1996).

5

Functional imaging of plants: a Nuclear Magnetic Resonance study of a cucumber plant.

T.W.J. Scheenen, A.M. Heemskerk, P.A. de Jager, F.J. Vergeldt and H. Van As

Functional magnetic resonance imaging was used to study transients of biophysical parameters in a cucumber plant in response to environmental changes. Detailed flow imaging experiments showed the location of xylem and phloem in the stem and the response of the following flow characteristics to the imposed environmental changes: the total amount of water, the amount of stationary and flowing water, the linear velocity of the flowing water and the volume flow. The total measured volume flow through the plant stem resembled the independently measured water uptake by the roots. A separate analysis of the flow characteristics for two vascular bundles revealed that changes in volume flow of the xylem sap were accounted for by a change in linear flow velocities in the xylem vessels. Multiple spin echo experiments revealed two water fractions for different tissues in the plant stem: the spin-spin relaxation time of the larger fraction of parenchyma tissue in the center of the stem and the vascular tissue was down by 17% in the period after cooling the roots of the plant. This could point to an increased water permeability of the tonoplast membrane of the observed cells in this period of quick recovery from severe water loss.

Introduction

Plant water relations deal with the distribution, movement and function of water in plant cells, tissues and organs, the development of internal water deficits and their significance to physiological processes, and how these phenomena are placed in an ecological context (1). With the development of new technologies (direct quantification of xylem tension with the xylem pressure probe and detection of air in xylem vessels by cryo scanning electron microscopy) plant water relations are currently one of the most controversial areas in plant physiology (reviewed in (2-5)): what are the driving forces behind water transport in plants? A number of groups have taken efforts in visualizing water transport in plants with nuclear magnetic resonance (NMR). Van As and Schaafsma (6) and Reinders et al (7, 8) used a portable NMR spectrometer (9) to measure spatially unresolved xylem water flow in a cucumber plant in situ and qualitatively examined the water flow through cut sections of a celery stem with NMR imaging (10). Meanwhile, Callaghan introduced the combination of static and dynamic NMR microscopy (11) and used it to investigate the origins of contrast in NMR images of biological tissues (12). Bentrup (13) indicated the importance of NMR-microscopy to botanists and Chudek and Hunter (14) and MacFall and Van As (15) reviewed NMR microscopy as a possibly useful tool in studying plants. After a study of phloem and xylem flow in castor bean seedlings (16) it was demonstrated that water transport can be measured localized, and even quantified, in larger plants (17), as well as in combination with fast imaging techniques to shorten measurement times (18, 19). A recent overview of many papers about NMR microscopy – both flow/diffusion and anatomy or water density and relaxational behavior applications – in plant science was written by Ishida et al. (20).

In this paper, we present a quantitative evaluation of temporal changes in different NMR imaging parameters (water fractions, spin-spin relaxation times and flow characteristics, of individual pixels and of multiple, added pixels from the same tissue) over a period of several days in a ten-week-old, growing cucumber plant. Water fractions and spin-spin relaxation times (T_2) are calculated by the use of a multiple spin echo (MSE) train (21). Water fractions and T_2 -values of different

tissues are interpreted without referring to any 'bound' or 'free' water, but with a central role for cellular compartment dimensions and the parameter H indicating the loss of magnetization at or near the boundaries of the compartments due to exchange over these boundaries into compartments with shorter relaxation times. Non-imaging studies (22-24) already indicated that the T_2 could be used to examine membrane permeabilities, which define the exchange rates of water over the cell or tonoplast membrane.

For every pixel, the displacement distribution of water within a certain time is also measured using a Pulsed Field Gradient Turbo Spin Echo (PFG TSE) pulse sequence (19) and from this displacement distribution the flow characteristics are calculated as described by Scheenen et al. (25). The total calculated volume flow through the plant stem is compared with the actual uptake of the plant, measured with a precision balance. Changes in water uptake are induced by the normal day/night cycle and a period of cooling the roots of the plant, which has a well-known effect of decreasing root permeability and therefore water uptake (1,7).

Flow sensitive and T_2 -imaging can relate local changes in biophysical parameters such as flow characteristics (directly) and membrane permeability (indirectly) to controlled changes in environmental conditions. In this way functional information is available with spatial resolution, which justifies the title 'functional imaging' for the combination of both imaging techniques.

Materials and methods

Plant material

Two-week-old Cucumber seedlings (*Cucumis Sativus* L.) were grown in a constantly aerated half-Hoagland solution (26) in a greenhouse of Unifarm, Wageningen, The Netherlands. The upper ten cm of the root system grew in an open, cylindrical pod to restrict root-branching within the dimensions of the NMR gradient probe, so later insertion in the gradient probe would not damage the roots. The temperature in the greenhouse was at least 25°C during the day, falling to values no lower than 21°C at night. During the photoperiod of 16 hours the plants

received direct sunlight and additional light from high-pressure sodium lamps. Under these conditions the plants grew to two meters in length in about ten weeks. Flowers were pinched out and occasionally the bottom leaf of the stem was removed with a razor blade to clear the lower 50 cm of the stem before moving the plant from the greenhouse to the NMR imager (removal of the last leaf was at least four days before installing the plant).

The instrumental setup

The NMR spectrometer consisted of an SMIS console (SMIS Ltd., Guildford, Surrey, UK), an electromagnet with a 14 cm air gap (Bruker, Karlsruhe, Germany) generating the magnetic field of 0.47 T and an external ^{19}F lock unit (SMIS) stabilizing the magnetic field. A custom-made shielded gradient probe (Doty Scientific Inc., Columbia, South Carolina, USA) with a 45 mm (i.d.) cylindrical bore, accessible from both ends was used. A solenoid radio frequency (rf) coil (diameter 15 mm), which induced and detected the NMR signal, was wrapped around an openable mould, placed around the plant stem. In less than two minutes the roots were taken out of the growth solution and put through the 45 mm bore of the gradient probe into an aerated container with identical growing medium. A cooling element inside the container could provide quick cooling of the roots (from 22°C to 3°C in five minutes) and the container itself was placed on a precision balance (LC3201D, Sartorius AG, Goettingen, Germany) below the magnet to monitor water uptake of the plant (see Fig. 5.1). The water uptake, as measured by the balance, was a moving average of 340 seconds: a single measurement was the mean uptake value in 20 seconds, every displayed point was the average of 17 measurements. The plant stem and coil mould were fixed inside the gradient probe to fix the position of the plant stem throughout all experiments. The climate chamber above the magnet held the stem and the leaves of the plant at $25 \pm 2^\circ\text{C}$ during the photoperiod (from 6.00 a.m. to 9.00 p.m., r.h. $65 \pm 5\%$, illumination about $2 \times 10^2 \mu\text{mol}/\text{m}^2\text{s}$ (PAR), depending on position of the leaves) and at $22 \pm 2^\circ\text{C}$ at night. After four days in the instrumental setup (growing several cm each day) the roots of the plant in the container were cooled to approx. 3°C for three hours, followed by another observation period of two days in the setup.

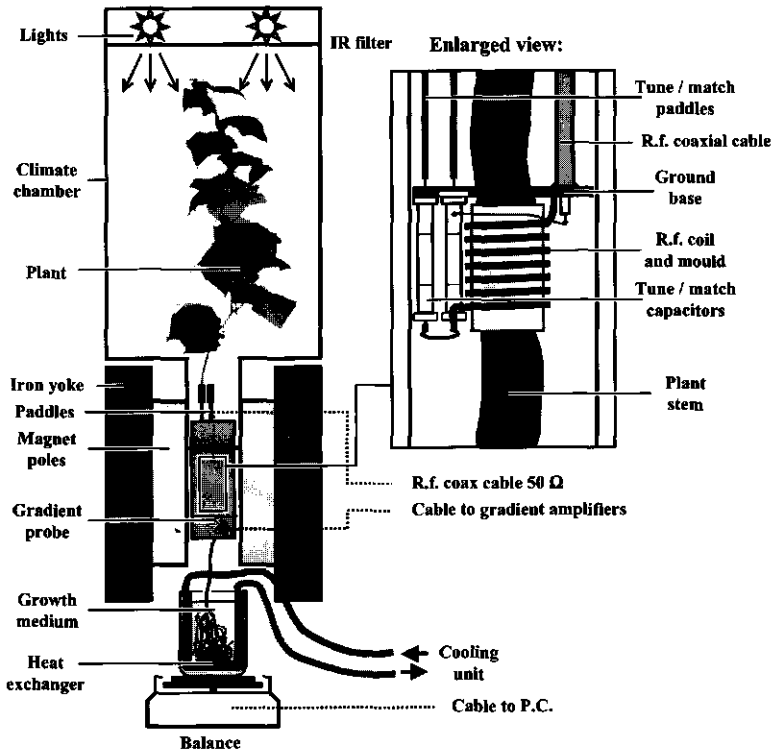


Figure 5.1: Schematic overview of the instrumental setup with the upper part of the cucumber plant in the climate chamber above the electromagnet and the roots in a container with a heat exchanger on the precision balance. The inset shows an enlarged view of the rf coil, wrapped around the stem, in the center of the gradient probe.

NMR imaging pulse sequences

Two different NMR imaging pulse sequences were used to monitor the plant water status and transport: a multiple spin echo (MSE) experiment (21) to evaluate the echo decay of the NMR signal per pixel and a PFG TSE sequence (19) to calculate the flow characteristics per pixel (25). Following the initial slice-selective 90° -pulse, both sequences used hard 180° -pulses in the spin echo trains to keep inter echo intervals short and sample as much of the signal as possible during its decay. The use of spin echoes, combined with large read out gradients (receiver bandwidth 50 kHz), was necessary to overcome magnetic field inhomogeneities, caused by numerous small air spaces in the plant tissues (27). Within half the acquisition time of one echo (1.28 ms) the signal decay per pixel due to T_2^* was negligible and the in-plane resolution was not affected by extra signal attenuation.

In the MSE experiment an echo train was acquired for every step of the phase encode gradient, so one could reconstruct an image for every echo in the train. The real part of the phased complex NMR signal $S(t)$ of every pixel in the images in time could be characterized by an n - exponential decay curve:

$$S(t) = \sum_{i=1}^n A_i \exp(-R_{2i}t) \quad [1]$$

in which A_i is the signal amplitude of fraction i at the moment of excitation ($t=0$) and R_{2i} is the corresponding characterizing relaxation rate ($= 1/T_{2i}$). We used mono and bi-exponential fits to extract the biophysical parameters amplitude and relaxation time from different tissues in the cucumber plant stem.

In the PFG TSE experiment (19) the echo train was used to shorten imaging time. Every individual echo was phase-encoded separately, which decreased the measurement time for one image with a factor equal to the number of echoes used in the TSE train. The displacement of water molecules in the pixels was monitored with two stepped pulsed field gradients in the longitudinal direction (i.e. along the plant stem) with amplitude g , duration δ and spacing Δ ($\delta < \Delta$), which modulated the complex NMR-signal in amplitude and phase. A Fourier transformation of this signal (28) gave the displacement propagator: the distribution of displacements of the water molecules within Δ for every pixel in the TSE image. The propagator of stationary water is symmetric around zero displacement (with a Gaussian shape, if the water can diffuse unrestricted), whereas flowing water has a net displacement within the time Δ . The flow characteristics were extracted from the flowing part of every pixel-propagator without assuming any model for the flow-profile within the corresponding pixel, using the NMR signal intensity of a reference tube for calibration (25).

In the PFG TSE experiment two different parameter sets were used to obtain either high time or high spatial resolution: a 64×64 image matrix with a field of view of 11.0 mm was measured in 21 minutes (repetition time 2.5 s), whereas a 128×128 image matrix with a field of view of 12.8 mm took 42 minutes of measuring time. The displacement encoding parameters were changed with changing water uptake caused by the day/night cycle (day: 32 g -steps from $-g_{\max}$ to $+g_{\max-1}$, δ 2.5 ms, Δ 7.0

or 10.0 ms, g_{\max} 0.457 to 0.385 T/m, night: δ 2.5 ms, Δ 15.0 ms, g_{\max} 0.337 T/m). The matrix size of the MSE experiment was always 128 x 128 pixels with a field of view of 12.8 mm and took 26 minutes of total acquisition time (repetition time 3 s). All data processing was performed with IDL (RSI, Boulder, Colorado, USA).

Results

MSE imaging

Four images were constructed from a mono-exponential fit to the NMR-signal decay in the echo train of the MSE experiments (Fig. 5.2): (b) an amplitude image, representing the fitted amount of water of every pixel in the image, (c) an R_2 image, characterizing the signal decay rate, (d) a T_2 image, revealing better contrast in long T_2 -values, and (e) a χ^2 image displaying the quality of the fit ($\chi^2 = \sum_{i=1}^N (S_i - f_i)^2 / (N - 2)$ in which N is the number of echoes and S_i and f_i the value of the i^{th} data point and its fitted value). The χ^2 image does not show any intensity related to the anatomy of the stem, which means that there were no detectable systematic deviations of the data from the mono-exponential fit. Figure 5.2a is a schematic overview of a transverse slice through a cucumber plant stem. The pixels in the center of the stem with no intensity in the amplitude image correspond with the pith cavity in the stem. The parenchyma in the central cylinder can be divided into inner and outer parenchyma on the basis of a small difference in amplitude (water density), visualized in Fig. 5.2f+g. The central cylinder of the stem generally contains four big and five smaller vascular bundles, which can clearly be distinguished in the R_2 image: images h and i in Fig. 5.2 show T_2 images of the four innerbundles and five outerbundles without xylem vessels. The tissue in the vascular bundles has T_2 -values in the order of 130 ms: large xylem vessels in the bundles are visible with long T_2 -values (Fig. 5.2j; 300 ms). A thin ring, small in amplitude and short in T_2 , separates the central cylinder from the cortex. The thin epidermis is visible with high intensity in the R_2 image (T_2 90 ms). The dot above the plant stem is a reference tube filled with an aqueous $MnCl_2$ solution to shorten the T_2 of the water to 150 ms ('doped' water).

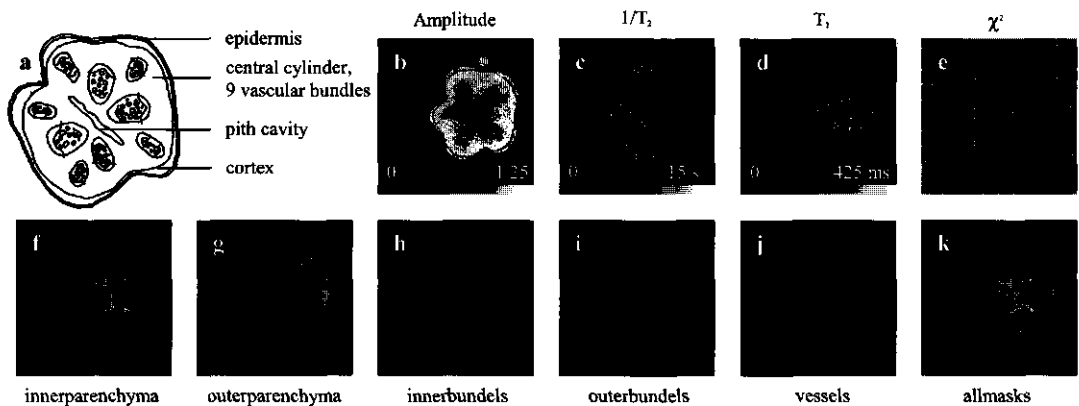


Figure 5.2: NMR images, calculated from one MSE experiment of a cucumber plant. The different tissues in the schematic overview (a) of a slice through a cucumber plant stem can clearly be recognized in the R_2 image (c) and T_2 image (d). The amplitude or water density image (b) is normalized to the mean intensity of nine pixels in the reference tube. The scale of the color table is somewhat larger than 1.0 since some points in the image may be greater than 1.0 because of noise. Image (e) reflects the χ^2 of the mono-exponential fit to the decay curve of every pixel. Images (f) to (j) are T_2 images of areas, selected with a mask based on amplitude and T_2 value. In image (k) all selected areas are combined leaving some pixels that could not be clearly assigned to a certain tissue. Also the cortex and the reference tube are not selected in any of the shown masks. Parameters of the NMR experiment: 128 x 128 matrix, field of view 12.8 mm, slice thickness 3 mm, repetition time 3 s, first echo at 6.4 ms, echo time in echo train 4.6 ms, 64 echoes.

As was mentioned earlier, we found no systematic deviations of the data from the mono-exponential fit related to the stem anatomy. This implies that the signal-to-noise ratio (SNR) of the decay curve of an individual pixel was too low for a meaningful multi exponential fit, although even for an individual pixel a multi exponential decay is expected, because of the different proton pools present in a pixel (water in different cells and/or different cell organelles). Averaging the decays from the pixels of the masks in Fig. 5.2 f to j greatly improved the SNR and enabled bi-exponential fits to the decaying NMR-signal. Fig. 5.3a displays the added NMR-signal decay curve of the pixels in the reference tube and a mono-exponential fit to the curve (no partially filled pixels included). A plot of the residuals of the fit shows only noise (Fig. 5.3b). Since pixels within the reference tube were completely filled with doped water the calculated amplitude could serve as a 100% water density standard for normalization of the amplitudes. The systematic deviation from zero of

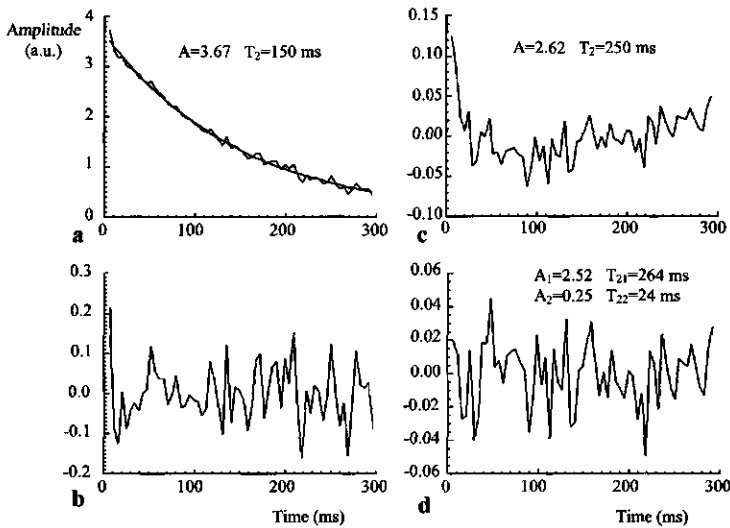


Figure 5.3: Added NMR signal decay curve of pixels in the reference tube and a mono exponential fit to the curve (a), the plot of the residuals of the fit to the curve (b) and the residuals of a mono-exponential (c) and a bi-exponential (d) fit to the added signal of all pixels in the innerparenchyma (Fig. 5.2f). The residuals of the mono exponential fit to the innerparenchyma signal decay is not a straight noisy line, which is the case in the residuals of the bi-exponential fit. Notice the difference in noise level between (b) and (d): more pixels could be used in the innerparenchyma signal decay curve, which improves the SNR. Experimental details as in Fig. 5.2.

the plot of the residuals (Fig. 5.3c) of a mono-exponential fit to the averaged decay curves of one of the selected areas in the image (the innerparenchyma Fig.2f) implies that there is signal left in the residuals. However, the plot of the residuals of a bi-exponential fit to the same data displays only noise (Fig. 5.3d): two exponentials describe the data well. The mean water density of the innerparenchyma is $75\% \pm 2$ (total amplitude of the fit compared to the reference tube amplitude), of which – ascribing the two exponentials to two water fractions – a fraction of $9\% \pm 1$ has a T_2 -value of 24 ± 5 ms and $91\% \pm 1$ has a T_2 -value of 264 ± 4 ms (errors are standard deviations). The tissues in Fig. 5.2f to j can be analyzed in the same way, revealing the time course of the water density and corresponding T_2 -values of the two water fractions during three days, as will be shown later.

Dynamic PFG TSE imaging

Contrary to MSE-imaging, in which multiple echoes are used to calculate amplitudes and relaxation times, TSE imaging uses echoes from different

refocusing times after excitation to construct an amplitude image. A certain amount of T_2 weighing is incorporated in the image, as was already mentioned with the introduction of the technique (29). If relaxation times are long, compared to the time from excitation to the first echo that determines the integral of the image in the phase encode direction (19), signal attenuation due to T_2 is small and the TSE image will hardly show any T_2 contrast. With the used time from excitation to the first echo (21 ms) the TSE image of Fig. 5.4a has only minor deviations from the calculated amplitude image in Fig. 5.2b; the low amplitude ring between the central cylinder and the cortex with short T_2 has lost some intensity in the TSE image compared to the calculated amplitude image. In both the TSE and MSE image the innerparenchyma has also lost some intensity because of saturation. The repetition time of the TSE experiment was 2.5 s (3.0 s in MSE) which was not long enough for the protons in the innerparenchyma to return to equilibrium completely (T_1 -values might have exceeded 1 s).

Analyzing a PFG TSE experiment as described elsewhere (25), we calculated the amount of stationary water (Fig. 5.4b), the amount of flowing water (Fig. 5.4c), the mean linear velocity of the flowing water (Fig. 5.4d) and the volume flow (Fig. 5.4e) for every pixel in the TSE image. Using the reference tube for calibration, the intensities of Fig. 5.4a to c represent an amount of water between 0 and 1.0, where 1.0 is the averaged intensity of nine pixels in the reference tube, representing 100% water density. The mean linear flow velocities of the flowing water in the xylem vessels reached levels up to 8 mm/s, where maximum velocities could exceed 15 mm/s in the center of a vessel. Vessels in eight out of the nine vascular bundles are visible in Fig. 5.4c. With the highest linear flow velocities in the vessels of three vascular bundles in the center of the stem, the majority of the water transport in the shown slice of the cucumber plant stem occurred in those three vascular bundles. We set a positive threshold value ($\sim 2 \times$ r.m.s. noise level) in the volume flow image to calculate the total water transport through the slice in the plant stem. The total volume flow was a summation of values of those pixels that exceeded the threshold and had at least one neighboring pixel, also with a value above this threshold. The calculated total volume flow through the slice in the plant stem will be compared with water uptake values from the balance measurements (see below). The calculation of the flow characteristics can also be performed with a summation of all

propagators of one vascular bundle. For two representative vascular bundles B1 and B2, indicated in the mask of all pixels with flowing water for every bundle in Fig. 5.4f, the changes in flow characteristics in time will be considered in more detail.

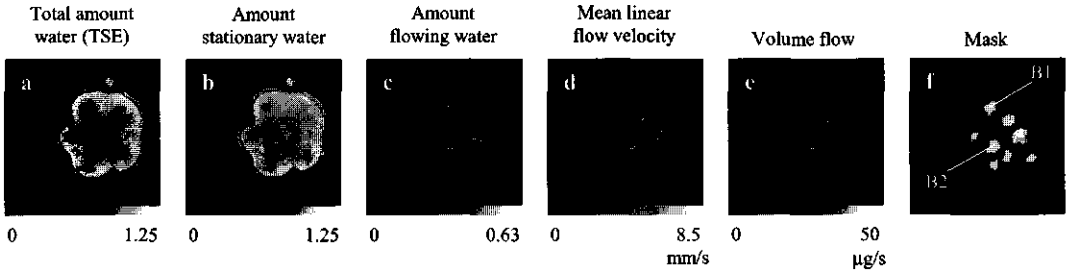


Figure 5.4: NMR images, calculated from a PFG TSE experiment. The total amount of water in the TSE image (a) closely resembles the calculated water density image in Fig. 5.2b. Images (a), (b) and (c) are normalized to the mean intensity of nine pixels in the reference tube ($=1.0$). The amount of flowing water can be recalculated in the cross sectional area of flow for every pixel, assuming that a vessel is homogenous along the direction of the plant stem over the thickness of the slice (3 mm). Apart from the cross sectional area of flow, also the linear flow velocity of the flowing water (d) and the volume flow (e) can be calculated. Image (f) indicates the individual vascular bundles as eight gray areas, representing all pixels with flowing water for every bundle. For bundles B1 and B2 the flow characteristics were recalculated with added propagators and studied in more detail. Parameters of the NMR experiment: 128×128 matrix with field of view 12.8 mm, repetition time 2.5 s, 32 echoes in TSE train, Δ 14.5 ms, δ 2.5 ms, g_{max} 0.330 T/m.

The parameters for the PFG TSE experiments were set to measure the xylem flow: the flow-encoding time Δ between the two pulsed field gradients was short (7 to 15 ms), since linear flow velocities in the xylem were high (locally >15 mm/s). With short Δ -values it is difficult to distinguish displacements of water molecules originating from self-diffusion from displacements of water molecules that flow slowly in e.g. phloem sieve tubes. This so-called dynamic range problem is illustrated in Fig. 5.5: the sum of all propagators that show xylem flow has a large shoulder from displacements 0 to 190 μm , whereas the sum of all propagators in phloem regions reveals only a small asymmetry of a Gaussian shape. Merely a qualitative evaluation of phloem flow is possible by subtracting the image representing a displacement of +14 μm from the image representing a displacement of -14 μm , as indicated by I-II in Fig. 5.5b. This procedure unveils the

regions of phloem flow for the measured plant in Fig. 5.5b: adding all intensities in the phloem regions gives a rough indication of the phloem flow through the slice.

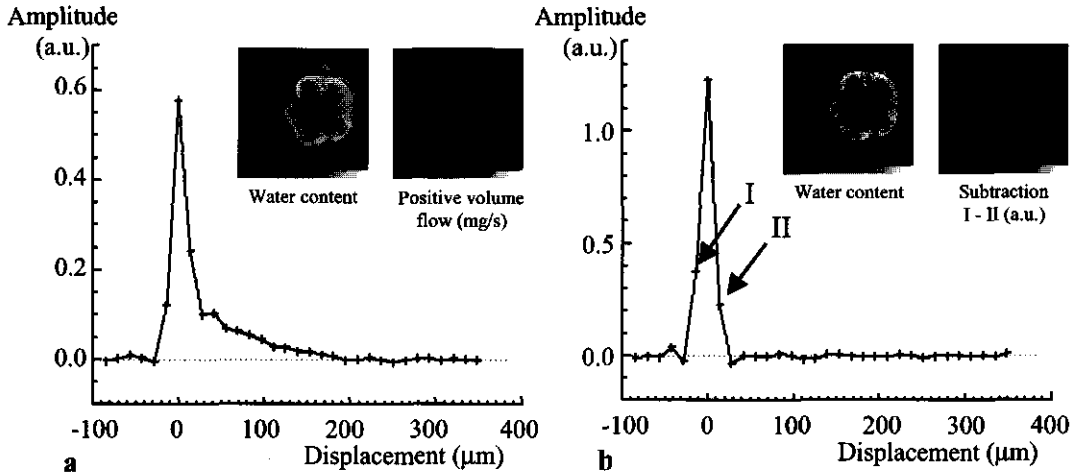


Figure 5.5: The added propagator of all pixels of the image in Fig. 5.4 that show xylem flow (a) and the added propagator of pixels in phloem tissue (b). In the inset in (a) the images of the calculated water density and volume flow are shown. Subtracting point II from I for every pixel propagator gives an indication of phloem flow as shown in the images in the inset in (b). Phloem flow is visible at the periphery of the vascular bundles with a radial symmetry, as can be expected from the bicollateral anatomy of the vascular bundles.

Functional imaging during day/night cycle and root cooling

After four days of acclimatization and growth in the experimental setup the roots of the cucumber plant were cooled rapidly for three hours with the heat exchanger in the container with growth medium. Cooling the roots severely inhibited the uptake of water by the plant, decreasing to levels around nocturnal uptake values before warming up the roots again. An outline of the uptake of the plant from the night before root cooling to two days after cooling is presented in the upper part of Fig. 5.6. The transient response of the plant to turning lights on and off is evident, alike the reaction to root cooling. Water uptake by the roots was inhibited when the roots were cooled but transpiration of water from the leaves continued, resulting in a net water loss of the plant. The prolonged period of root cooling caused the leaves to wilt and the stomata of the leaves to close (1), as shown before in a previous NMR study of a cucumber plant (7). After warming up the roots, the uptake restored only

partially, but with closed stomata of the wilted leaves water uptake exceeded transpiration and the plant recovered. Within four hours after warming up the roots again (before the lights were turned off), the plant did not show any sign of water deficit anymore. The increase in water uptake in the first four days (data not shown) reflected the increase of leaf surface of the growing plants. The day after root cooling the uptake was lower than before root cooling. On the last day, shown in Fig. 5.6, water uptake was almost back to the level before root cooling.

The total volume flow through the imaged slice of the plant, measured with NMR and calculated as indicated earlier, is also plotted in Fig. 5.6. Again, the response to the day/night cycle and the steep decrease in volume flow as a reaction to root cooling are evident. Moreover, from the start of root cooling to the end of the shown experiment the calculated NMR data comes close to the balance uptake values, so nearly all water that actually flows through the xylem has been localized. Early on the day of root cooling the calculated NMR flow does not coincide with the high

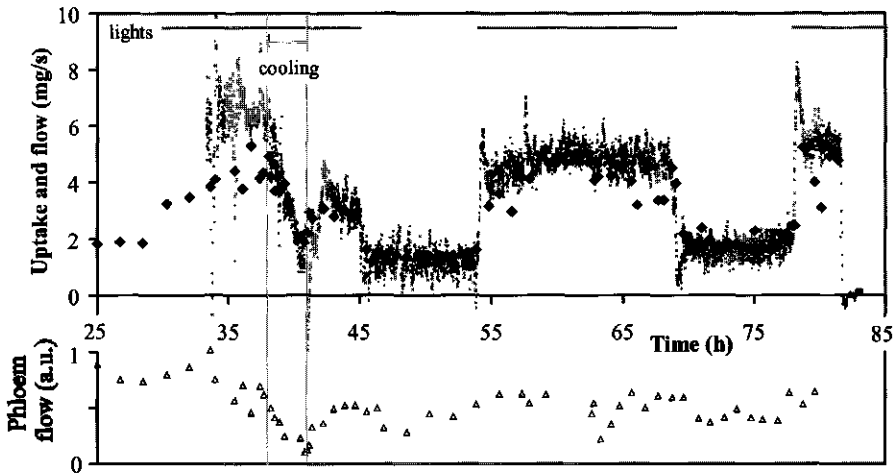


Figure 5.6: The water uptake by the cucumber plant measured with the balance (small dots) and with PFG TSE NMR (black diamonds). The ground level of evaporation out of the aerated container, visible at the end of the experiment (83 hours) when the plant was taken out of the setup, is set to zero. In the lower part of the figure an indication for phloem flow in arbitrary units is plotted (open triangles). The gray lines in the top of the figure indicate the light on periods. The period of root cooling is indicated with two vertical lines. Parameters of the NMR experiments: 128 x 128 matrix with field of view 12.8 mm or 64 x 64 matrix with field of view 11.0 mm, repetition time 2.5 s, 32 echoes in TSE train, Δ , δ and g were varied with expected flow velocities.

uptake values, measured with the balance. Although the balance measurements in that region are quite noisy or even absent because of too fierce aeration, one can still observe a difference between the balance measurement (~ 6.5 to 7.0 mg/s) and the calculated NMR flow (~ 4.5 mg/s) (the reason for this difference will be discussed below). A qualitative evaluation of phloem flow, made as described in Fig. 5.5b is displayed in the lower part of Fig. 5.6. The intensity of the phloem flow is in arbitrary units and shows only a reaction to root cooling: any response to the day/night cycle is not clear from the data.

The course of the flow characteristics, calculated for two complete vascular bundles (indicated in Fig. 5.4f), is shown in Fig. 5.7. The volume flow of the bundles in Fig. 5.7c resembles the overall uptake of the plant. Bundle B2 (see Fig. 5.4f), indicated with triangles in Fig. 5.7, transports more than twice the amount of water (0.94 ± 0.02 s.e. (standard error) mg/s over the first day after root cooling) than bundle B1, indicated with diamonds in Fig. 5.7 (0.41 ± 0.02 s.e. mg/s). Transients in volume flow are a result of changing linear flow velocities in both vascular bundles. Significant changes in the cross-sectional area of flow are not visible (Fig. 5.7a), because of a low signal-to-noise ratio (mean cross-sectional area of flow of bundle B1 is 0.16 ± 0.02 s.d. (standard deviation) mm^2 over the whole experiment, 0.18 ± 0.03 s.d. mm^2 for bundle B2). The flow characteristics for the other vascular bundles are comparable to the two shown in Fig. 5.7: the strong reaction of the mean linear flow velocity to the day/night cycle and to root cooling is responsible for the transients in the volume flow; the signal-to-noise ratio of the cross-sectional area of flow is not high enough to discern a significant change.

For two of the five selected tissues in Fig. 5.2, the innerparenchyma and the outerparenchyma, the results of the bi-exponential fits over the three days are shown in Fig. 5.8. The water fractions of the two components are normalized to the mean intensity of 9 pixels in the reference tube. The total water density of the outerparenchyma tissue (the sum of the two water fractions) comes close to 1, which can also be seen in the amplitude image, calculated with one exponent in Fig. 5.2b, where the intensity of the outerparenchyma is as large as the intensity in the reference tube. The total water density of the innerparenchyma tissue is around 0.75 to 0.80 ($A_1 + A_2$), possibly influenced by partial saturation because of a long T_1 ,

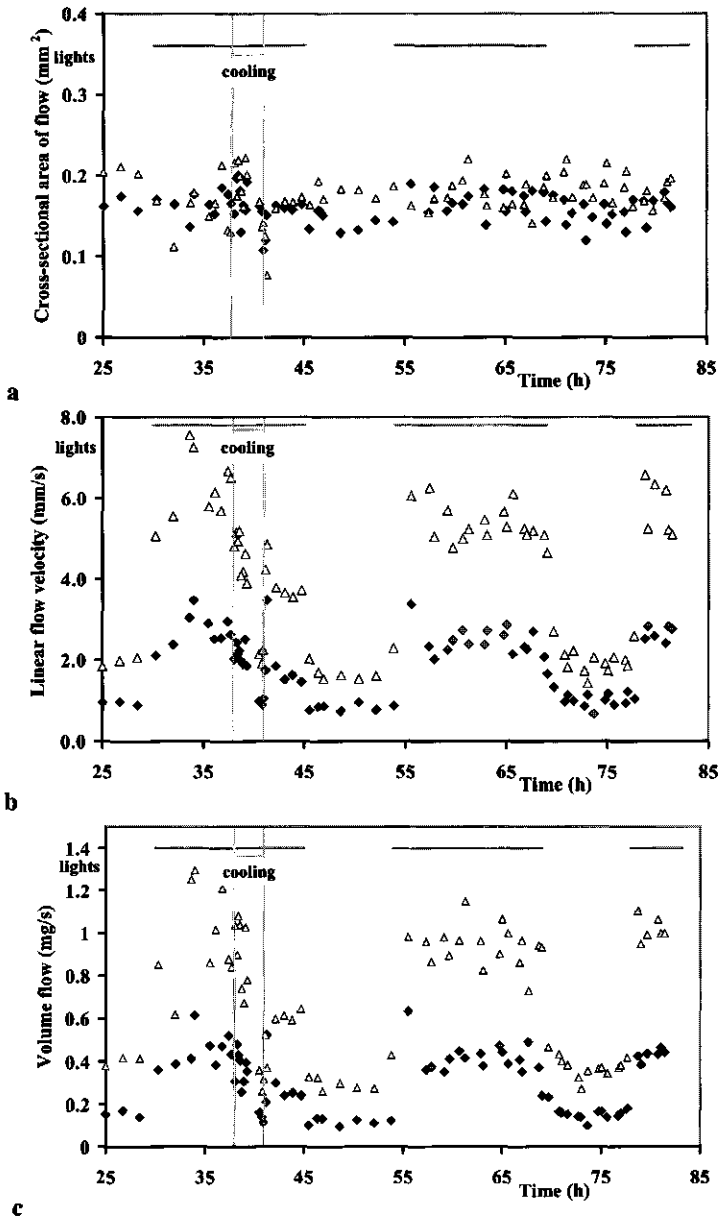


Figure 5.7: The flow characteristics for two vascular bundles, calculated with the summation of all propagators that show flow within one bundle. The cross-sectional area of flow of a bundle in mm² (a) multiplied with the mean linear flow velocity of the same bundle in mm/s (b) equals the volume flow in mm³/s or mg/s (c). Again, the gray lines in the top of the figure indicate the light on periods and root cooling is indicated with two vertical lines. The diamonds indicate a peripheral vascular bundle (area B1 in Fig. 5.4f), whereas the triangles indicate one of the four vascular bundles in the center of the stem (area B2 in Fig. 5.4f).

as was mentioned before. The two water fractions of the outerparenchyma tissue remain constant throughout the experiment: no influence of the day/night cycle or root cooling can be discerned either in water fraction (Fig. 5.8a) or in T_2 (Fig. 5.8b). The amplitude of the large fraction of the innerparenchyma tissue increases about 5% in the last hour of root cooling and the period with the lights on thereafter, which might be due to a decrease in T_1 that cancels the possible partial saturation. The T_2 of this fraction shows a relation with the day/night cycle and with root cooling: with lights off the T_2 of the fraction is around 0.26 s, dropping to around 0.23 s with the lights turned on with a steep decrease to around 0.19 s just after the period of root cooling. The T_2 of the smaller fraction of the innerparenchyma tissue does not show a significant dependence on day/night cycle or root cooling. Although the data of

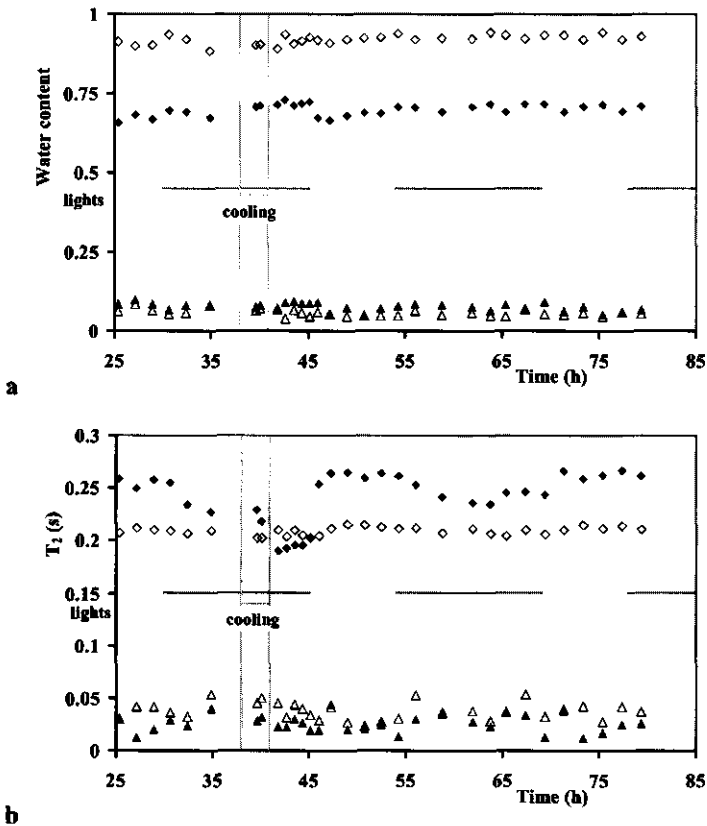


Figure 5.8: The water density (a) and corresponding relaxation time T_2 (b) for two fractions of the innerparenchyma tissue (closed diamonds and triangles) and the outerparenchyma tissue (open diamonds and triangles), calculated with a bi-exponential fit to the averaged NMR-signal decay of all pixels from the regions indicated in Fig. 5.2f and g.

the inner and outer vascular bundles (Fig. 5.2h and i) are noisier because of the smaller amount of pixels in that tissue, both tissues show similar reactions to root cooling: a decrease in T_2 of 15 to 20% of the large water fraction just after the period of root cooling (data not shown).

Figure 5.9 recapitulates the results of one MSE and one PFG TSE experiment with a T_2 image and an image with water density and flow information in two directions. The regions of xylem and phloem flow do not overlap, so the spatial in-plane resolution of $100 \times 100 \mu\text{m}$ is high enough to distinguish between the two. Not surprisingly, the vascular bundles with the largest xylem vessels, visible as dots with long relaxation times, show the largest amounts of water flowing from roots to shoot. Phloem flow is only visible on the exterior side of those bundles that show the larger quantities of xylem flow.

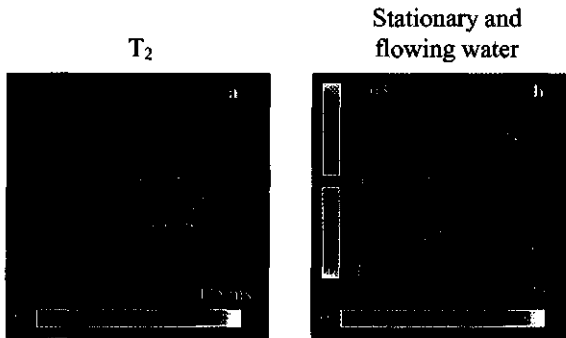


Figure 5.9: Two images summarizing an MSE and a PFG TSE experiment. The image in (a) is the T_2 -image from Fig. 5.2d. The image in (b) is an image of the water density (cf. Fig. 5.4a), overlaid with an image of the amount of water flowing upwards in the xylem (cf. Fig. 5.4c) and an image with a qualitative indication of phloem flow (inset in Fig. 5.5b). The green color scale in (b) represents the total amount of water, whereas the blue color scale represents the amount of flowing water, both relative to the average intensity of nine pixels in the reference tube ($= 1$). The red color scale indicates phloem flow intensity qualitatively, in arbitrary units.

Discussion

In general, care must be taken in interpreting multi-exponential NMR decay curves of plant tissue, since multi-exponential relaxation can be caused by cellular

inhomogeneity, subcellular compartmentation (30) and the presence of relaxation sinks at the boundaries of (both homogenous and inhomogeneous) cells or cell compartments (23, 31). However, if an amplitude and T_2 image, although calculated with a mono-exponential fit, is used to differentiate between structural tissues, the NMR-signal decay curve of a number of pixels within these tissues can be averaged to increase the SNR, without introducing large cellular inhomogeneities. If this curve would be analyzed with a three-exponential fit three water fractions could be assigned to different cellular compartments (22, 23, 32): the vacuole (large fraction with long T_2), the cytoplasm (small fraction with intermediate T_2) and the cell wall and extracellular water (small fraction with short T_2) (23, 32). In this study we fitted the decay curve with a bi-exponential function because the signal-to-noise ratio was too low to extract a third component with acceptable accuracy (other reasons were that the decay curve was cut off before the signal decayed to zero and the first part of the decay curve (time before first echo) was not available). The larger fraction of the two, with the long T_2 , can still be assigned to vacuolar water, whereas the small fraction with short T_2 represents water from the cytoplasm and maybe contributions of water inside the cell wall and extracellular water. The T_2 of the large water fraction is a weighted mean average value of the T_2 of the water in the individual vacuoles, which differ slightly in size and in T_2 . Changes in the calculated T_2 can be explained with a model, that describes a relation between the observed T_2 of the vacuolar water fraction and the average intrinsic bulk T_2 of the water in the vacuoles, the average surface sink strength density H and the average dimensions of the vacuoles (23, 33):

$$1/T_{2,obs} = H(1/r_x + 1/r_y + 1/r_z) + 1/T_{2,bulk} \quad [2].$$

The dimensions of the vacuoles can be expressed in the average radii r_x , r_y and r_z in three directions. H indicates the rate of magnetization loss at the vacuolar membrane, either due to wall relaxation or to exchange of water with the short- T_2 cytoplasm, or even exchange between extracellular water and water in the vacuole (passing through the cytoplasm). The validity of the relation between $1/T_{2,obs}$ and cell dimensions for vacuolized cells has recently been demonstrated for cells in different

internodes in the apical zone of maize and pearl millet plants (van der Weerd et al., *Journal of Experimental Botany*, accepted).

How can this model be used to interpret the dramatic changes in time in the T_2 of the vacuolar water fraction of the innerparenchyma tissue as shown in Fig. 5.8? The largest change in T_2 is the 17% drop (from 0.23 to 0.19 s) in the 4.5-hour period just after root cooling. The time and period in which the T_2 is shorter rules out a temperature effect: the temperature of the roots had already been set back to normal when T_2 -values had just dropped. A decrease in stem diameter, as reported by Reinders et al. (7), can not be the cause of the drop either, since the stem diameter is back to the original value within 15 minutes after cooling. The water density of the vacuolar water fraction increased only about 5% in the period of smaller T_2 -values, indicating that the amount of water inside the vacuoles hardly changes, and moreover, that the volume of the vacuoles (r_x , r_y and r_z) remains constant within 5%. The vacuoles are not likely to accumulate large amounts of paramagnetic ions, which would lower the value for $T_{2,bulk}$, simply because these ions are not present in substantial amounts. The only variable that can be responsible for the 17% decrease in T_2 is H .

The increase in H , the rate of magnetization loss over the vacuolar membrane, might indicate an increase in exchange speed of water between the cytoplasm and the vacuole: an increase in the tonoplast permeability for water. More protons from water, crossing the vacuolar membrane, lose their magnetization in the cytoplasm or, if the distance from tonoplast membrane to cellular membrane is small (in the order of 1 μm), in the cell wall. In this way, even a change in plasmalemma membrane permeability could affect H and thereby also $1/T_{2,obs}$.

The two water fractions in the outerparenchyma tissue do not show any changes in water density and T_2 over the studied period of time, contrary to the innerparenchyma tissue and the tissue in the inner and outerbundsels that all clearly show a decrease in T_2 of the large (vacuolar) water fraction. In the period after root cooling, in which the plant recovered from severe water loss, the decrease in T_2 in tissue around xylem vessels and tissue in the innerparenchyma indicates an increase in H , which in turn could mean an increase in tonoplast and/or cell

membrane permeability, important for restoring the water balance of the plant. Of course this hypothesis needs to be tested further.

Generally the total water uptake in Fig. 5.6, calculated from the PFG-TSE data, comes close to the water uptake values, measured with the precision balance, although before cooling the roots the NMR-values are too low. A reason for calculating systematically deviating volume flow values can be found in the presence of vessels with too high linear flow velocities, which results in large maximum displacements within Δ . The surface of the flowing part of the pixel-propagator represents the amount of flowing water (25, cf. Fig. 5.5a). A large maximum displacement at a given amount of flowing water stretches the pixel-propagator all over the displacement axis, lowering the amplitude into the noise, where it cannot be quantified anymore.

The flow characteristics of the complete individual vascular bundles in the experiment as shown by two representative bundles in Fig. 5.7 reveal the development of the cross-sectional area of flow, the mean linear flow velocity and the volume flow in absolute quantities. The difference in cross-sectional area of flow for the two bundles is small (0.18 ± 0.03 s.d. - 0.16 ± 0.02 s.d. mm^2), whereas the difference in volume flow (and mean linear flow velocity) is more than a factor of 2 (0.94 ± 0.02 s.e. to 0.41 ± 0.02 s.e. mg/s). Assuming an equal pressure difference over the two bundles, the volume flow through a circular tube or vessel is related to the fourth power of the vessel radius (the Hagen-Poiseuille law (34)). Therefore the bundle with the higher flow rates must have more vessels with larger diameters and less vessels with smaller diameters than the other bundle to keep the cross-sectional areas (almost) equal. From Fig. 5.7a one cannot conclude that the period of root cooling had a structural effect on the cross-sectional area of flow: changes in the volume flow rate are accounted for by the linear flow velocities.

It is difficult to discern extremely slow flow from stationary water when using short Δ -values. Although phloem flow has been visualized qualitatively, a quantitative evaluation requires long Δ -values. With these long observation times severe signal loss between excitation and detection of the first echo needs to be avoided. For this purpose it is more appropriate to use a stimulated echo version of the PFG TSE

technique (35), or another flow-sensitive NMR imaging pulse sequence that uses a stimulated echo (36).

The overlay image in Fig. 5.9b suggests that xylem flow and phloem flow are correlated: those vascular bundles that are most active in xylem transport, also take care for the majority of phloem transport. Münch (37) already proposed that the surplus of water from arriving phloem sap that had originally transported solutes could be released in the xylem to be transported back towards the leaves. Whether this implies a positive correlation between xylem and phloem flow has to be investigated further.

The presented study describes the results of one cucumber plant. Three other investigated plants (data not shown), differing slightly in size and age, displayed similar reactions to root cooling and the day/night cycle concerning water loss of the plant, changes in xylem flow and T_2 . In larger plants with larger water uptake again problems with high linear flow velocities occurred, but the calculated NMR flow indicated very clearly the trend in water uptake (again, with volume flow values calculated from the NMR measurements being smaller than the uptake, measured with the balance). In one larger plant phloem flow could be discerned on the interior and exterior sides of three large vascular bundles and in four other bundles (exterior). In this plant phloem flow was clearly more intense at night than during daytime, again being the smallest while the roots were cooled.

Functional MRI in plants, as demonstrated here, is a unique tool to study plant responses to different water-availability conditions, cold treatment or other biotic and abiotic stressors. Post-genomic studies of (genetically modified or wild type) plants with functional MRI could reveal the functionality of gene expression at cell, organ and whole plant level in water-related processes which are crucial for plant function. Another application could be the induction and refilling of air embolisms in plants to study possible mechanisms behind refilling. Changes in total amount of water, amount of flowing water, amount of stationary water, volume flow and T_2 can be studied on tissue or even single vessel or pixel level. If functional MRI is combined with other techniques, e.g. the xylem pressure probe, one could study

xylem pressure and xylem flow at the same time to validate or disaffirm current hypotheses in plant water relations.

Conclusions

The combination of T_2 and detailed flow imaging experiments reveals the functioning of plants in response to environmental changes by tracing water transport in xylem and phloem and the spin-spin relaxation time T_2 . The analysis of the MSE experiments, aided by image guided tissue differentiation, with a bi-exponential decay curve reproducibly revealed two water fractions for several tissues. The T_2 of the large fraction can be assigned to vacuolar water. A decrease of the T_2 of the vacuolar water fraction of the innerparenchyma tissue and the vascular tissue surrounding the xylem vessels after a period of cooling the roots can be attributed to an increase in the surface sink strength density. This increase in H , in the period in which the cucumber plant recovers from severe water loss, may indicate an increased permeability for water of the tonoplast and plasmalemma membrane.

Water transport through the xylem vessels is localized and quantified with the flow imaging experiments, indicating, apart from a normal day/night cycle, a large drop in water uptake of the cucumber plant when the roots are cooled. Since the NMR quantification of flow in the xylem vessels matched uptake values, measured with a balance, it is now possible to study water transport separately in every vascular bundle, and for large xylem vessels even individually. Although the presented flow imaging experiments were optimal to measure the xylem flow, phloem flow could also be discerned. A day/night cycle in phloem flow was not found, but the reaction to root cooling was unambiguously: phloem flow dropped during and just after the period of root cooling. The utilization of the two imaging techniques in other plants and the study of individual xylem vessels and surrounding tissues in the cucumber plants are two promising aspects for the near future.

Acknowledgement

This research was supported by the Dutch Technology Foundation STW, applied science division of NWO (project WBI 3493).

References

1. R. O. Slatyer, *Plant-water relationships*. London: Academic Press (1967).
2. U. Zimmerman, A. Haase, D. Langbein and F. Meinzer, *Philos. Trans. R. Soc. Lond. Ser. B* **341**, 19-31 (1993).
3. M. J. Canny, *Ann. Bot.* **75**, 343-357 (1995).
4. J. A. Milburn, *Ann. Bot.* **78**, 399-407 (1996).
5. M. T. Tyree, *J. Exp. Bot.* **48**, 1753-1765 (1997).
6. H. Van As, and T. J. Schaafsma, *Biophys. J.* **45**, 469-472 (1984).
7. J. E. A. Reinders, H. Van As, T. J. Schaafsma and D. W. Sheriff, *J. Exp. Bot.* **39**, 1211-1220 (1988).
8. J. E. A. Reinders, H. Van As, T. J. Schaafsma, P. A. de Jager and D. W. Sheriff, *J. Exp. Bot.* **39**, 1199-1210 (1988).
9. H. Van As, J. E. A. Reijnders, P. A. de Jager, P. A. C. M. van de Sanden and T. J. Schaafsma, *J. Exp. Bot.* **45**, 61-67 (1994).
10. T. J. Schaafsma, H. Van As, W. D. Palstra, J. E. Snaar and P. A. de Jager, *Magn. Reson. Imaging* **10**, 827-836 (1992).
11. P. T. Callaghan, C. D. Eccles and Y. Xia, *J. Phys. E: Sci. Instrum.* **21**, 820-822 (1988).
12. P. T. Callaghan, C. J. Clark and L. C. Forde, *Biophys. Chem.* **50**, 225-235 (1994).
13. F. W. Bentrup, *Bot. Acta* **109**, 177-179 (1996).
14. J. A. Chudek and G. Hunter, *Prog. Nucl. Magn. Reson. Spectrosc.* **1**, 43-62 (1997).
15. J. S. MacFall and H. Van As, In *Nuclear Magnetic Resonance in Plant Biology*. Y. Shachar-Hill and P. E. Pfeffer, editors. The American Society of Plant Physiologists. 33-76 (1996).
16. W. Köckenberger, J. M. Pope, Y. Xia, K. R. Jeffrey, E. Komor and P. T. Callaghan, *Planta* **201**, 53-63 (1997).
17. E. Kuchenbrod, E. Kahler, F. Thurmer, R. Deichmann, U. Zimmermann and A. Haase, *Magn. Reson. Imaging* **16**, 331-338 (1998).
18. M. Rokitta, A. D. Peuke, U. Zimmermann and A. Haase, *Protoplasma* **209**, 126-131 (1999).
19. T. W. J. Scheenen, D. van Dusschoten, P. A. de Jager and H. Van As, *J. Magn. Reson.* **142**, 207-215 (2000).
20. N. Ishida, M. Koizumi and H. Kano, *Ann. Bot.* **86**, 259-278 (2000).
21. H. T. Edzes, D. van Dusschoten and H. Van As, *Magn. Reson. Imaging* **16**, 185-196 (1998).
22. B. P. Hills and S. L. Duce, *Magn. Reson. Imaging* **8**, 321-332 (1990).
23. J. E. M. Snaar and H. Van As, *Biophys. J.* **63**, 1654-1658 (1992).

24. B. P. Hills and J. E. M. Snaar, *Mol. Phys.* **76**, 979-994(1992).
25. T. W. J. Scheenen, D. van Dusschoten, P. A. de Jager and H. Van As, *J. Exp. Bot.* **51**, 1751-1759 (2000).
26. D. R. Hoagland and D. I. Arnon, *Calif. Agric. Exp. Sta. Circ.* **347** (1950).
27. C. J. Rofe, J. Van Noort, P. J. Back and P. T. Callaghan, *J. Magn. Reson. B* **108**, 125-136 (1995).
28. J. Kärger and W. Heink, *J. Magn. Reson.* **51**, 1-7 (1983).
29. J. Hennig, A. Nauwerth and H. Friedburg, *Magn. Reson. Med.* **3**, 823-833 (1986).
30. J. E. M. Snaar and H. Van As, *J. Magn. Reson.* **99**, 139-148 (1992).
31. K. R. Brownstein and C. E. Tarr, *Phys. Rev. A* **19**, 2446-2453 (1979).
32. D. van Dusschoten, P. A. de Jager and H. Van As, *J. Magn. Reson. A* **116**, 22-28 (1995).
33. H. C. W. Donker, H. Van As, H. J. Snijder and H. T. Edzes, *Magn. Reson. Imaging* **15**, 113-121 (1997).
34. R. B. Bird, W. E. Stewart and E. N. Lightfoot, *Transport Phenomena*. New York: John Wiley & Sons (1960).
35. T. W. J. Scheenen, F. J. Vergeldt, C. W. Windt, P. A. de Jager and H. Van As, *J. Magn. Reson.* **151**, 94-100 (2001).
36. M. Rokitta, U. Zimmermann and A. Haase, *J. Magn. Reson.* **137**, 29-32 (1999).
37. E. Münch, *Die Stoffbewegungen in der Pflanze*. Germany, Jena: Fischer (1930).

6

Embolism induction and repair in xylem vessels of *Cucumis Sativus* L.

T.W.J. Scheenen, F.J. Vergeldt, A.M. Heemskerk, P.A. de Jager and H. Van As

The flow characteristics of the water in a virtual slice through a cucumber plant stem (*Cucumis Sativus* L.) have been studied with dynamic nuclear magnetic resonance imaging. Cooling the roots of the plant severely inhibited water uptake by the roots and increased the hydraulic resistance of the plant stem. This increase is (at least partially) due to the formation of embolisms in the xylem vessels of the plant. Four large vessels (diameters of two vessels 0.13 and 0.18 mm) in the depicted slice embolized and started to get refilled in the night after root cooling. The timescale of refilling ranged from five to fourteen hours for a three-mm part of the vessel. Extrapolating these times linearly would mean that vessel refilling in cucumber is a very lengthy process. Refilling occurred while neighboring vessels at a distance not more than 0.4 mm were under tension, transporting an equal amount of water before and a day after root cooling. Relative differences in volume flow in different vascular bundles suggest differences in xylem tension for different vascular bundles.

Introduction

The phenomenon of rapid wilting of various plants (for instance cucurbits) when the roots of these plants are cooled and the quick recovery after root temperature has returned to normal levels has been described already in 1860 (1). Berndt et al. (2) gave an overview of many papers on the subject through the years, concluding that the primary effect of root cooling was a reduced water uptake caused by a (quickly reversible) fall in radial conductance of the roots. A strong reduction in water uptake can cause the formation of xylem embolisms: due to a strongly negative water potential the water column in a xylem vessel is disrupted and the vessel fills with water vapor and air blocking further water transport. Embolisms in xylem vessels in roots and leaves, frozen while still attached to the plant, have been studied with cryo-scanning electron microscopy (2-9). These studies suggest that embolism formation and repair in the xylem is a continuous process occurring within one day and that partially filled vessels and water droplets in the lumen of vessels are proof of the refilling of the vessels. The mechanism behind this embolism repair is still unknown and some questions have been raised about the observations with the cryo-scanning electron microscopy technique itself (10).

Searching for a mechanism for embolism repair, one almost automatically enters the debate about the mechanism of xylem sap ascent in general. Recently, three reviews on this subject have been published (11-13) showing several different views on how water is transported from roots to leaves. The Cohesion-Tension theory (14) poses that xylem sap flows through continuous water columns in the xylem, driven by evaporation of water from the leaves, involving pressures in the xylem vessels more negative than the vapor pressure of water, making it vulnerable to cavitation. The water potential of the xylem vessels (the difference between the sap osmotic pressure and the xylem pressure) must be in balance with the water potential of adjoining tissues and cells in order for those tissues and cells not to lose water. If embolism formation and repair is a continuous process during the day, how can a vessel be refilled while tissue remains under tension? To answer this question Canny (4, 12) proposed the compensating pressure theory, which received severe criticism ((15-18) among others). Tyree et al. (17) concluded that none of the existing ideas could explain their results of embolism refilling in young

stems of Laurel. However, very recently it has been argued that xylem tension and embolism repair is not mutually exclusive (19), which would mean that the Cohesion-Tension theory still holds. In the refilling model, presented by Holbrook and Zwieniecki (19), a central role is played by the structure of the bordered pits and the surface properties of the xylem vessel walls, defining the contact angle of xylem sap with the vessel wall. It is the surface tension of the convex meniscus in the pit chambers between a refilling vessel and a vessel under tension that prevents xylem sap in the refilling vessel to connect with water from the vessel under tension (20). In this way the refilling vessel (with a slightly positive pressure to dissolve the gas) is hydraulically isolated from the vessel under tension until the embolized vessel is completely refilled. For both the driving force for refilling the embolized vessel by adjoining living cells and the details of re-establishing hydraulic continuity, new techniques and investigations are asked for (17, 19).

Several groups have shown that nuclear magnetic resonance imaging (NMRi or MRI) is suitable for plant studies at single vessel level (21-24). In this paper we present the first spatially resolved, non-invasive, *in vivo* measurements of embolism induction and refilling in a mature, intact cucumber plant (*Cucumis Sativus* L.) and its effect on flow behavior in individual xylem vessels. By using MRI methods as described by Scheenen et al. (25, 26) we studied changes in water transport in an individual plant in time as a function of environmental changes. We investigated whether xylem embolisms in the stem of the cucumber plant are involved in the phenomenon of rapid wilting and recovery during and after root cooling and are now able to answer a few pressing questions in the field of xylem vessel cavitation and restoration.

Methods

Plant material and NMR imaging setup

24-day-old commercially grown cucumberplants (*Cucumis sativus* L., cv Hurona), were transferred from rock wool to an aerated, half-Hoagland solution and grown for five weeks in a greenhouse at Wageningen University. A cylindrical jacket around the upper ten cm of the roots maintained horizontal root expansion within

4.5 cm diameter to facilitate insertion into the gradient probe of the instrumental setup. Flowers were pinched out and occasionally the bottom leaves of the plants were cut off to clear the lower 50 cm of the stems from leaves. Three days before the start of the measurements, one of these plants (~1.6 m tall) was moved from the greenhouse to the laboratory. A plastic mould was placed around the plant stem (~35 cm from the roots) and a radiofrequency (RF) coil (diameter 15 mm) was wound round the mould. The roots of the plant were put through the 4.5 cm cylindrical bore of a gradient probe (Doty Scientific Inc., Columbia, South Carolina, USA) and the plant with the RF coil and a support for capacitors inside the gradient probe was positioned in a 0.7 T electromagnet (Bruker, Karlsruhe, Germany) (Fig. 6.1).

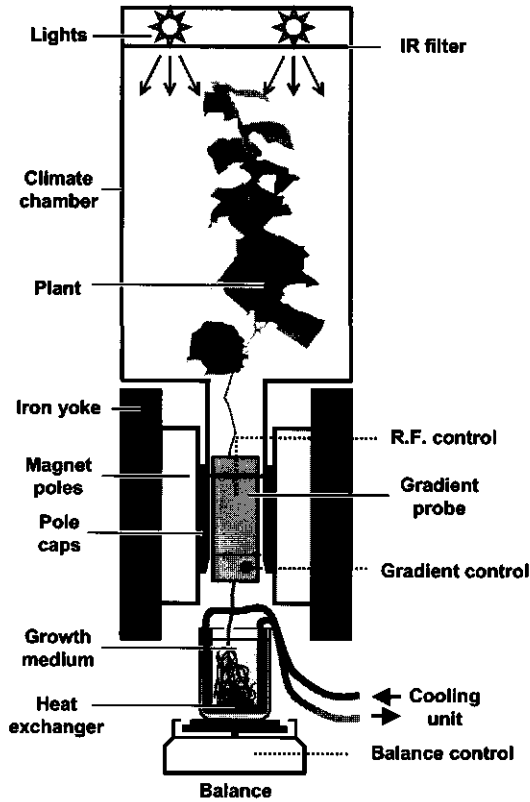


Figure 6.1: Overview of the plant in the instrumental setup. The dotted lines are connections to the RF amplifier and receiver, the gradient amplifiers and to a computer that monitors the weight of the container with growth medium.

The experiments were performed with an SMIS console (SMIS Ltd., Guildford, Surrey, UK). Water uptake by the roots of the plant was measured with a precision balance (LC3201D, Sartorius AG, Göttingen, Germany), sampling the average differential weight of the container with growth medium every 30 seconds. A heat exchanger in the container was able to cool and reheat the roots from 22°C to 3°C or vice versa in five minutes. The temperature in the climate chamber above the magnet was $25 \pm 2^\circ\text{C}$ during the photoperiod (from 6.00 a.m. to 9.00 p.m., relative humidity $65 \pm 5\%$, illumination about $2 \times 10^2 \mu\text{mol/m}^2\text{s}$ (PAR), depending on position of the leaves) and $22 \pm 2^\circ\text{C}$ at night.

NMR imaging pulse sequence and analysis

The diameter of the xylem vessels in the vascular bundles of a cucumber plant can range between 0.02 and 0.35 mm (27). With an in plane spatial resolution of $120 \times 120 \mu\text{m}$ the flow profile of water flowing in each volume-element (or pixel) of an image cannot be predicted, since a pixel of a transverse image of a cucumber plant stem can contain a few small vessels, one or two larger vessels or only a part of one of the larger vessels. Therefore the complete distribution of displacements in the direction of flow of the water within a certain labeling time (called a propagator) was acquired for every pixel. A pulsed field gradient turbo spin echo pulse sequence (26) was used to construct the propagators for every pixel within a physiologically relevant time. The following flow characteristics were extracted from the propagators for every pixel as described by Scheenen et al. (25): the total amount of water, the amount of stationary water, the amount of flowing water, the mean linear velocity of the flowing water, and the volume flow. On the basis of the flow characteristics per pixel several individual vessels could be discerned and the flow characteristics were recalculated for the summation of pixels containing individual vessels. In this way the flow characteristics of single pixels, individual xylem vessels and complete vascular bundles could be monitored in time.

Results

Overall reaction of the plant to the day/night cycle and root cooling

Figure 6.2 shows the water uptake and MRI flow results for the complete period of time that the plant was in the instrumental setup (cf. Fig. 6.1), starting at 20.00 hours on the first day. During the day (lights on) transpiration of the plant clearly elevated water uptake by the roots. The light intensity on the second day was low to allow the plant to recover from transportation and insertion in the setup. From the third day on illumination was kept constant at about $2 \times 10^2 \mu\text{mol/m}^2\text{s}$ (PAR), depending on the position of the leaves. From the third to sixth day the plant grew about 20 cm in length, which is visible in a steady increase in water uptake values of the plant in this time. The roots of the plant were cooled on day six from 12.20 h to 16.20 h. Water uptake decreased in this period to values below those measured at night. During root cooling, transpiration exceeded water uptake, resulting in a net

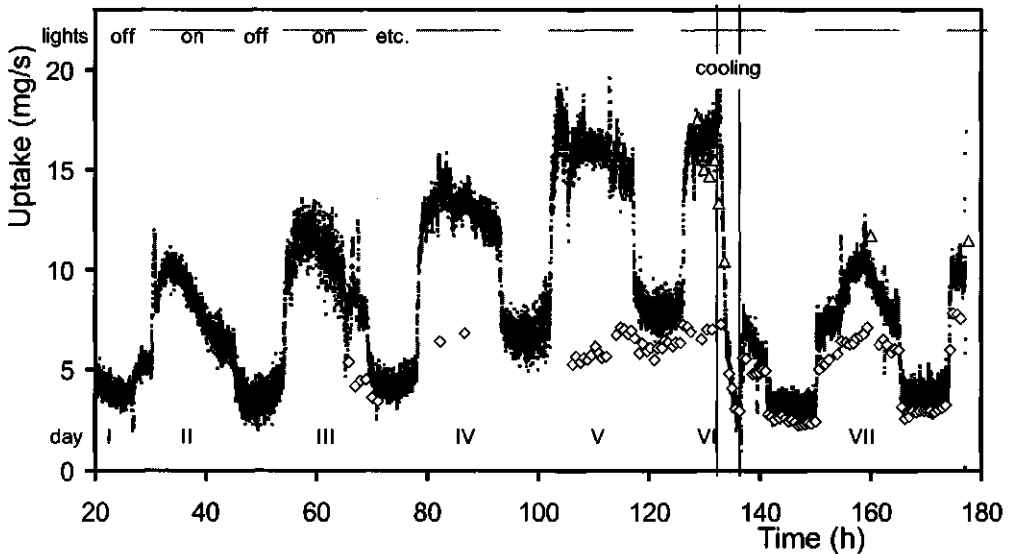


Figure 6.2: The water uptake by the roots of the cucumber plant in the instrumental setup. The black dots represent the values measured with the precision balance: every point is a moving average of 10 points, which is effectively five minutes. The open diamonds and triangles represent the total volume flow rate in the stem, calculated from respectively conventional NMR experiments (with linear motion-encoding gradient steps) and from experiments with non-linearly stepped gradients. The day/night cycle is indicated at the top of the graph and the period of root cooling on the fifth day is indicated with the two vertical lines. The roman numbers indicate the day number of the experiment.

water loss that caused severe wilting of all leaves and the top of the stem. After warming the roots to room temperature water uptake recovered only partially, but the plant recovered completely within 2.5 hours (except for the upper three small leaves that got damaged by the light in absence of transpiration). However, the decreased water uptake values in the days after root cooling reflected decreased transpiration levels. With unchanged conditions in the climate chamber this could point to an increased hydraulic resistance in the vascular system of the plant, if the decreased radial conductance of the roots quickly recovered after warming the roots (2).

NMR imaging of the plant stem

Results from four MRI measurements are shown in Fig. 6.3, together with light microscopic pictures of a thin, hand-cut slice of the stem through the imaging plane (made after the MRI study). The different tissues, indicated in the microscopic picture of a part of the plant stem (Fig. 6.3a) can be recognized in an image of the NMR spin-spin relaxation time T_2 (Fig. 6.3b), and an image of the water content of the slice (Fig. 6.3c). The NMR images in Fig. 6.3b+c are fitted results of a multi-echo imaging experiment (28). The large voids in the center of both images represent the empty pith cavity of the stem. The stele of the stem with large parenchymal cells contains four large and five smaller bicollateral vascular bundles, in which individual xylem vessels can be discerned. The large parenchymal cells have relatively long T_2 -values, whereas the vascular bundles, with smaller cells, have shorter T_2 -values. The individual xylem vessels can be seen as high intensity dots in the water content image and long T_2 -values inside the vascular bundles. The two circles on both sides of the stem in the NMR images are reference tubes filled with water.

Although only one small transverse slice of the stem (at 35 cm from the roots) with a thickness of 3 mm was visualized in the NMR images the cause of an increased hydraulic resistance could immediately be found. Figure 6.3c, d and e are three images representing the water content at different points in time revealing cavitating vessels due to root cooling. The red arrows in Fig. 6.3d indicate four vessels (two cavitating vessels at arrow 1) that were filled with water before root cooling ($t=130$ h, Fig. 6.3b), empty 3.7 hours after the period of root cooling ($t=140$ h, Fig. 6.3c) and

refilled again in the last night of the experiment ($t=170$ h, Fig. 6.3d). Figure 6.3f is an enlarged view (light microscopy) of the embolized vessel indicated with arrow II in Fig. 6.3d. The time course of cavitation and refilling of these vessels will be examined in detail later.

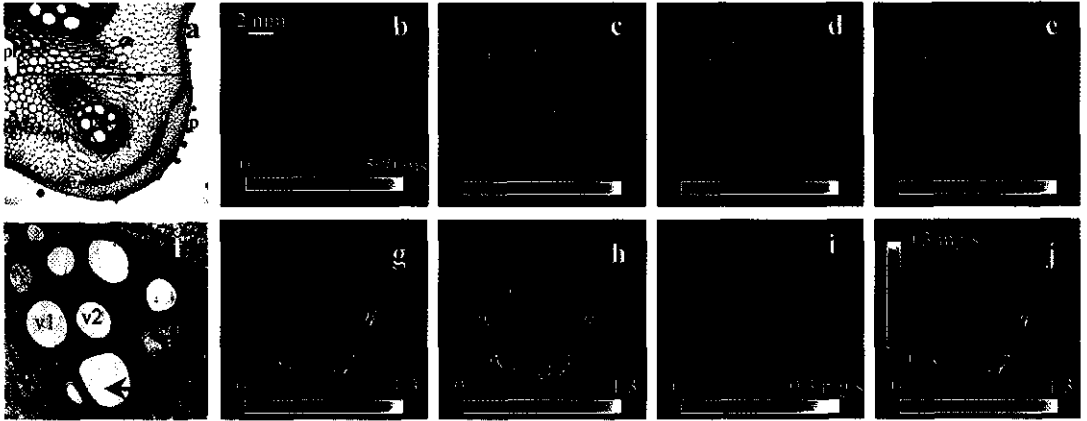


Figure 6.3: Cross-sections through the stem of the cucumber plant. a) Light microscopy of the bottom right vascular bundle. b) NMR image of the spin-spin relaxation time at $t=170$ hours, calculated from a multi-echo imaging experiment (28). c+d+e) NMR images of the water content of the slice at three different points in time: at $t=130$, 140 and 170 hours respectively. In d) the red arrows indicate cavitated vessels. The blue arrow indicates a vessel in which flow is restored. f) Enlarged view of the bottom right vascular bundle. The xylem vessel, indicated with the red arrow, is an embolizing vessel and is monitored in time in Fig. 6.4, together with vessels v1 and v2. g+h+i) NMR Images of some of the flow characteristics extracted from the propagators of every pixel: the total amount of water, the amount of stationary water and the volume flow respectively. The colored scales in g) and h) indicate an amount of water, relative to the reference tube ($=1$), the scale in i) indicates the volume flow per pixel in mg/s. j) An overlay image of the volume flow and the total amount of water. Experimental parameters: field of view 15.4 mm, resolution $120 \times 120 \times 3000 \mu\text{m}$, measurement time 21 min. Abbreviations in a): ep, epidermis; co, cortex; scl, sclerenchyma; ste, stele; vb, bicollateral vascular bundle; x, xylem; phl, phloem; pi, pith.

Figure 6.3g to j summarize the results of one flow-imaging experiment: the total amount of water per pixel (Fig. 6.3g), the amount of stationary water per pixel (Fig. 6.3h), the volume flow per pixel (Fig. 6.3i) and an overlay image of the volume flow and the total amount of water (Fig. 6.3j). In addition, images representing the amount of flowing water and the linear flow velocity of the flowing water are available (data not shown). It is clear from Fig. 6.3i that only a few large xylem vessels take care for the majority of the total volume flow through the slice. The

added volume flow of the pixels with flowing water represents the total volumetric water uptake through the slice, which should correspond with water uptake by the roots, measured with the precision balance. In Fig. 6.2 the values for the total volume flow, calculated from the MRI measurements, are indicated as open diamonds and open triangles. The open diamonds represent values from 'conventional' measurements, in which motion-encoding gradients are stepped equidistantly before Fourier Transformation into a propagator (26). These values were systematically too small for higher linear flow velocities. This problem was circumvented by stepping the motion-encoding gradients non-linearly, thereby probing higher linear velocities more accurately (Scheenen et al., in preparation). The calculated volume flow values of these measurements, indicated with the open triangles in Fig. 6.2, clearly fit the uptake values, measured with the balance.

The induction and refilling of an embolism

The flow characteristics in time of one of four embolisms that were visible in the measured slice are examined in detail here. The signal from five pixels, containing the embolizing vessel, indicated with the bottom red arrow (arrow II) in Fig. 6.3d and 6.3f, was added and re-analyzed as described by Scheenen et al (25). The signal from an area of nine pixels, adjoining the five-pixel area that contained the embolizing vessel, was also analyzed separately (vessels v1 and v2 from Fig. 6.3f). In Fig. 6.4 the flow characteristics are presented for both areas from the night before root cooling until the end of the experiment. The formation of an embolism is clearly visible: in the center of the period of root cooling the volume flow (squares in Fig. 6.4a) and the amount of flowing water (triangles in Fig. 6.4c) abruptly fell to zero. The total amount of water in the area with the embolizing vessel dropped to $10.4 \times 10^{-2} \text{ mm}^3$ and remained at this value for twelve hours until about 4.30 a.m. that night. Then, it took 13 hours for the selected area in the slice to be refilled with $7.7 \times 10^{-2} \text{ mm}^3$ water ($= 0.64 \times 10^{-2} \text{ mm}^3/\text{h}$): the cross-sectional area of flow of the embolized vessel was $7.7 \times 10^{-2} / 3.0$ (slice thickness) $= 2.6 \times 10^{-2} \text{ mm}^2$. The cross-sectional area of flow, calculated from the light-microscopic picture was $3.0 \times 10^{-2} \text{ mm}^2$. Water transport in this vessel was not restored within the total experimental time.

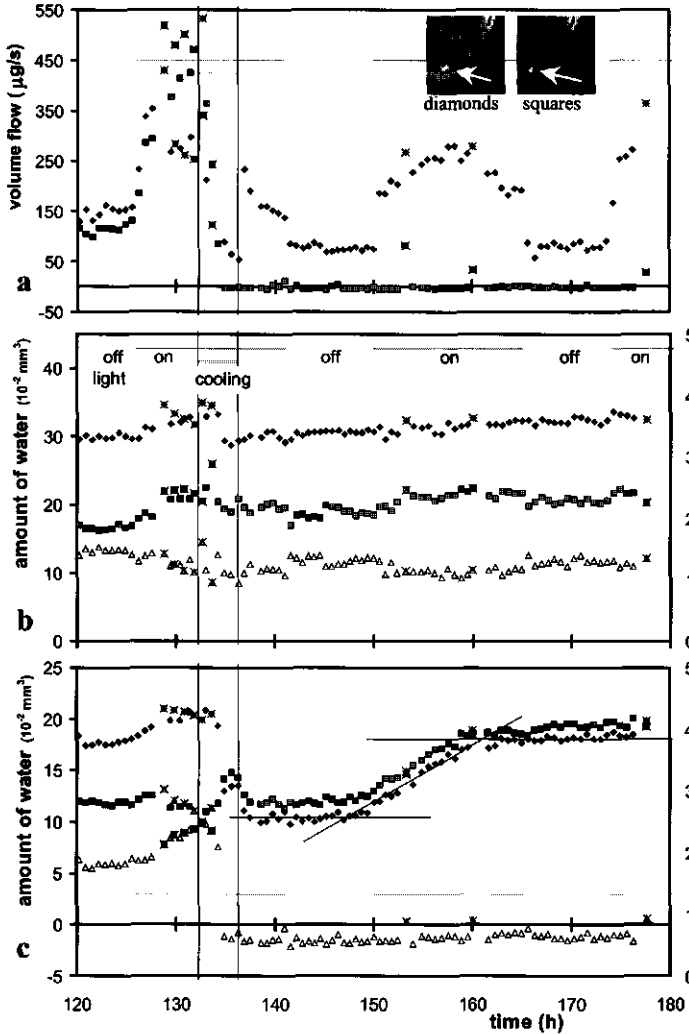


Figure 6.4: The flow characteristics of two small neighboring areas, of which one contains an embolizing vessel (area of five pixels) and the other contains at least one vessel unaffected by root cooling (area of nine pixels). The areas are indicated as highlighted pixels in two enlarged parts of the image in the inset of Fig. 6.4a. a) Volume flow of both vessels in time: the squares represent the embolizing vessel, the diamonds indicate the unaffected vessel. b) The total amount of water (closed diamonds), the amount of stationary water (squares) and the amount of flowing water (triangles) of the unaffected vessel. c) The total amount of water (closed diamonds), the amount of stationary water (squares) and the amount of flowing water (triangles) of the embolizing vessel. The second y-axis on the right side of graphs b and c represent the averaged water amounts for one pixel in the selected area. The crosses through some specific points indicate the results obtained by the non-linearly motion-encoded measurements (cf. the triangles in Fig. 6.2).

Surprisingly, the flow characteristics of the area of nine pixels immediately adjoining the refilling vessel (with vessels v1 and v2, Fig. 6.3f) were not affected by the formation and refilling of the embolism. According to the Hagen-Poiseuille law for laminar flow (29) the volume flow through a circular tube or vessel is related to the vessel radius to the power of four. This relation clarifies why the volume flow of the unaffected nine-pixel area with two smaller vessels v1 and v2 was smaller than the volume flow of the embolizing vessel (Fig. 6.4a), whereas the amount of flowing water of v1 and v2 was larger (compare Fig. 6.4b with Fig. 6.4c). The cross-sectional area of flow for v1 and v2, calculated from the light-microscopic picture was $2.2 \times 10^{-2} \text{ mm}^2$ and $1.4 \times 10^{-2} \text{ mm}^2$. Although the vessels are not perfectly circular, the Hagen-Poiseuille law can be used to estimate the xylem pressure difference ΔP_x over the vessels, which was assumed to be equal for v1, v2 and the embolizing vessel. ΔP_x of the embolizing vessel before root cooling, needed to drive 0.49 mg water per second through a 0.2 mm diameter vessel (estimated from a cross-sectional area of flow of $3.0 \times 10^{-2} \text{ mm}^2$), is 14 Pa/mm. Table 6.1 summarizes the kinetics of refilling for all vessels indicated with the red arrows in Fig. 6.3d. The flow characteristics of the embolizing vessel in Fig. 6.4, which were calculated from the alternative flow-measurements (triangles in Fig. 6.2), corresponded with those calculated from the 'conventional' flow-measurements (squares in Fig. 6.2), so the values from both measurements could be considered here (cf the ordinary symbols in Fig. 6.4 with the symbols in which a cross is drawn).

Table 6.1: Details of refilling of four xylem vessels that embolized during root cooling.

Vessel number Fig. 6.3d	Dia- meter (mm)	Cross- sectional area (mm^2)	Volume flow* (mg/s)	Start of refilling [†] (hours)	Refilling time (hours)	Refilling speed (mm^3/h)	ΔP_x (Pa/mm)
I [‡]	-	5.1×10^{-2}	0.36 ± 0.06	4.00 a.m.	14	1.1×10^{-2}	-
II	0.18	2.6×10^{-2}	0.49 ± 0.02	4.30 a.m.	13	0.64×10^{-2}	14
III	0.13	1.3×10^{-2}	0.17 ± 0.05	0.00 a.m.	5	0.75×10^{-2}	11

*Mean volume flow \pm standard deviation in the hours before root cooling

[†]Night after root cooling

[‡]Data in this row originates from two embolized vessels

Restoration of flow in a xylem vessel

Apart from embolizing vessels, also a vessel that restored flow could be found in the slice (indicated with the blue arrow in Fig. 6.3d). Figure 6.5 reveals the flow characteristics of a selected area containing this vessel (5 pixels), together with those of a neighboring area (six pixels), transporting water throughout the complete experiment. Even around $t=67$ hours (day III) no water was transported in the selected area (data not shown). At $t=152$ hours (8.00 a.m. at day VII, two hours after the lights had been turned on, indicated with a vertical line in Fig. 6.5a + c) water transport in the vessel started and increased to 0.2 mg/s in six hours. The total amount of water in the area with the restoring vessel remains constant throughout the experiment: before $t=152$ hours all water was stationary; when the vessel starts transporting water about one-third of the water starts flowing (Fig. 6.5c). The cross-sectional area of flow of this vessel was $8.2 \times 10^{-2} / 3.0 = 2.7 \times 10^{-2} \text{ mm}^2$, calculated from the NMR measurements, and $3.0 \times 10^{-2} \text{ mm}^2$, calculated from Fig. 6.3f, corresponding with a circular vessel diameter of 0.2 mm. For a volume flow of 0.2 mg/s a ΔP_x of 6 Pa/mm is needed (again, assuming a circular vessel geometry). The amount of stationary and flowing water of the area next to the restoring vessel (at a distance of 0.5 to 0.6 mm) were not influenced by the restoration of flow or root cooling (Fig. 6.5b). However, the volume flow of this area on the day after root cooling was larger compared to the transpiring period before root cooling and the hours just after root cooling on day VI. ΔP_x over one unit length of the xylem vessel in this area was larger on day VII than on the day of root cooling (day VI).

Discussion

The development of the overall water uptake by the cucumber plant in the instrumental setup before root cooling indicates that the plant is healthy and growing (Fig. 6.2). The difference in water uptake between just before and one day after root cooling suggests a reduction in hydraulic conductivity of the xylem, as the decrease in radial conductance of the roots (caused by root cooling) is rapidly reversed on rewarming (2). The cause of the reduction in hydraulic conductivity is the formation of embolisms, blocking water transport. In the 3-mm thick slice that

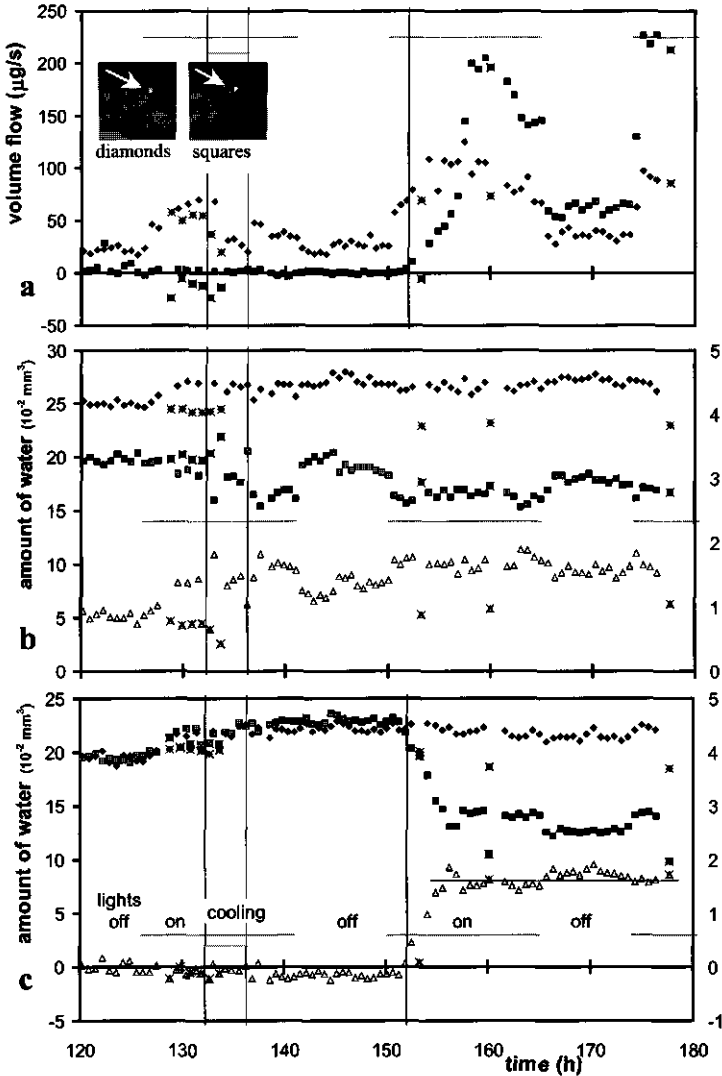


Figure 6.5: The flow characteristics of two small neighboring areas, of which one contains a vessel in which flow is restored (area of five pixels) and the other contains at least one vessel, unaffected by root cooling (area of six pixels). As in Fig. 6.4, the areas are indicated as highlighted pixels in two enlarged parts of the image in the inset of Fig. 6.5a; a) represents the volume flow of both vessels in time: the squares represent the restoring vessel, the diamonds indicate the unaffected vessel. b) and c) represent the total amount of water (closed diamonds), the amount of stationary water (squares) and the amount of flowing water (triangles) of the unaffected vessel and the restoring vessel, respectively. Again, the second y-axis on the right side of graphs b and c represent the averaged water amounts of one pixel in the selected area and the crosses through points indicate deviant measurements (cf. the triangles in Fig. 6.2).

was studied here, four embolizing vessels were found (Fig. 6.3). How many other vessels had been embolized at different positions in the stem (or in the roots) is unknown. However, the difference in water uptake between the hours before root cooling and one day after root cooling (> 7 mg/s) could not be caused by the loss of transport capacity in the four embolizing vessels in the slice alone (total volume flow of these vessels before root cooling 1.0 mg/s, cf. Table 6.1). Where some vessels were not affected by root cooling (Fig. 6.4b) and others even showed an increase in volume flow after root cooling (Fig. 6.5a) the total volume flow decreased drastically due to vessels in which water transport was completely stopped or reduced, probably because of embolisms outside the slice, but inside the conduits concerned.

Investigating the temporal dynamics of embolizing vessels in more detail in Fig. 6.4 revealed a few interesting phenomena. Firstly, large embolized xylem vessels in the stem of the plant were refilled, and the time scale of refilling is long. It took five, thirteen and fourteen hours to refill a length of only three mm (the observed slice) of the embolized vessels. The speed of refilling was in the order of 0.6×10^{-2} mm³/h. With comparable refilling speeds, the smaller embolized vessel refilled faster (in the observed slice). Extrapolated linearly it would take 17 to 47 hours for every cm of a vessel to be refilled with water. Although it is not possible to resolve whether the speed of refilling is constant over a complete vessel from the presented data, it is clear that refilling of an embolized vessel in the stem of a cucumber plant is a slow process, contrary to what has been concluded for petioles of sunflower (3, 4), the primary root of squash plants (2) or young stems of laurel (17). This is a plausible reason why we did not observe restoration of flow in embolized vessels in our experiment: the time scale of complete refilling is simply too long. Vessels, embolized because of root cooling on day VI, were not completely refilled by the end of the experiment. The vessel in which flow was restored on day VII had not been transporting water for at least four days. An embolism below or above the slice in this conduit might have been induced while moving the plant from the greenhouse to the lab or in the first days in the setup.

Secondly, refilling occurred while nearby tissue and vessels were under tension. The area adjoining an embolizing vessel at a distance not more than 0.4 mm was

unaffected by embolism formation and refilling of the neighboring vessel (Fig. 6.4b). Therefore, the water in the refilling vessel must be completely isolated from water in surrounding cells or vessels, as was hypothesized and investigated by Holbrook and Zwieniecki (19, 20).

The pressure difference per unit length of a xylem vessel (ΔP_x , the driving force for flow) is in the order of 10 Pa/mm (assuming cylindrical vessel geometry) and not equal for all vascular bundles in the slice. Water close to the walls in vessels is effectively stationary in a laminar flow profile and therefore difficult to distinguish from surrounding stationary water in accompanying cells. Therefore, the cross-sectional area of flow, calculated from the NMR measurements, was systematically smaller than the cross-sectional area of flow, calculated from the light-microscopic pictures. The volume flow of vessels v1 and v2 (Fig. 6.3f) was constant in the hours with lights on before root cooling on day VI, throughout day VII and VIII (Fig. 6.4a). However, the volume flow of vessels near the vessel in which flow was restored was around 50% larger on day VII and VIII than on day VI before root cooling (lights on periods, Fig. 6.5a). These relative differences in volume flow (and therefore also in ΔP_x) suggest differences in xylem tension between different vascular bundles in a slice.

If the water in a refilling vessel needs to be hydraulically isolated (with bordered pits (19, 20)) from surrounding cells or tissues under tension, then what is the source of the incoming water and what is the driving force for water to enter the embolized vessel? Perhaps a combination of MRI with a xylem or tissue pressure probe and a detailed study of vessel and air bubble anatomy (especially in the longitudinal direction) can give the answer to this emerged question.

Acknowledgement

This research was supported by the Dutch Technology Foundation STW, applied science division of NWO (project WBI 3493). The authors thank Ir. Jaap Nijse from the laboratory of plant physiology for preparing the light microscopy pictures.

References

1. J. Sachs, *Botanische Zeitung* **18**, 121-126 (1860).
2. M. L. Berndt, M. E. McCully and M. J. Canny, *Plant Biol.* **1**, 506-515 (1999).
3. M. J. Canny, *Am. J. Bot.* **84**, 1217-1222 (1997).
4. M. J. Canny, *Am. J. Bot.* **84**, 1223-1230 (1997).
5. C. Buchard, M. McCully and M. Canny, *Agronomie* **19**, 97-106 (1999).
6. M. E. McCully, C. X. Huang and L. E. C. Ling, *New Phytol.* **138**, 327-342 (1998).
7. M. E. McCully, *Plant Physiol.* **119**, 1001-1008 (1999).
8. J. S. Pate and M. J. Canny, *New Phytol.* **141**, 33-43 (1999).
9. M. W. Shane and M. E. McCully, *Aust. J. Plant Physiol.* **26**, 107-114 (1999).
10. H. Cochard, C. Bodet, T. Arneglio and P. Cruziat, *Plant Physiol.* **124**, 1191-1202 (2000).
11. J. A. Milburn, *Ann. Bot.* **78**, 399-407 (1996).
12. M. J. Canny, *Ann. Bot.* **75**, 343-357 (1995).
13. M. T. Tyree, *J. Exp. Bot.* **48**, 1753-1765 (1997).
14. H. H. Dixon and J. Joly, *Philos. Trans. R. Soc. Lond. Ser. B-Biol. Sci.* **186**, 563-576 (1894).
15. J. P. Comstock, *Am. J. Bot.* **86**, 1077-1081 (1999).
16. V. Stiller and J. S. Sperry, *Am. J. Bot.* **86**, 1082-1086 (1999).
17. M. T. Tyree, S. Salleo, A. Nardini, M. A. o Gullo and R. Mosca, *Plant Physiol.* **120**, 11-21 (1999).
18. M. T. Tyree, *Plant Biol.* **1**, 598-601 (1999).
19. N. M. Holbrook and M. A. Zwieniecki, *Plant Physiol.* **120**, 7-10 (1999).
20. M. A. Zwieniecki and N. M. Holbrook, *Plant Physiol.* **123**, 1015-1020 (2000).
21. N. M. Holbrook, E. T. Ahrens, M. J. Burns and M. A. Zwieniecki, *Plant Physiol.* **126**, 27-31 (2001).
22. J. S. MacFall and H. Van As, in *Nuclear Magnetic Resonance in Plant Biology*, eds. Y. Shachar-Hill and P. E. Pfeffer, (The American Society of Plant Physiologists), pp. 33-76 (1996).
23. M. Rokitta, A. D. Peuke, U. Zimmermann and A. Haase, *Protoplasma* **209**, 126-131 (1999).
24. W. Köckenberger, J. M. Pope, Y. Xia, K. R. Jeffrey, E. Komor and P. T. Callaghan, *Planta* **201**, 53-63 (1997).
25. T. W. J. Scheenen, D. van Dusschoten, P. A. de Jager and H. Van As, *J. Exp. Bot.* **51**, 1751-1759 (2000).
26. T. W. J. Scheenen, D. van Dusschoten, P. A. de Jager and H. Van As, *J. Magn. Reson.* **142**, 207-215 (2000).
27. J. E. A. Reinders, *Thesis Molecular Physics* (Wageningen University, Wageningen) (1987).
28. H. T. Edzes, D. van Dusschoten and H. Van As, *Magn. Reson. Imaging* **16**, 185-196 (1998).
29. R. B. Bird, W. E. Stewart and E. N. Lightfoot, *Transport Phenomena* (John Wiley & Sons, New York) (1960).

7

Quantitative imaging of plant water status and transport with Nuclear Magnetic Resonance: a strategy.

T.W.J. Scheenen, P.A. de Jager, F.J. Vergeldt and H. Van As

The possibilities of quantitative NMR imaging of plants at a low magnetic field strength are discussed. An advantage of a low magnetic field strength for plant studies is the absence of susceptibility related image artifacts. The electromagnet used in the current studies has an open setup, which facilitates vertical positioning of the plant. The inherent low signal to noise ratio is partly compensated by the use of a solenoid radiofrequency coil and the possibility to record many signal-containing spin echoes. The multiple spin echoes can be used for quantitative T_2 imaging or for decreasing the acquisition time of one image with turbo spin echo imaging, enabling quantitative displacement imaging with a physiologically relevant time resolution. Due to the unpredictable flow profile in a single pixel it is necessary to record the complete distribution of displacements for every pixel of an image. Both fast flow and diffusion can be imaged quantitatively by sampling q -space with non-equidistant steps. Possible problems when quantifying flow are discussed. Quantitative T_2 imaging and displacement imaging relate more than one parameter to every pixel of an image, which can take away the need for a high spatial resolution.

Introduction

The debate on the mechanisms behind water transport in plants is livelier than ever, as a result of the introduction of the xylem pressure probe and cryo-scanning electron microscopy into the scientific area of plant water relations. Questions have been raised around the century-old Cohesion Tension theory (1), which poses that xylem sap flows through continuous water columns from roots to shoot, driven by evaporation of water from the leaves. Obviously, with trees exceeding heights of ten meters this would leave water in the xylem at pressures more negative than the vapor pressure of water. Other forces, like root pressure and capillary forces, are also involved in long distance water transport. Although Nuclear Magnetic Resonance imaging (NMRi or MRI) has been applied to plants or plant tissue in many studies (for an overview, see Ishida *et al.*(2)), it is a relatively new technique in plant physiology. Köckenberger reviewed MRI for plant cell metabolism studies together with an introduction in the fundamental principles of NMR (3). Only recently MRI has been used as a tool to unravel water transport and its mechanisms in large intact plants by quantifying flow characteristics and relaxation times for every pixel in an NMR image (4).

Why is MRI in plant science still far from being a routine tool? Some reasons could be the high costs of NMRi equipment, the difficult theoretical fundamentals on which the technique is based, the horizontal orientation of standard imaging setups, the limited accessibility (for large plants) of the magnetic fields' iso-center of most setups, and the specific requirements which have to be met when measuring plants. In this paper we would like to address some of these issues and set out a strategy on how to deal with plant-specific problems in quantitative NMRi of plants at relatively low magnetic field strengths.

Magnetic field strength and signal-to-noise ratio

A high signal-to-noise ratio (SNR) is crucial in an NMR experiment for a high accuracy of the calculated or fitted parameters and a high resolution in space and time. The SNR of the NMR signal, immediately after excitation, is proportional to the

magnetic field strength B_0 to the power of 7/4 ($\text{SNR} \sim B_0^{7/4}$) (5). This has been the main reason for the development of high field imaging spectrometers using superconducting magnets. However, plants have many air-filled intercellular spaces in their tissues. Since air and water have different magnetic susceptibilities, the density of the magnetic field lines in air is different from that in water, producing magnetic field inhomogeneities around every air-water interface. The strength of these field inhomogeneities is linearly proportional to B_0 and cause artifacts in NMR images (6). Apart from positional displacements of signal intensity in the image, the intensity is also reduced, and image resolution is degraded because of self-diffusion or flow of protons within the random field inhomogeneities (7). Loss of image intensity can already be dramatic (50% and more) in the first echo of an NMR experiment (8). Moreover, if multiple echoes are recorded and the signal is not only lost because of transverse relaxation (characterized by the spin-spin relaxation time T_2), the presence of field inhomogeneities severely hampers quantitative T_2 and proton density imaging. Additional signal loss affects the NMR signal decay in an echo train for every pixel in an image, to which an exponential decay curve is fitted (with decay time T_2 and the proton density as the initial signal amplitude, (9)). In other experiments in which the magnetization needs to evolve for some time (e.g. because of flow-encoding) (a part of) the signal can simply not be recalled if it is lost due to the field inhomogeneities caused by susceptibility differences.

At relatively low magnetic field strengths the field inhomogeneities in plants, due to susceptibility differences, are small compared to the imaging gradients: displacements of self-diffusing protons in these field inhomogeneities on the timescale of a single scan are too little to cause additional attenuation of the signal. In quantitative T_2 and proton density studies at $B_0 = 0.47$ T Edzes *et al.* (9) found T_2 -values in the stem of Giant Hogweed approaching the value of pure water (>1.5 s). With such long T_2 -values many spin-echoes can be recorded (up to 1000 in a cherry tomato (9)), increasing the total SNR. The optimal field strength, obtaining the highest SNR with minor susceptibility artifacts, depends on the size, the shape, the concentration and distribution of air spaces in the sample.

An advantage of the 0.7 T low-field electromagnet (Bruker, Karlsruhe, Germany), of which some results are presented here, is its easy accessibility. The magnet is stripped from its shim coils, in the iso-center is only a custom-made gradient probe with an open 4.5-cm cylindrical bore (Doty Scientific Inc., Columbia, South Carolina, USA) and a small lock to stabilize the main magnetic field. Plants can quite easily be put into the gradient probe and the roots are placed inside a vessel containing the medium, placed on top of a precision balance (LC3201, Sartorius AG, Göttingen, Germany) to measure the water uptake (4). The field lines of B_0 are in the horizontal direction, which enables the use of solenoid radiofrequency (rf) coils around plant stems (perpendicular to the direction of B_0) to excite and detect the NMR signal. The performance of solenoid coils exceeds the performance of e.g. saddle coils (often used in superconducting magnets) by a factor of 3 (5), which is an advantage in coping with the low SNR at low B_0 . Apart from the coil geometry, also the coil diameter d influences the SNR ($\text{SNR} \sim 1/d$) (5). Homemade openable moulds around the plant stem give support when a new solenoid is wound around a stem to keep d minimal for every new plant. The choice of not using a Faraday cage in the setup forces us to take special care in grounding the plants and shielding the rf coil: grounding connections from a copper tape around the plant stem and of the coil shielding are as short as possible. The specialized field of using cooled (superconducting) coils and pre-amplifiers to increase the SNR is an aspect that is not dealt with here (10), although the accessibility of the electromagnet would certainly allow applying them.

Imaging water transport in plants: unpredictable flow profiles

Although the flow profile of water in a xylem vessel of a plant is generally assumed to be laminar, the flow profile of flowing water in one pixel of an image of a plant stem or root depends on the size and position of the pixel relative to the xylem vessel. If the pixel is large compared to the vessel diameter, multiple vessels are captured in one pixel and the flow profile of that pixel is the sum of several individual laminar flow profiles. If the pixel is small compared to the vessel diameter it can contain only a part of a laminar flow profile. In both cases, the flow profile of the flowing water in the pixel is unknown. With dynamic NMR microscopy (11) one

can obtain the complete distribution of proton displacements within a certain observation time for every pixel, which can be translated into the flow profile of the water in that pixel. An additional complication is the fact that the distribution of proton displacements in a vessel or tube varies with the observation time because of radial diffusion of protons over the flow profile (12, 13).

In a dynamic NMR imaging experiment the displacement of protons is probed with two pulsed magnetic field gradients (PFG) with amplitude g , duration δ and spacing Δ (cf Fig. 7.1). The modulation of the amplitude and phase of the complex NMR signal as a function of PFG amplitude (also known as q -space with $q = \gamma \delta g / 2\pi$, γ being the proton gyromagnetic ratio) can be Fourier Transformed into the displacement distribution of the protons within Δ : a so-called propagator $P(R, \Delta)$ (11, 14). Measuring propagators for every pixel in an image in plant tissue has been done in seedlings (15, 16), although the time resolution of these experiments was low (4.5 hours). Since only a single echo was recorded in every scan it took n scans to record an image with n^2 pixels for every step (or image) in q -space.

The possibility to record many spin echoes in an echo train to characterize relaxation times and proton density, as mentioned previously, can now be used in a different way. Propagators can be measured with a much higher time resolution if the two motion-encoding PFGs are combined with turbo spin echo (TSE) imaging, also called Rapid Acquisition Relaxation Enhanced imaging (RARE) (17). The measurement time of a single image can be shortened by a factor equal to the amount of measured echoes. The signal in this TSE image can be modulated with the two PFGs in a spin echo (SE) sequence (18) or a stimulated echo (STE) sequence (19) (Fig. 7.1). With the PFG spin echo TSE sequence, propagators in large plants have been measured (4) and quantified by extracting the following flow parameters from it (20): the total amount of water, the amount of stationary water, the amount of flowing water, the linear flow velocity of the flowing water and the volume flow. The propagator intensity of nine pixels in a reference tube filled with water has been used for calibration.

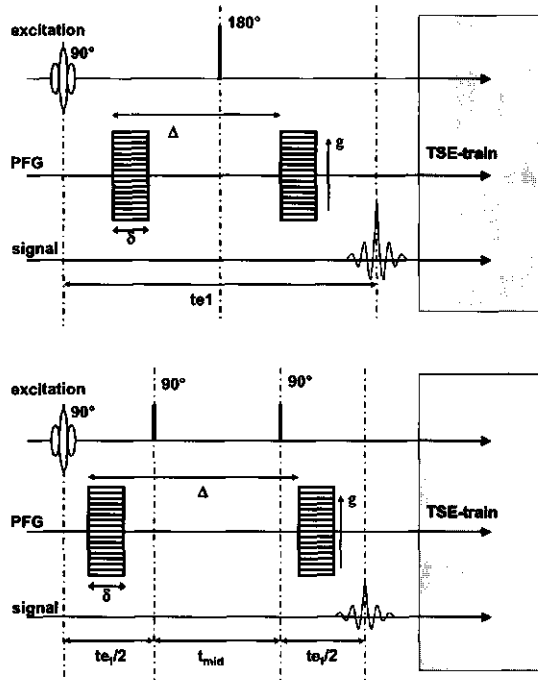


Figure 7.1: The PFG spin echo TSE pulse sequence (top) and the PFG stimulated echo TSE pulse sequence (bottom).

**Measuring water displacements in plants:
slow flow and diffusion, fast flow and diffusion**

The vast majority of water in a plant is stationary; water in xylem and phloem tissue can flow at different velocities, depending on vessel size and pressure difference over the vessels. The root mean square displacement σ of stationary, self-diffusing protons, observed by NMR, is proportional to the square root of the corrected labeling time $\Delta - \delta/3$ and the diffusion constant D of the observed protons:

$$\sigma = \sqrt{2D(\Delta - \delta/3)} \quad [1],$$

whereas the mean displacement \bar{r} of flowing protons is proportional to Δ itself:

$$\bar{r} = \bar{v}\Delta \quad [2],$$

in which \bar{v} is the mean flow velocity of the flowing protons. The labeling time between the two PFGs has to be long (in the order of 150 ms) to discriminate

between slow flow ($50 \mu\text{m/s}$) and diffusion (19). The choice between using a SE or STE version of the pulse sequence (Fig. 7.1) depends on the time from excitation to the first echo (containing Δ), the spin-lattice relaxation time T_1 and spin-spin relaxation time T_2 of the observed protons. In a SE experiment the NMR signal is in the xy -plane throughout the time from excitation to detection, where it decays according to the T_2 . In a STE experiment, the signal is stored along the z -axis during most of the labeling time, where it decays according to the spin-lattice relaxation time, which is longer (often substantially) than T_2 . The maximum amplitude of the stimulated echo is intrinsically half the initial signal amplitude, but can still be larger than the spin echo amplitude at the same time after excitation. Propagators of slowly flowing water (maximum linear velocity 0.67 mm/s) in a cut-off pedicel of a tomato have been measured with the stimulated echo version of the PFG TSE pulse sequence (19). If linear flow velocities are high, short labeling times can be used for which the spin echo version of the sequence is more suitable.

At high flow rates other issues are of importance. In larger plants the linear flow velocities of the xylem sap can reach velocities of several cm/s , which can cause a dynamic range problem in the propagator. This is illustrated in Fig. 7.2 with four simulated propagators of a certain amount of stationary water and an equal amount of flowing water. Stationary self-diffusing water has a Gaussian shape at zero displacement. The water, flowing with a laminar flow profile, has a boxcar shape with rounded edges from zero to the maximum displacement within the observation time. All shown propagators are the real part of a complex signal: the imaginary part of the signal has zero intensity (data not shown). The maximum velocity of the flowing water, which is twice the mean velocity for laminar flow, increases from (a) to (d). With all displacements R occurring between zero and the maximum displacement within the labeling time Δ between the two PFGs, the boxcar shape stretches out over the displacement axis. If the maximum displacement exceeds the edge of the axis (defined by the smallest q -step) the propagator intensity emerges at negative displacements (aliasing, Fig. 7.2c). With even higher displacements the boxcar stretches out all over the displacement axis (Fig. 7.2d). Note in this figure that the maximum displacement of $400 \mu\text{m}$ is visible at $80 \mu\text{m}$. The simulated propagators do not contain any noise, in contrast with experimental

data, in which the noise can overwhelm a broad distribution of displacements as in Fig. 7.2c and 7.2d.

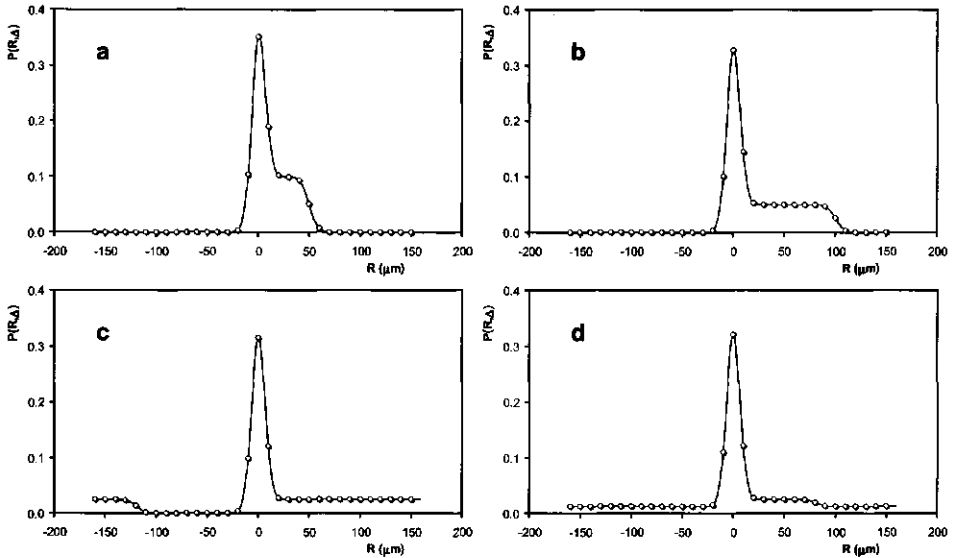


Figure 7.2: Simulated propagators of two water fractions: 50% stationary water and 50% water flowing with a laminar flow profile. In (a) to (d) the simulated mean linear flow velocities in the laminar profile are 2.5, 5.0, 10.0, and 20.0 mm/s, respectively. Radial diffusion over the parabolic flow profile is not accounted for, the diffusion constant in the direction of the PFGs is set to $2.2 \times 10^{-9} \text{ m}^2/\text{s}$, Δ is 10 ms. In (a) and (b) the rectangular displacement profile of the flowing water stretches over the displacement axis to 50 and 100 μm . In (c) the displacement profile exceeds the positive part of the axis and emerges at negative displacements (the signal is aliased). In (d) the displacement profile stretches all over the axis, which effectively gives the propagator an offset.

A solution for this dynamic range problem (within a nearly equal total measurement time) is the use of an alternative way of sampling the signal as a function of q-steps, proposed in non-imaging studies (21). In Fig. 7.3a the real and imaginary part of the signal as a function of q-steps associated with the simulated propagator in Fig. 7.2d is plotted twice with a solid line. The imaginary part of the signal originates from flowing water only, whereas the real part of the signal is composed of signals from stationary as well as flowing water. The top signal in Fig. 7.3a is sampled with equidistant q-steps, the bottom signal is sampled with non-equidistant steps that gradually increase in size at larger q-values. From Fig. 7.3a it is evident that the step size of the linear sampling is too large to probe the signal correctly. If the complete signal would be sampled linearly with the smallest step, 128 steps

would be needed to probe the shown signal, instead of the 32 or 36 steps in the top and bottom sampling, increasing the measurement time with a factor of approximately 4. Before Fourier transformation (FT) into the propagator, the non-linearly sampled data must be interpolated because this mathematical operation needs equidistant data. The range of the displacement axis of the corresponding propagators in Fig. 7.3b and 7.3c (after FT) is inversely proportional to the smallest q-step.

After FT of the signal, sampled with 32 equidistant steps, the propagator in Fig. 7.3c (open circles) has the offset-value as shown in Fig. 7.2d, including some truncation artifacts because the signal in Fig. 7.3a was not sampled completely to zero intensity at the largest q-values. The truncation artifacts can be prevented by sampling the signal using even larger q-values, which takes time, or they can be removed by filtering or extrapolating the signal to larger q-values. The displacement axis of the propagator after FT of the signal, sampled with 36 non-equidistant steps and interpolated from 36 to 128 steps, covers a four times larger range (from -600 to +600 μm). In this propagator (Fig. 7.3b) the boxcar shape representing the laminar flow profile with maximum displacement of 400 μm is evident.

The signal $S(q)$ can be filtered before FT to increase the SNR of the flowing part of the signal and to remove truncation artifacts. The filter in Fig. 7.3a has a transmission of 1 in the center of q-space, where the signal intensity from flowing water is high. At larger q-values the transmission is zero. The signal of stationary water is severely affected by the filter, resulting in broadening of the stationary water peak in the propagator (the asterisks in Fig. 7.3b). Because the maximum displacement of the flowing water is large, the flowing part of the propagator is hardly affected by the filter.

The experimental data are shown in the images in Fig. 7.4a and the propagators in Fig. 7.4b. The images represent the calculated flow characteristics of a non-linearly sampled spin echo PFG TSE experiment of a transverse slice through the stem of a 1.5-m tall intact cucumber plant in the 0.7 T electromagnet setup. The flowing parts

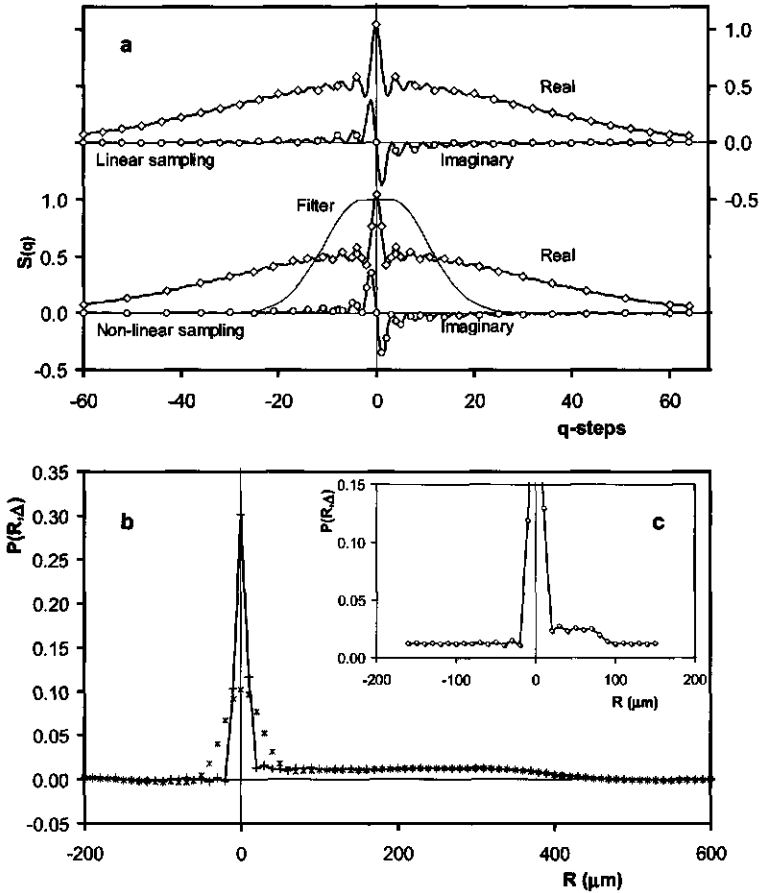


Figure 7.3: Simulated data of 50% stationary and 50% flowing water (with maximum linear velocity 20.0 mm/s) before (a) and after (b+c) Fourier Transformation. In (a) the simulated signal is indicated with solid lines, diamonds and circles represent the experimental sampling. $S(q)$ can be sampled linearly with equidistant steps (upper chart in (a)) or non-linearly with an emphasis on small q -values (lower chart in (a)). The solid line in (b) interconnects the data points of the propagator after interpolation and FT of the non-linearly sampled signal. In (c) the aliased propagator after FT of the linearly sampled signal is shown (cf. Fig. 7.2d). Applying a filter to the data before FT results in severe broadening of the stationary water peak, but hardly affects the flowing part of the propagator (asterisks in (b)).

of the averaged propagators of all the pixels of the indicated vascular bundle are shown in Fig. 7.4b: the propagator after FT of the signal of linearly sampled q -space (represented by diamonds) is interconnected by a dashed line, and the propagator after FT of the interpolated and filtered signal of non-linearly sampled q -

space (represented by plusses) is shown with a solid line. Using linear q -steps, an equal amount of time is spent on small and large q -values, whereas with non-linear steps, the smaller q -values, where signal intensities are higher, take up a larger part of the total experimental time. The SNR of the flowing part of the non-linear

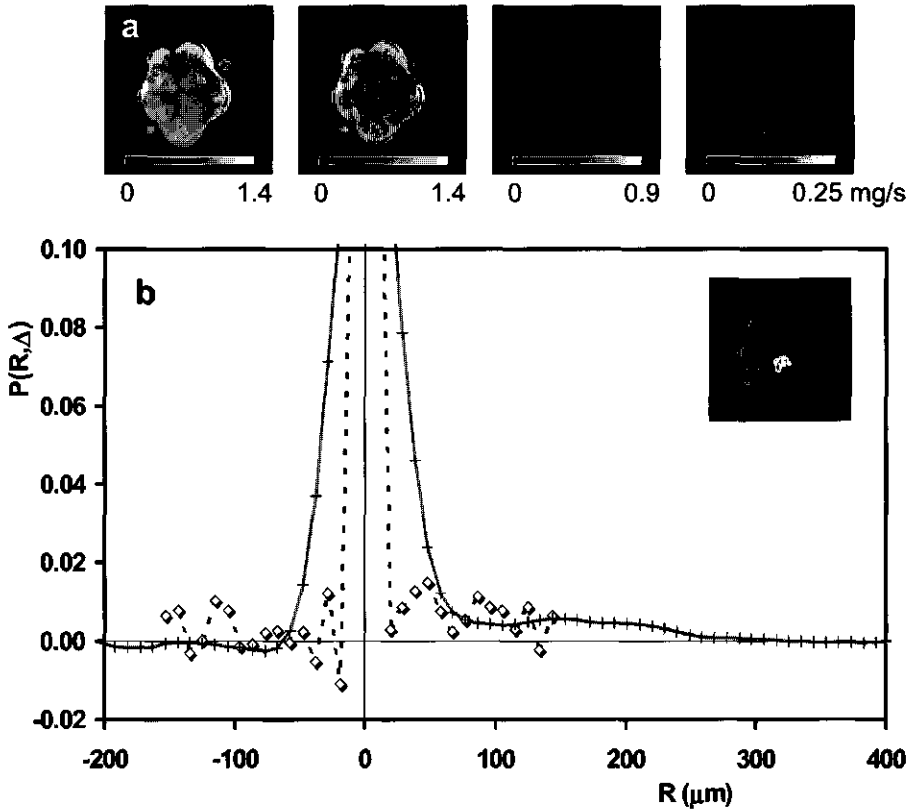


Figure 7.4: Experimental data from a cucumber plant stem. The images in (a) represent the flow characteristics of an experiment with non-linear q -space sampling. These are respectively the total amount of water, the amount of stationary water, the amount of flowing water, all three relative to the averaged amount of water of a pixel in the reference tube (normalized to 1), and the volume flow in mg/s. The propagator in (b) is a summation of the propagators of all pixels in one vascular bundle, indicated in the inset. The experimental data, represented by diamonds (interconnected by the dashed line) are the result of linear q -space sampling before FT. The plusses (interconnected by a solid line) indicate the propagator of non-linearly sampled q -space using interpolation and filtering before FT. Experimental parameters: 50 kHz bandwidth, 32 echoes in TSE train, 128 x 128 matrix, field of view 15.4 mm, slice thickness 3.0 mm, repetition time 2.5 s, Δ 9.13 ms, δ 3.0 ms, g_{max} 0.409 T/m, total measurement time 24 minutes for 36 non-equidistant steps and 21 minutes for 32 equidistant steps.

experiment is therefore higher, especially after applying the filter. Since rapid, abrupt jumps or changes in the flowing part of a propagator are not to be expected, the smoother shape of the propagator from non-linear sampling and filtering is preferred above the noisy, truncated shape of the propagator using linear steps as in Fig. 7.4b. The total volume flow values from all pixels with flowing water in non-linearly sampled experiments correspond to water uptake values of the cucumber plant, measured with a precision balance (Chapter 6). The total volume flow values, calculated from linearly sampled experiments, systematically deviated from the water uptake values, measured using the precision balance (Chapter 6).

Resolution, relaxation and quantification

The SNR of a pixel in an NMR image depends on the amount of water in that pixel, which is the product of tissue water content and pixel volume: the larger a pixel, the lower the spatial resolution of the image, and the higher the SNR of the pixel. In plant stems the thickness of the imaged slice, representing a cross-section of the stem, can be set to a much larger value than the in-plane resolution of the image, because of a large tissue symmetry along the plant stem direction. Signal averaging over a number of scans also increases the SNR, but immediately lengthens the total measurement time ($\text{SNR} \sim \sqrt{\text{number_of_averaging_scans}}$). Since both a high spatial resolution and a high SNR per pixel are desirable, preferably within an acceptable measurement time, every experiment is a compromise between spatial resolution, SNR and measurement time. The main consideration in this compromise should be the question what information needs to be extracted from the experiment. This information needs to be acquired as accurate as possible within the available measurement time, which is the reason why a high spatial resolution is not always needed. In quantitative T_2 and proton density imaging and dynamic NMR imaging information can be retrieved from several parameters for every pixel, providing a kind of sub-pixel resolution.

Quantitative T_2 and proton density imaging can even be severely hampered by a high spatial resolution. Movement of protons by self-diffusion in the time between

the large read-out imaging gradients, needed for a high resolution, can attenuate the NMR signal (9). Then, the NMR signal decays not only because of spin-spin relaxation, but also because of diffusion. Generally, an exponential decay curve is fitted to the NMR signal decay of every pixel to acquire the T_2 and the initial signal amplitude at the moment of excitation, reflecting the proton density (or water density). The additional signal attenuation because of diffusion decreases the signal decay time, whereas the initial signal amplitude will remain largely unaffected. Figure 7.5 shows the difference in T_2 contrast between two experiments of a geranium petiole with different spatial resolution. At a resolution of $39 \times 39 \times 2500 \mu\text{m}$ T_2 -values of large parenchyma cells in the central cylinder clearly differ from T_2 -values in the cortex, and also the vascular bundles are visible. At a higher resolution of $31 \times 31 \times 2500 \mu\text{m}$ all T_2 -values have decreased, and almost all contrast is gone. The water density images are hardly effected by the additional signal attenuation.

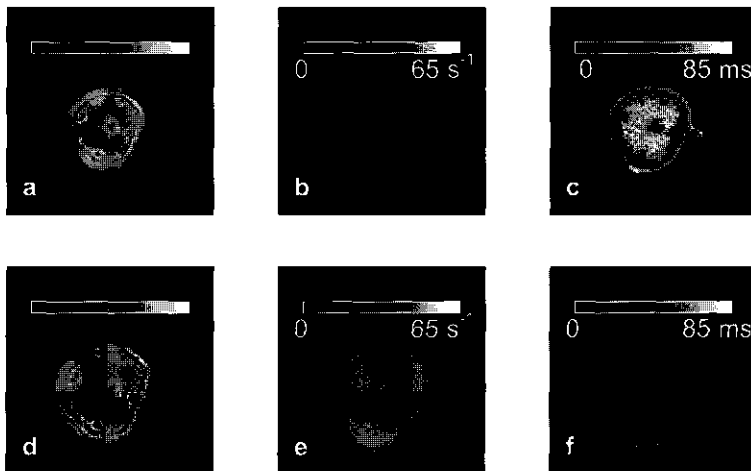


Figure 7.5: Single parameter images of a geranium petiole. The images are calculated from two multi-echo imaging experiments (9) with different resolutions. Images (a) to (c) are the calculated water density image, a $1/T_2$ and a T_2 image with a field of view of 5 mm (nominal resolution $39 \times 39 \times 2500 \mu\text{m}$). Images (d) to (f) are images of the same parameters with a field of view of 4 mm (nominal resolution $31 \times 31 \times 2500 \mu\text{m}$). Although the T_2 -values are probably already affected by diffusion for both field of views, the decrease of T_2 -values for higher resolution clearly illustrates the effect of increasingly larger gradients in combination with diffusion. Experimental parameters: 25 kHz bandwidth, echo time 6.6 ms, 64 echoes, 128×128 matrix, 6 averages, repetition time 2.5 s, total measurement time 32 minutes.

At lower resolution (in the order of $0.5 \times 0.5 \times 3$ mm), the SNR of one pixel can be sufficiently high for a meaningful multi-exponential fit (i.e. with acceptable standard deviations of the fitted parameters). This results in two or more water fractions and corresponding relaxation times, which can be assigned to the water within one pixel, creating sub-pixel resolution. In the stem of an intact cucumber plant a relatively high spatial resolution has been used to distinguish different tissues on the basis of water density and T_2 of a mono-exponential fit, after which the signal decay curves of a single tissue type were averaged to increase the SNR (4). The averaged decay curves were fitted to a two-exponential function of which the two water fractions were ascribed to vacuolar water on one hand and water in the cytoplasm and extracellular water on the other hand. Transient changes in T_2 -values of the fractions in the tissues may give information about exchange of water over the membranes separating the fractions (the vacuolar and plasmalemma membrane) (Van der Weerd *et al.*, Journal of Experimental Botany, accepted).

Not only in quantitative T_2 imaging, but also in a dynamic NMR imaging experiment, high resolution is not always necessary. The acquisition of propagators enables discrimination between stationary and flowing water at pixel level (20). Even if one or more xylem vessels are captured within one pixel, the signal of the flowing water can still be separated from stationary water. Then, another compromise has to be made between spatial resolution and the number of q-steps encoding for flow. The choice depends on the question: what information is more important: an exact localization of flow or an accurate flow profile? Xylem vessels in cucumber plant stems can have diameters up to $350 \mu\text{m}$ (22), which can be localized much easier (cf. Fig. 7.4a) than xylem vessels in e.g. a Chrysanthemum stem with diameters up to $50 \mu\text{m}$ (23). For large vessels the amount of flowing water in a pixel is often also large, corresponding to a large integral of the flowing fraction in a pixel-propagator. In this case quantification of the propagators is accurate (the total volume flow of all pixels with flow corresponds to the water uptake of the plant, measured with a balance (4)). With smaller vessels, the amount of flowing water within a pixel is small, which is one of the problems with flow quantification, discussed in the next section.

Flow quantification problems

In Chrysanthemum stem segments, the total volume flow of all pixels with flowing water does not always correspond with uptake values measured with a balance. This is illustrated using the results of an air-inlet experiment of a Chrysanthemum flower (cv. Cassa) in Fig. 7.6. A 22-cm stem segment was cut out of a Chrysanthemum flower under water to avoid air entrance in the xylem vessels. The segment was placed in the NMR setup and the top of the segment was connected with silicone tubing to a setup controlling water uptake, (20, 24). After some time of stable water uptake due to the applied underpressure at the top of the stem segment, the water level was lowered below the bottom of the segment for 10 minutes, admitting air to the xylem vessels. After reapplying water to the cut surface of the stem segment, the restoration of water uptake of the segment was monitored

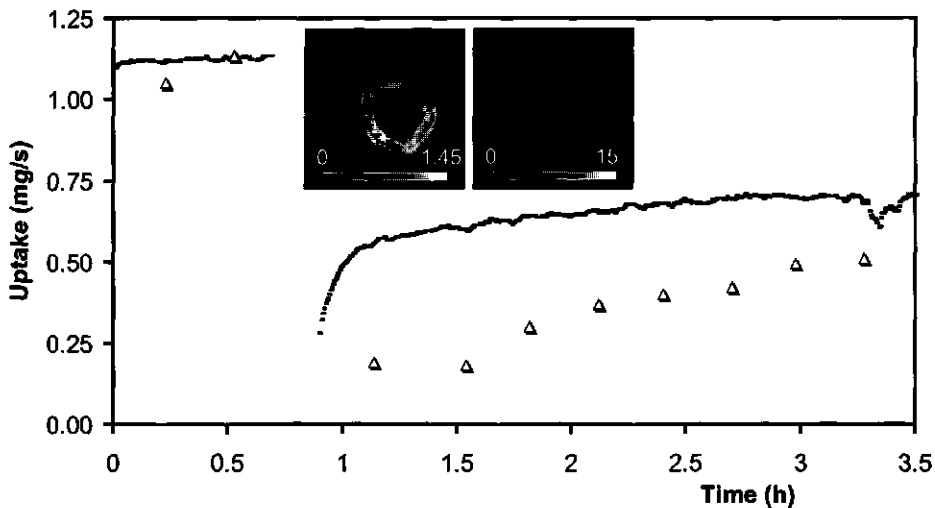


Figure 7.6: Water flow rate pattern before and after air inlet of a stem segment of a Chrysanthemum flower, cut off under water. The interrupted curve represents water uptake, measured using a precision balance; the triangles represent the total volume flow calculated from NMR measurements. Inset: two images from a transverse slice through the stem segment representing the total amount of water, relative to the amount of water in a pixel in the reference tube ($=1$, average of nine pixels), and the volume flow per pixel. Experimental parameters: 50 kHz bandwidth, 32 echoes in TSE train, echo time in train 4.26 ms, 128 x 128 matrix, field of view 12.8 mm, slice thickness 2.5 mm, repetition time 1.0 s, 32 PFG steps, Δ 15.6 ms, δ 2.5 ms, g_{max} 0.375 T/m, total measurement time 17 minutes, pressure difference over the stem segment was maintained at 38.8 kPa.

in time. The water uptake measurements, measured with the balance (dots in Fig. 7.6), clearly show an initial water uptake of 1.12 mg/s. After air inlet, an initial quick recovery is followed by a slower restoration to a plateau value of about 0.70 mg/s, but the initial uptake values before air inlet are not reached anymore. The mechanism behind the removal of air from the stem segment and the time course of restoration of the original flow profiles have been studied in detail elsewhere (25). Primary concern here is the development of the total volume flow values, calculated from the NMR measurements. These values do not coincide with the uptake values, measured with the balance, for which possible reasons are discussed in the next section. In the inset in Fig. 7.6 an image of the total amount of water and an image with the volume flow are shown (the large void in the center of the stem in the image consists of dry spongy matter that does not contain water). The visible ring contains the epidermis, supporting fibers, phloem tissue, xylem tissue and parenchymal cells. Flow is visible in small groups of pixels in the xylem tissue, in the larger xylem vessels of the primary and early secondary xylem.

How do we calculate the total volume flow through the stem segment? As is described in the introduction of the quantification method (20), the intensity of every point of a propagator $P(R, \Delta)$ (cf. Fig. 7.3 and 7.4) can be related to an amount of water by using the signal intensity I_{ref} of a reference tube filled with water for calibration. After subtraction of stationary water from a propagator, the volume flow Q through a pixel is a summation of the propagator intensities of flowing water, multiplied by their corresponding displacement values R within the labeling time (20):

$$Q = \sum_{R=0}^{R=R_{max}} (P(R, \Delta)R) \frac{I_{ref}}{\Delta} \quad [3].$$

For accurate volume flow values, the SNR needs to be as high as possible: this is the reason why not every displacement value is incorporated in the addition of intensities, but only those from zero to the maximum displacement R_{max} of the water in that pixel. R_{max} , the point at which the signal has vanished and only noise is left, is chosen at the displacement value just before the first point in the flowing part of a propagator with negative intensity. To calculate the total volume flow through the stem segment we performed another operation to decrease noise. The total volume

flow is a summation of only those pixels with a volume flow above a threshold value ($\sim 2/3$ of peak noise level), which have at least one neighboring pixel with intensity also above this threshold value. The reason for this selection criterion is the fact that the numerous xylem vessels in the stem segment are small compared to the in-plane pixel resolution of $100 \times 100 \times 2500 \mu\text{m}$, but all the vessels are localized in the *primary and secondary xylem of the stem, which covers multiple adjoining pixels*. The disadvantage of this criterion is that the volume flow of individual pixels (if any) without neighboring pixels with intensity above the threshold are discarded as noise.

Before air inlet, all flow has been localized: uptake values from NMR measurements coincide with the uptake measured with the balance. After air inlet however, only 32% of the actual uptake is measured by NMR (considering the same pixels as before air inlet), and this percentage increases in time up to 73% by the final measurement. The surprisingly low and increasing percentage of flow that can be localized by the NMR measurements can have different reasons. Firstly it is the SNR of the volume flow image. Many xylem vessels (especially with relatively large diameters, in the order of $40 \mu\text{m}$ (26)) which originally transported water are blocked just after air inlet (27). Vessels that remain active probably have small diameters (in the order of $10 \mu\text{m}$ (26)), resulting in a small amount of flowing water per pixel, and therefore a low intensity in the flowing part of the propagator. Signal intensity of the flowing part can become negative because of the small SNR: R_{max} is estimated systematically too low and Q of the pixel decreases more than it should (cf. the linear sampling of the cucumber vascular bundle in Fig. 7.4b, in which the flowing part of the propagator exceeds far beyond the first negative propagator intensity at $R = 130 \mu\text{m}$). In time, the air in some vessels dissolves and the vessel functions again, increasing the amount of flowing water in a pixel, elevating the flowing part of the corresponding pixel-propagator, which now adds to the total volume flow together with small, continuously active vessels, previously unaccounted for. Changing the way R_{max} is determined, by choosing R_{max} just before the second point of the flowing part of the propagator with negative intensity, introduces more noise in the volume flow values per pixel, causing scatter in the time-course of the total volume flow values.

The second reason for a change in the percentage of recovered volume flow can be found in the use of the reference tube for calibration. In the presented TSE experiments the signal intensity of the first echo determines the total integral of the TSE image (18). In the time t from excitation to the first echo the NMR signal $S(t)$ decays according to the spin-spin relaxation time T_2 :

$$S(t) = A_0 e^{(-t/T_2)} \quad [4],$$

in which A_0 is the initial signal amplitude. If the spin-spin relaxation time of the water in the reference tube differs largely from the T_2 of the water in the xylem vessel (relative to the time from excitation to the first echo), the signal intensity in the TSE image of the water in the reference tube is attenuated with a different factor than the intensity of the water in the vessel. If the first echo time is at 17.5 ms after excitation and the relaxation times of the reference tube and the xylem sap are approximately 150 and 400 ms respectively (as is the case in the cucumber plant stem), the difference in signal intensity in the corresponding integral of the propagators is 7.5%. However, if T_2 -values of the xylem sap are in the order of 50 ms and the first echo is at 23.2 ms after excitation, the difference in the integral of the propagators is 36%. If the exchange of water into and out of the xylem vessels in the stem segment changes, because of changes in permeability for water when restoring original flow-profiles, the T_2 -values of the xylem vessels could change in time. This would change the signal attenuation factor and thereby the calculated volume flow.

A decrease of the T_2 of water in the vessels in time can also introduce a blurring effect on the TSE images (18). This effect will spread the propagator intensity of a pixel in the phase encode direction lowering the SNR of the flowing part of the propagator of that pixel, of which the consequences were described in the previous section. In this complicated matter, it might be worth giving up time resolution by not using the TSE sequence, but evaluate the signal decay for every q-step with a multiple spin echo train. In that case a signal decay curve is available for every point of the propagator, so different relaxation times can be ascribed to flowing and stationary water within one pixel. A propagator of the initial signal amplitudes can then be constructed for accurate quantification as described in the addendum of Chapter 3.

Conclusions

NMR imaging studies of large plants do not necessarily have to be performed at high magnetic field strength. The accessibility of the iso-center of the magnetic field and the possibility to position the plant vertically are two advantages of using an electromagnet or a wide-bore vertical superconducting magnet. Electromagnets usually have lower magnetic field strengths and therefore a low SNR. The use of dedicated solenoid rf coils overcome part of the low SNR problem. The possibility of acquiring many signal-containing echoes of plant tissue at low magnetic field strength also increases the SNR and creates great opportunities for plant studies. This long echo train can be used either for quantitative water density and T_2 measurements, or to shorten the measurement time with a TSE train, enabling a faster acquisition of any magnetization-prepared image.

The flow profile of water, flowing in a pixel of an image of a plant stem, depends on the size of the xylem vessels relative to the size of one pixel and the observation time that is used to monitor flow in a PFG experiment. Therefore it is necessary to record the complete distribution of displacements within the observation time. The dynamic range problem of probing high linear velocities in a propagator can be circumvented by stepping the PFGs in a non-equidistant way. Sampling small q -values in more detail and interpolating larger q -values increases the SNR of the flowing part of the corresponding propagator and enlarges the displacement axis.

A high spatial resolution is not always necessary but always a trade-off with time resolution, accuracy and detail in the displacement distribution. In quantitative T_2 imaging a high resolution can even severely distort the T_2 -contrast, because of additional signal attenuation due to self-diffusion in large read-out gradients. One can obtain a kind of sub-pixel resolution by fitting or calculating more than one parameter for every pixel of an image. In a multi echo experiment one can distinguish different water fractions within one pixel or within the same type of tissue (by fitting multi-exponential decay curves), and in a dynamic NMR experiment (PFG TSE imaging) one can discriminate stationary from flowing water.

If the amount of flowing water within a pixel becomes too small, problems with extracting the flow characteristics can occur. Some of the possible reasons can be a low SNR or differences in T_2 between the flowing water and the water used for calibration (in a reference tube). With complicated quantification problems an experiment probing both the propagator and the signal decay curve for every pixel can be considered.

Acknowledgement

This research was supported by the Dutch Technology Foundation STW, applied science division of NWO (project WBI 3493).

References

1. H. H. Dixon and J. Joly, *Philos. Trans. R. Soc. Lond. Ser. B-Biol. Sci.* **186**, 563-576 (1894).
2. N. Ishida, M. Koizumi and H. Kano, *Ann. Bot.* **86**, 259-278 (2000).
3. W. Köckenberger, *J. Exp. Bot.* **52**, 641-652 (2001).
4. T. W. J. Scheenen, A. M. Heemskerk, P. A. de Jager, F. J. Vergeldt and H. Van As, *Biophys. J.* submitted (2001).
5. D. I. Hoult and R. E. Richards, *J. Magn. Reson.* **24**, 71-85 (1976).
6. K. M. Lüdecke, P. Röschmann and R. Tischler, *Magn Reson Imag.* **3**, 329-343 (1985).
7. S. Posse and W. P. Aue, *J. Magn. Reson.* **88**, 473-492 (1990).
8. H. C. W. Donker, H. Van As, H. T. Edzes and A. W. H. Jans, *Magn. Reson. Imag.* **14**, 1205-1215 (1996).
9. H. T. Edzes, D. van Dusschoten and H. Van As, *Magn. Reson. Imag.* **16**, 185-196 (1998).
10. R. D. Black, T. A. Early, P. B. Roemer, O. M. Mueller, A. Mogro Campero, L. G. Turner and G. A. Johnson, *Science*, **259**, 793-795 (1993).
11. P. T. Callaghan, C. D. Eccles and Y. Xia, *J. Phys. E: Sci. Instrum.* **21**, 820-822 (1988).
12. P. T. Callaghan, S. L. Codd and J. D. Seymour, *Concepts Magn. Reson.* **11**, 181-202 (1999).
13. U. Tallarek, E. Rapp, T. Scheenen, E. Bayer and H. Van As, *Anal. Chem.* **72**, 2292-2301 (2000).
14. J. Kärgler and W. Heink, *J. Magn. Reson.* **51**, 1-7 (1983).
15. W. Köckenberger, J. M. Pope, Y. Xia, K. R. Jeffrey, E. Komor and P. T. Callaghan, *Planta* **201**, 53-63 (1997).
16. P. T. Callaghan, W. Köckenberger and J. M. Pope, *J. Magn. Reson. Series B* **104**, 183-188 (1994).

17. J. Hennig, A. Nauerth and H. Friedburg, *Magn. Reson. Med.* **3**, 823-833 (1986).
18. T. W. J. Scheenen, D. van Dusschoten, P. A. de Jager and H. Van As, *J. Magn. Reson.* **142**, 207-215 (2000).
19. T. W. J. Scheenen, F. J. Vergeldt, C. W. Windt, P. A. de Jager and H. Van As, *J. Magn. Reson.* **151**, 94-100 (2001).
20. T. W. J. Scheenen, D. van Dusschoten, P. A. de Jager and H. Van As, *J. Exp. Bot.* **51**, 1751-1759 (2000).
21. X.A. Mao and O. Kohlmann, *J. Magn. Reson.* **150**, 35-38 (2001).
22. J. E. A. Reinders, *Thesis Molecular Physics* (Wageningen University, Wageningen) (1987).
23. J. Nijse, G. W. A. M. van der Heijden, W. van Ieperen, C. J. Keijzer and U. van Meeteren, *J. Exp. Bot.* **52**, 319-327 (2001).
24. W. van Ieperen, U. van Meeteren and H. van Gelder, *J. Exp. Bot.* **51**, 769-776 (2000).
25. W. van Ieperen, U. van Meeteren and J. Nijse, *Post Harvest Biol. Biotechn.* , submitted (2001).
26. J. Nijse, *Thesis Horticultural Production Chains* (Wageningen University, Wageningen) (2001).
27. W. van Ieperen, J. Nijse, C. J. Keijzer and U. van Meeteren, *J. Exp. Bot.*, in press (2001).

Summary

This Thesis treats one of the new techniques in plant science i.e. nuclear magnetic resonance imaging (NMRI) applied to water motion in plants. It is a challenge to measure this motion in intact plants quantitatively, because plants impose specific problems when studied using NMRI. At high magnetic field strength air-filled intercellular spaces in the plant tissue cause susceptibility-related local magnetic field inhomogeneities, which are much smaller at low magnetic field strength. The inherently low signal-to-noise ratio at low magnetic fields is compensated by the possibility to record a long train of spin-echoes, since generally the spin-spin relaxation time T_2 at low magnetic field is longer than at high magnetic field.

In this Thesis the spin echo train is used to shorten the time to produce an NMR image. As a result, time-dependent flow phenomena can be followed at a physiologically relevant time scale using dynamic NMRI employing either a pulsed field gradient (PFG) spin echo sequence (for fast flow, Chapter 2) or a PFG stimulated echo motion-encoding sequence (for slow flow, Chapter 3). Using the quantification method presented in this Thesis (Chapter 4) a number of flow characteristics can be determined for every pixel in an image of a plant stem:

- the total amount of water,
- the amount of stationary water,
- the amount of flowing water,
- the mean linear flow velocity of the flowing water and
- the volumetric flow rate.

These flow characteristics, together with the water density (or total amount of water) and the T_2 value per pixel (measured with quantitative T_2 imaging), were studied in the stem of a cucumber plant as a function of the day-night cycle and cooling of the root system. Root cooling results in inhibition of the water uptake and xylem- and phloem transport, and causes severe wilting of the plant leaves. Following root cooling, during recovery of the plant from its wilted state, the T_2 -values of tissue around the vascular bundles strongly decrease, which may indicate an increased membrane permeability for water of the tissue cells in this period (Chapter 5).

During root cooling, large negative pressures in the plant xylem cause cavitations in the vessels, blocking further water transport. In this Thesis the first direct *in vivo*

observations of refilling of cavitated xylem vessels are presented (Chapter 6). This refilling takes many hours and occurs while nearby vessels are under tension and are transporting water. This finding has important implications for the mechanism underlying the refilling process: water entering the refilling vessel must be hydraulically isolated from flowing water in nearby vessels.

The strategy (Chapter 7) and methodology of quantitative flow and T_2 NMR imaging, discussed in this Thesis have opened new ways to find answers to longstanding questions in plant science.

Samenvatting

Dit proefschrift behandelt een voor plantenwetenschappen nieuwe techniek, te weten NMR imaging (ruimtelijk opgeloste kernspinresonantie) toegepast op beweging van water in planten. Het is een uitdaging deze bewegingen in levende planten te meten omdat planten specifieke problemen met zich meebrengen wanneer deze kwantitatief met NMR imaging bestudeerd worden. In sterke magnetische velden veroorzaken met lucht gevulde intercellulaire holtes in plantaardig weefsel lokale magneetveld inhomogeniteiten, die veroorzaakt worden door verschillen in susceptibiliteit, en die bij lage magneetveldsterktes veel zwakker zijn. De aan lage veldsterkte inherente lage NMR signaal/ruis verhouding wordt gecompenseerd door de mogelijkheid tot het opnemen van een lange spin echo trein, omdat in het algemeen de spin-spin relaxatie tijd T_2 bij lage magneetveldsterkte langer is dan bij hogere magneetveldsterkte.

In dit proefschrift wordt de spin echo trein gebruikt om de opnametijd van één image te verkorten. Hierdoor kunnen tijdsafhankelijke stromings-processen op een fysiologisch relevante tijdschaal bestudeerd worden met een gepulste veld gradiënt spin echo sequentie (voor snelle stroming, Hoofdstuk 2) of een gepulste veld gradiënt gestimuleerde echo sequentie (voor langzame stroming, Hoofdstuk 3). Met de kwantificeringsmethode, gepresenteerd in dit proefschrift (Hoofdstuk 4), kunnen de volgende stromingskarakteristieken worden bepaald voor elk pixel in een NMR image van de stengel van een plant:

- de totale hoeveelheid water,
- de hoeveelheid stilstaand water,
- de hoeveelheid stromend water,
- de gemiddelde lineaire stroomsnelheid van het stromend water en
- de volumetrische stroomsnelheid.

Het verloop van deze stromingskarakteristieken samen met de totale hoeveelheid water en de T_2 per pixel (gemeten met kwantitatieve T_2 metingen) is bestudeerd in de stengel van een komkommerplant als functie van het dag-nacht ritme en het koelen van de wortels van de plant. Wortelkoeling remde de wateropname, het xyleem- en het floëem transport en liet de bladeren van de plant sterk verwelken. Na wortelkoeling, in de tijd waarin de verwelkte bladeren van de plant zich weer herstellen, zijn de T_2 waarden van het weefsel rondom vaatbundels veel lager dan

ervoor, wat zou kunnen duiden op een verhoogde permeabiliteit voor water van de membranen van de cellen in het betreffende weefsel gedurende deze periode (Hoofdstuk 5).

Grote onderdrukken in het xyleem van de plant tijdens wortelkoeling veroorzaakte cavities in de vaten, waardoor water transport geblokkeerd werd. In dit proefschrift worden de eerste, directe *in vivo* waarnemingen van het opvullen van gecaviteerde xyleemvaten beschreven (Hoofdstuk 6). Dit vullen van gecaviteerde vaten neemt vele uren tijd in beslag en gebeurt terwijl bijna aangrenzende xyleemvaten nog gewoon water transporter en dus een onderdruk ervaren. Dit gegeven heeft belangrijke consequenties voor het mechanisme van het opvullen van gecaviteerde vaten: water dat het gecaviteerde vat binnenkomt mag niet in hydraulisch contact staan met water in de omringende vaten.

De onderzoeksstrategie (Hoofdstuk 7) en het gebruik van de kwantitatieve stromings- en T_2 metingen in dit proefschrift hebben nieuwe mogelijkheden gecreëerd om antwoorden te vinden op al lang bestaande vragen in de plantenwetenschappen.

List of Publications

U. Tallarek, E. Bayer, D. van Dusschoten, T.W.J. Scheenen, H. Van As, G. Guiochon and U.D. Neue, Dynamic NMR microscopy of chromatographic columns, *American Institute of Chemical Engineers Journal*, Vol. 44, pp. 1962-1975 (1998).

D. van Dusschoten, U. Tallarek, T.W.J. Scheenen, U.D. Neue and H. Van As, Spatially resolved transport properties in radially compressed bead packings studied by PFG NMR, *Magnetic Resonance Imaging*, Vol. 16, pp. 703-706 (1998).

T.W.J. Scheenen, D. van Dusschoten, P.A. de Jager and H. Van As, Fast spatially resolved displacement imaging in (bio)systems, in 'Spatially Resolved Magnetic Resonance, Methods, Materials, Medicine, Biology, Rheology, Geology, Ecology, Hardware', (P. Blümler, B. Blümich, R. Botto and E. Fukushima, eds.), pp. 481-486, Wiley-VCH, Weinheim, New York (1998).

T.W.J. Scheenen, D. van Dusschoten, P.A. de Jager and H. Van As, Microscopic displacement imaging with pulsed field gradient turbo spin echo NMR, *Journal of Magnetic Resonance*, Vol. 142, pp. 207-215 (2000).

T.W.J. Scheenen, D. van Dusschoten, P.A. de Jager and H. Van As, A model-free quantification of water transport in intact plants with NMR imaging, *Journal of Experimental Botany*, Vol. 51, pp. 1751-1759 (2000).

U. Tallarek, E. Rapp, T. Scheenen, E. Bayer and H. Van As, Electroosmotic and pressure-driven flow in open and packed capillaries: velocity distributions and fluid dispersion, *Analytical Chemistry*, Vol. 72, pp. 2292-2301 (2000).

U. van Meeteren, W. van Ieperen, J. Nijse, T.W.J. Scheenen, H. Van As and C.J. Keijzer, Processes and xylem anatomical properties involved in rehydration dynamics of cut flowers, *Acta Horticulturae*, Vol. 543, pp. 207-215 (2001).

T.W.J. Scheenen, F.J. Vergeldt, P.A. de Jager and H. Van As, Microscopic imaging of slow flow and diffusion: a pulsed field gradient stimulated echo sequence combined with turbo spin echo imaging, *Journal of Magnetic Resonance*, Vol. 151, pp. 94-100 (2001).

U. Tallarek, T.W.J. Scheenen, P.A. de Jager and H. Van As, Using NMR displacement imaging to characterize electro-osmotic flow in porous media, *Magnetic Resonance Imaging*, Vol. 19, pp. 453-456 (2001).

A.K. Heibel, T.W.J. Scheenen, J.J. Heiszwolf, H. Van As, F. Kapteijn and J.A. Moulijn, Gas and liquid phase distribution and their effect on reactor performance in the monolith film flow reactor, *Chemical Engineering Science*, in press.

U. Tallarek, T.W.J. Scheenen, and H. Van As, Macroscopic flow heterogeneity in electroosmotic and pressure-driven flows through fixed beds at low column-to-particle diameter ratio, *Journal of Physical Chemistry B*, in press.

T.W.J. Scheenen, A.M. Heemskerk, P.A. de Jager, F.J. Vergeldt and H. Van As, Functional imaging of plants: a nuclear magnetic resonance study of a cucumber plant, *the Biophysical Journal*, submitted.

T.W.J. Scheenen, A.M. Heemskerk, P.A. de Jager, F.J. Vergeldt and H. Van As, Embolism induction and repair in xylem vessels of *Cucumis Sativus* L., in preparation.

T.W.J. Scheenen, P.A. de Jager, F.J. Vergeldt and H. Van As, Measuring plant water status and transport with nuclear magnetic resonance imaging: a strategy, in preparation.

Curriculum vitae

Thomas Wilhelmus Jacobus Scheenen werd geboren op 10 augustus 1974 in Roggel. Zijn Atheneum-B diploma met twee extra vakken behaalde hij aan de Scholen-gemeenschap Sint Ursula te Horn in 1992, waarna hij met de studie Moleculaire Wetenschappen aan de Wageningen Universiteit begon. Deze studie werd cum laude afgerond in 1996 met afstudeervakken bij de vakgroepen Moleculaire Fysica en Experimentele Diermorphologie en Celbiologie. In 1997 begon hij als Onderzoeker in Opleiding bij het laboratorium voor Biofysica (voorheen Moleculaire Fysica), gefinancierd door de Stichting Technische Wetenschappen, en verrichtte hij onderzoek dat leidde tot dit proefschrift. Per 1 september 2001 is hij werkzaam als Fysicus MRI bij het Universitair Medisch Centrum Sint Radboud te Nijmegen.